SILICON WAVEGUIDE INTEGRATED NANOPLASMONICS FOR OPTOELECTRONIC AND SENSING APPLICATIONS

A DISSERTATION

SUBMITTED TO THE FACULTY OF

UNIVERSITY OF MINNESOTA

BY

CHE CHEN

IN PARTIAL FULFILLMENT OF THE REQUIREMENTS

FOR THE DEGREE OF

DOCTOR OF PHILOSOPHY

MO LI

AUGUST 2018

Acknowledgments

First of all, I would like to thank my advisor, Prof. Mo Li for advising me during my pursuit for PhD degree. When I first joined his research group, I wasn't very familiar with the research projects in the lab and the progress was slow in the beginning. Prof. Li is very patient to me and gives me time to acquire necessary knowledge and skills. Also, his rigorous attitude and high requirement towards high-quality research work impresses and influences me greatly. Without his guidance and inspiration, the work presented in this dissertation would not exist.

In addition to my advisor, I also thank Prof. Sang-Hyun Oh for his dedicated help in my research. We had numerous discussions together and generated several innovative ideas, which leads to my research projects. Also, Prof. Oh generously spent much time in improving these ideas and provide crucial assistance in my research. His experience and expertise are of great importance for our research.

I also thank Prof. Steven Koester for his instruction in semiconductor physics and help in my research. I didn't have much understanding on this topic when I started PhD study. I am very grateful to have the opportunity to learn this topic from a renowned expert like Prof. Koester.

I thank collaborators who offer their selfless sharing and help. Dr. Daehan Yoo, Daniel Mohr and Dr. Han-Kyu Choi provided crucial assistance in plasmonic research that I am not very familiar. Dr. Nathan Youngblood and Dr. Huan Li help me a lot in my experiment and theory with their valuable experience. Especially I would like to thank Dr. Youngblood for his help when I started my research.

My appreciation also goes to other members that I have worked with in the lab. I thank Dr. Junyang Chen, Dr. Li He, Dr. Semere Tadnesse, Dr. Yu Chen, Qiyu Liu, Ruoming Peng, Jiacheng Yuan, Bingzhao Li and Changming Wu for their assistance in my research and many other matters.

I also appreciate the help from staff members from Minnesota Nanofabrication Center and Characterization Facility for their careful maintenance of the scientific tools. I would like to especially mention the assistance and advice from Dr. Bryan Cord, Kevin Roberts, Tony Whipple, Lage von Dissen, Dr. Nicholas Seaton and Dr. Bing Luo.

My special thanks are for my parents who encouraged me to pursue my dreams when I was young and help me out when I am in need. Without their longtime support in my study, I would not go this far to pursue this PhD degree.

Abstract

Silicon photonics, utilizing silicon and other semiconductors for on-chip light manipulation, has scaled the conventional optoelectronic devices (e.g. waveguide, photodetector and modulators) down to sub-micrometer footprint. This enables rack-to-rack high-bandwidth optical communication in data centers. Moreover, silicon photonics provides an on-chip platform for fundamental research including optomechanics, cavity electrodynamics and chemical sensing.

On the other hand, surface plasmon polariton (SPP), can confine light into hotspot below optical diffraction limit and significantly enhance local electromagnetic field. This boosts the light-matter interaction significantly and enable biosensing applications including SERS and SEIRA. However, the metallic structure introduces high optical absorption, which is detrimental for long distance light propagation. In this dissertation, we focus on the on-chip integration of silicon photonics and plasmonics: using the dielectric waveguide for light delivery and plasmonics for light focusing. This integration approach combines the advantages of the low propagation loss of silicon waveguides, high-field confinement of a plasmonic structure for enhanced light-matter interaction.

In the first project, we show the integration of a black phosphorus photodetector in a three-dimensional architecture of silicon photonics and metallic nanoplasmonics structures. By vertically integrating plasmonic grating on top of a silicon waveguide grating, a nanoscale optic hotspot is created. Adding another layer of 2D material, black phosphorus, an efficient telecom-band photodetector is fabricated. The short-channel (~60 nm) BP FET shows an on-off ratio up to 1000. Moreover, benefiting from the ultrashort

channel and near-field enhancement enabled by the nanogap structure, the photodetector shows an intrinsic responsivity as high as 10 A/W afforded by internal gain mechanisms, and a 3-dB roll-off frequency of 150 MHz.

Such a hybrid integration also obviates the need for a bulky free-space optics setup and can lead to fully integrated, on-chip optical sensing systems. In the second project, we directly pattern an ultra-compact plasmonic resonator atop a mid-infrared silicon waveguide for spectroscopic chemical sensing. The footprint of the plasmonic nanorod resonators is as small as 2 μm^2, yet they can couple with the mid-infrared waveguide mode efficiently. The plasmonic resonance is verified by measuring the transmission spectrum of the waveguide, with a coupling efficiency greater than 70% and a field intensity enhancement factor of over 3600 relative to the evanescent waveguide field intensity. Using this hybrid device and a tunable mid-infrared laser source, surface-enhanced infrared absorption spectroscopy of both a thin PMMA film and an octadecanethiol monolayer are successfully demonstrated.

Table of Contents

List of Tables

List of Figures

Chapter 1. Introduction

1.1. Silicon Photonics and Two-dimensional Materials

1.1.1. Silicon Photonics as a Novel Optic Platform

Since the beginning of the ray optics, the conventional free-space optical setup consists of dielectric lenses, metallic mirrors, polarization control components and precise alignment stages. Though these setups serve important purpose in optics and related researches, there are some disadvantages that cannot be simply ignored. For example, it takes long time training for beginners to acquire specific skills and experience to build and adjust such a sophisticated setup for optical experiment. Also, for industrial applications, systems built on free-space optics design suffer from high building cost, low mechanical stability and rigorous operation requirements. In the past two decades, the fast development of fiber optics enables several compact systems including fiber lasers, [1] optical power amplifiers [2] and fiber chemical sensors. [3] Though much more compact than their free-space counterparts, these systems are still too bulky to be used for handheld portable applications or integrated system outside a research or industry environment.

Silicon photonics, initially developed in 1980s, [4] is currently experiencing a rapid growth in order to meet the increasing demand of communication bandwidth in modern data centers, which is driven by growing data intensive applications. Though many researchers may consider any photonic devices on a planar substrate involving the material of silicon as “silicon photonics”; here, we narrow the concept of silicon photonics down to the on-chip waveguide-based integrated photonics which matches the definition in CMOS

industry. So, unless particularly specified, devices like free-space photonic crystals and dielectric Mie-resonators are not regarded as “silicon photonics” in the rest of this dissertation. [5]

Generally, silicon photonics utilizes the single-crystalline silicon nanowires on the silicon-on-insulator (SOI) substrate as an optical waveguide to propagate and process optics signals. From the point view of electromagnetic physics, silicon waveguides share nearly the same fundamental physics as optic fibers. Propagating electromagnetic field is tightly confined in a sub-micrometer wide waveguide core by total internal reflection, which is due to the refractive index contrast between high-index silicon core and low-index air/oxide cladding. Just like optic fibers, different propagating mode (e.g. TE and TM mode) of different optical properties can exist in the waveguide in meeting the requirements of boundary conditions. Silicon waveguides share many similar advantages as optic fibers. First, modern fabrication technology produces silicon waveguide with low propagation loss well within the sub-dB/cm range even though the waveguide suffers slightly higher scattering loss compared to optical fibers because of the sidewall roughness induced in dry etching step. Second, optical waveguides in nature has very low crosstalk between different channels compared to RF electric interconnects and is ideal for dense wavelength multiplexing in single waveguide and high-speed data communication. Also, the fabrication process of silicon photonics can be directly adopted from current CMOS technology and ensures its cost will eventually drop down once mass production is reached. [6] Notably, one of biggest challenges in silicon photonics is the lack of efficient on-chip light source, which is simply because of the indirect bandgap nature of silicon. In recent years, different approaches are being developed to solve this problem and they yield good

results. These methods include III-V-to-silicon bonding, transfer printing, epitaxial growth and colloidal quantum dots. [7]

As mentioned above, silicon photonics share many common properties as optic fibers. This provides a unique opportunity for researchers to explore the possibility to replicate the same applications that optic fibers have demonstrated. So far, several types of devices have been demonstrated such on-chip electro-optic modulator [8] and optical parametric amplifier. [9] More importantly, besides these applications, silicon waveguides are able to replace the free-space optical setup and minimize the optical circuit to few millimeters on a planar substrate. It offers a compact and versatile on-chip platform for repeating and revalidating optical experiments and applications that were only demonstrated in free-space optics previously. Recent years, people have witnessed several emerging field that directly utilizes silicon photonics, such as on-chip optomechanics, [10] photonic non-volatile memory [11] and frequency comb generation. [12] Specifically, silicon optomechanics combines photon-induced mechanical force with optical waveguide to achieve on-chip all-optical RF signal amplification [13] and spin angular momentum measurement of the photons in waveguide. [14] In addition, benefitted from the massive device production capability of CMOS fabrication processes, this platform can easily produce a large number of optical channels conveniently, compared to conventional free-space optic setups. This enables experiments that heavily rely on simultaneous parallel operations. For example, in the photonic deep learning application demonstrated recently, [15] the nanophotonic circuits involves up to 56 Mach-Zehnder interferometers each individually controlled by a thermal shifter with high accuracy, which is tremendously difficult to achieve in free-space optics. These examples show that silicon photonics is not

only an important addition or replacement of the free-space optics, but also further extends the scope of optical research through massive production of integrated optical channels with identical performance. It is becoming a new optic platform with unprecedented compactness for different researches in various disciplines.

1.1.2. Two-Dimensional Materials

The search for materials with extreme thinness can be traced back to the discovery of fullerene [16] and carbon nanotubes. [17] For these nanomaterials, their surfaces only consist of few-layer or a single-layer of carbon atoms. Due to their special structures, they present many unique material properties in the nanoscale such as extraordinary electron mobilities [18] and high mechanical tensile strength for carbon nanotubes. [19] However, these materials have rather unconventional three-dimensional structures which cause significant issues in their real-world applications such as electronic transistors. People have to wait for more than a decade before the successful isolation and verification of the first planar two-dimensional (2D) material consisted of a single layer of carbon atoms-graphene in 2004. [20]

Since then, the research in 2D materials has drawn the attention from both academic research and industrial development with different focuses. In a rigorous definition, 2D materials are a type of crystals that have atom layers loosely connected by weak van der Waals force in out-plane direction. While in each individual layer, the in-plane atoms are tightly bonded by covalent bonds and arranged in a regular lattice structure. Although graphene flakes should be produced every time a pencil is scratched against a sheet of paper, the controllable thinning down process to a single atom layer from multi-layer graphite pieces is unexpectedly difficult at the beginning. In 2004, to people's surprise, the first successful separation of a graphene flake is achieved simply by exfoliating a graphite piece several times with sticky Scotch tapes. [20] This surprisingly easy yet very effective method of producing monolayer materials opens the door to 2D materials research. In the next a few years, a large number of van der Waals materials have been explored and

become members of the 2D material family. To name a few early discoveries, these materials include graphene, transition-metal dichalcogenides (TMDCs) (e.g. MoS_2, $MoSe_2$ and WSe_2), [21] and boron nitride. [22] Even a decade after the first finding of graphene, the continuous effort in this area revealed new 2D materials like black phosphorus (BP) and CrI_3 and they soon become new toolkits for scientists and engineers. [23], [24]

Owning to the few-layer or monolayer thickness, the electronic band structure of 2D materials becomes quite different from their bulk forms. This is due to quantum confinement of electrons and holes in such a small volume. Thus, 2D materials exhibit many novel properties that are very different from their bulk form. For example, the broken inversion-symmetry in monolayer MoS_2 offers a large second harmonic generation which is much stronger than its bilayer form. [25] Also, the recently discovered 2D magnetic material CrI_3, has variable magnetism strength depending on layer numbers, which was never revealed in other types of bulk ferromagnetic materials. [26]

Benefitted from these unique properties, 2D materials provides many interdisciplinary research opportunities when combined with other research fields such as material science, electronics and optics. Among these research focuses, one of the most important and interesting one is the combinations of 2D material and optics/photonics. Photon, a fundamental particle with zero mass and exact energy, is an ideal tool to probe the properties of the unknown materials. In fact, many important characterizations of 2D materials rely on simple optical approaches. For example, the quick and accurate determination of the graphene monolayer is achieved by observing its Raman spectrum peaks. [27] Also, the photon-exciton interaction process in TMDCs materials can only be probed with photoluminescence measurement. [28] Moreover, in understanding 2D

material plasmonics, the plasmon wave is launched by impinging photons of certain energy and is visualized by scanning optical near-field imaging method. [29] All the above experiments and observations were not likely to happen without the help of optical cauterization method.

Besides the characterization of the 2D materials, the application of optics in 2D materials research can yield many novel applications when photonic devices are included in the picture. This only become achievable after the success of dry transfer method that can heterogeneously integrate fragile 2D material flakes on arbitrary substrate without damaging their crystal structures and introducing significant impurities. [30] 2D material thin flakes, benefited from the atomic thicknesses and weak van der Waals force between layers, can be extremely mechanically flexible compared to rigid semiconductor materials with crystal lattices (e.g. silicon). This enables a very convenient way of transferring 2D materials from one substrate (with target flake among other exfoliated flakes) onto another substrate (with target device) using PDMS stamps as long as the adhesion force are different between stamps and the substrates.

Through this straightforward yet effective method, photonic devices fabricated on a semiconductor substrate can be easily combined with 2D materials of different types. In the past a few years, many prototype devices have been demonstrated. For example, the first 2D material laser is fabricated by integrating a monolayer WSe_2 flake on a high-quality GaP photonic crystal cavity (PCC). The laser has an optical pumping threshold as low as 27 nanowatts at 130 Kelvin, similar to the value achieved in quantum-dot PCC lasers. [31] In another example, the low universal absorption of 2.3 % in monolayer graphene can be drastically improved over 60% by sandwiching graphene between periodic dielectric

Fabry-Perot cavity for photodetection purpose. [32] These examples, although show potential in the integration of photonic devices and 2D material, are still relying on free-space optics for optical illumination and signal collection. For real on-chip photonic applications, a more innovative approach is needed for the integration which inevitably requires silicon photonics.

1.1.3. Silicon Waveguide Integrated 2D Material Optoelectronic Devices

As discussed in the previous section, in order to create an on-chip 2D material photonic device, silicon photonics, as an integration platform, is one of the best options. There are several advantages. First, the current tape exfoliation technique can only produce 2D material flakes of tens of micrometers size. Considering the alignment inaccuracy in the transfer process, this would well fit the size of a silicon waveguide of a micrometer width. Second, silicon waveguide has very low propagation loss and is an efficient light delivery method to replace the complicated components in a bulky free-space optical setup. Also, it can easily provide multiple parallel optical channels for possible multiplexing applications. More importantly, the combination of 2D material and silicon photonics aims at providing possible solutions to current challenges in silicon photonics. For instance, to integrate efficient light sources on silicon substrate, two fabrication approaches can be used: direct growth and wafer bonding of the III-V gain material. However, the first approach suffers from unwanted defects caused by interfacial lattice mismatch even for the best achieved result to date, [33] and the later method increases the cost and failure rate in practical production. [34] The possible solution brought by 2D material is the heterogeneous integration through mechanical exfoliation and transfer method. By directly transferring 2D material flakes on a planar substrate, the lattice matching constraint is relaxed and the material interface can be atomic smooth with high-quality capping layers. [35]

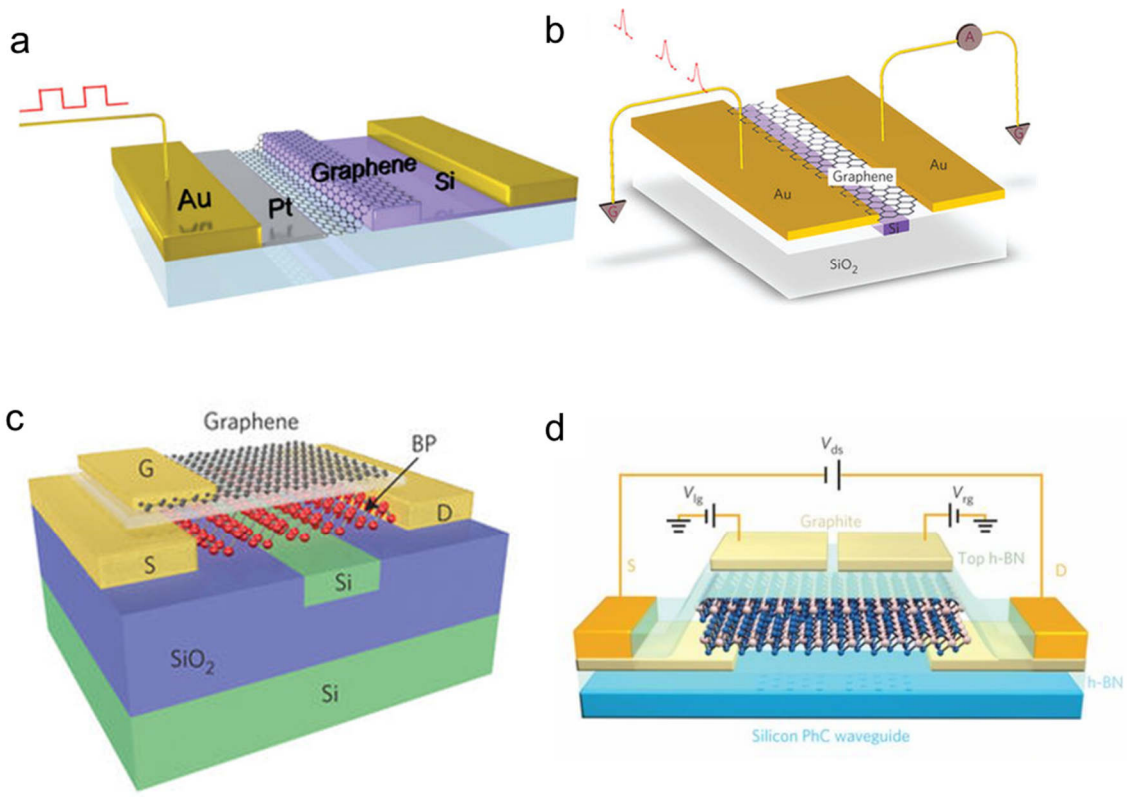

Figure 1.1. Silicon waveguide integrated on-chip optoelectronic devices. (a) Silicon waveguide integrated modulator and photodetector based on graphene in telecom band. [36], [37] (c) A black phosphorus photodetector using similar device structure. (d) Optical microscope image of the BP photodetector. [38]

Based on the heterogeneous integration method, the on-chip integration of 2D material and photonics has drawn much attention and many devices are demonstrated with different functionalities, designs and performances. The first discovered 2D material, graphene, receives the earliest attention, due to its universal optical conductivity of $e^2/4\hbar$ for a very broad range of photon energies. Also, the CVD-grown graphene, though suffering from poor quality due to polycrystalline nature comparing to the exfoliated flakes, has very large area and enables the wet transfer process when the dry transfer method is

still in its infancy. In 2011, Liu *et al.* demonstrated the very first graphene modulator integrated on silicon waveguide (Figure1.1 (a)). [36] It has a broad range of operating wavelength (1.35-1.6 μm), small device footprint (25 μm^2) and high operation speed (1.2 GHz at 3 dB roll-off), which are essential requirements for fully integrated silicon photonic system. Later, Gan *et al.* shows the first chip-integrated graphene photodetectors based on similar design, which demonstrates high photoresponsivity and 20 GHz RF photoresponse (Figure1.1 (b)). [37] For the theoretical research, a more detailed analysis pointed out three major mechanisms contributing to photocarrier generations: photovoltaic, thermoelectric and photo-induced bolometric effects. [39] This analysis is among the first to reveal the underlying photo-carrier generation process in a 2D material device and provides important insights for the improvement of the design in new photonic 2D devices. Despite the initial success, however, graphene based optoelectronic device suffers from very high dark current because of its semimetal zero-bandgap nature. This also limits the efficient modulation of channel conductance by externally applied electrical field which leads to low on/off ratio. To resolve these challenges, different 2D materials with direct and non-zero band gap are explored to replace graphene as the active material in integrated device. In 2014, soon after the discovery of black phosphorus (BP), [24] Youngblood *et al.* demonstrated the very first waveguide integrated photodetectors with BP flake instead of graphene (Figure1.1 (c) (d)). [38] Compared to similar device based on graphene, the device shows negligible dark current and much higher on-off ratio with reasonable gate voltage modulation. In addition, the device photoresponsivity reaches up to 135 mA/W for 11.5 nm flake with the sacrifice of RF bandwidth limited to 3 GHz at 3 dB roll-off. In 2017, a new 2D TMDC material, $MoTe_2$, is integrated on photonic crystal waveguide as an on-

chip integrated light source based on a double-gate PN junction design. [40] This electrical pumped 2D light source achieved light emission at 1160 nm wavelength with an external quantum efficiency of 0.5%, which is the first practical waveguide integrated light emitting diode using 2D material as optical gain material.

In summary, the on-chip heterogeneous integration of 2D materials and silicon waveguide has simplified the conventional free-space measurement setup considerably by using the planar substrate and top-down fabrication. Moreover, it also produces possible solutions to current challenges in silicon photonics applications and shines light on the fundamental research of light-matter interaction in nanoscale.

1.2. Surface Enhanced Spectroscopy for Sensing Applications

1.2.1. Surface Enhanced Raman Spectroscopy (SERS) and Surface Enhanced Infrared Absorption (SEIRA) Spectroscopy

Biosensing is generally defined as the detection and identification of biological materials such as tissues, cells, enzymes, antibodies, and other natural products through measuring dependent variables such as electrical resistivity, mechanical response, optical absorption and temperature. [41] Many types of sensors based on different working principles have been developed over the years. These include thermochemical, electrical-impedance-based, piezoelectric and optical sensors. [42] They are widely used in applications like disease diagnosis, medicine development and environment pollutant monitoring. [43] The sensing outcomes of these applications almost completely rely on the sensitivity and identification capability of the sensors used. Thus, tremendous effort has been made to improve the performance of these sensing devices.

Among these sensors, optical sensors have unique advantages such as high tolerance to electrical noise, broad operation wavelength, reliable chemical identifications and label-free measurement. In the category of optic sensors, plasmonic sensors hold a special place with its unprecedented sensitivity. The fundamental physics behind the plasmonic sensors is the surface plasmon polaritons (SPP), which is defined as the collectively oscillation of free electrons on noble metal surface excited by impinging photons in visible or infrared wavelengths. [44] This coherent electron oscillation, which can be confined in a small volume far below conventional diffraction limit, significantly enhances local electromagnetic field and leads to boosted light-material interaction in its

close vicinities. [45] Thus, the sensitivity of plasmonic sensors can be dramatically improved as the refraction index change in the device surroundings is significantly amplified. It soon catches the attention of biosensing research community and many results are presented. For example, visible-wavelength plasmonic sensors based on local surface plasmon resonance (LSPR) have very high sensitivity and measurement accuracy. This is because the surface plasmon excited at the metal/dielectric interface of metallic nanoparticles can covert a very minute change of local refractive index induced by unknown analyte to a spectral shift in nanoparticle extinction and scattering spectra. [46]

The shifts of spectra are only capable of measuring binding events and rates of arbitrary types of molecules. To identify the species of the unknown analyte, a closer examination of the optical spectroscopy is needed. Currently, there are two commonly applied plasmonic-based molecule identification approaches: surface enhanced Raman spectroscopy (SERS) and surface enhanced infrared absorption (SEIRA) spectroscopy. Raman scattering, different from elastic Rayleigh scattering, is the inelastic scattering of impinging photons through different energy levels of molecular vibrations/rotations. Thus, the scattered photons have energies that are either Stokes or anti-Stokes shifted compared to original pump photon energies. By observing the spectral positions and strengths of the emission peaks, the unknown molecules can be detected and identified. Intrinsically, Raman scattering is an extremely weak phenomenon in most molecules because of the very small scattering cross-section (e.g., $\sim 10^{-28}$ cm^2 $molecule^{-1}$ for the stretching vibration of benzene molecule) [47] and its direct observation is even more challenging for a small volume analyte. Conventionally, a high-power ultrafast laser and an extremely sensitive spectrometer are necessary. For SERS technique, through the plasmonic enhanced

electromagnetic field in the vicinities of noble metal surfaces, both the pumping and emission electromagnetic field experienced the same boost. So, the Raman emission signals experience a strong boost up to $|E_{pump}|^2 \cdot |E_{Raman}|^2$ in total enhancement as long as the Stokes shifted wavelength is close to the pumping photon wavelength. Because of the enormous nonlinear optical enhancement, a large effective Raman cross-section was reached (~10^{-17}-10^{-16} cm^2/molecule) and the observation of single molecule is successfully achieved in an aqueous colloidal silver solution. [48]

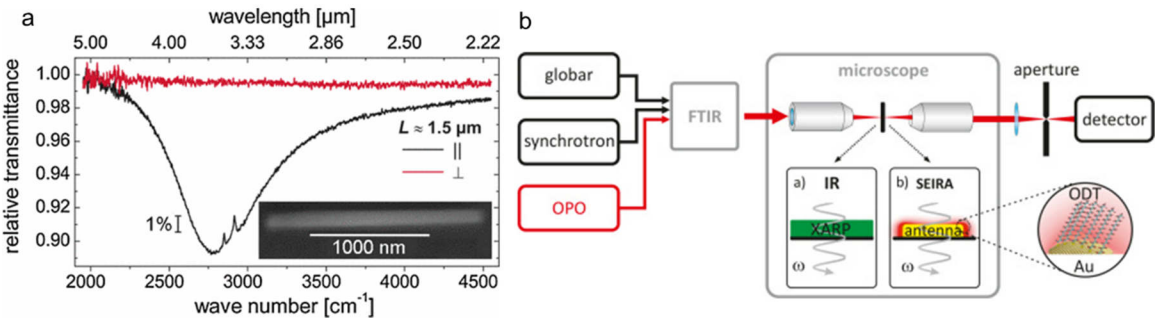

Figure 1.2. Different types of light sources used in SEIRA sensing techniques. (a) Relative IR transmittance of a gold nanowire with one ODT monolayer using a synchrotron IR source. Inset: Scanning electron micrograph of a gold nanowire.[49] (b) Schematic illustrations of a OPO laser combined with FTIR microscope spectrometer for both conventional IR spectroscopy and SEIRA detection of monolayer analyte. [50]

SEIRA is another spectroscopic sensing approach and it has rather straightforward working mechanism in comparison to SERS. It is the direct measurement of absorption peaks induced by the molecular bond vibrations in mid-infrared wavelength range. The absorption peak positions of different chemical bonds are their natural fingerprints and enable the direct detection and identification of the molecules in unknown analytes. The

IR absorption cross-sections of molecular absorptions are much larger compared to Raman process (e.g., ~10^{-19} cm^2 $molecule^{-1}$ for the C-H bond stretching). However, because it is a linear optical process, the expected enhancement signal is only proportional to $|E_{incident}|^2$ in a plasmonic enhanced electromagnetic field, only a square root of the enhancement factor SERS technique can offer. Although the first SEIRA experiment can be traced back to 1980s, [51] for quite a long time, SEIRA technology does not draw much attention from researchers and its advancement is behind SERS technology.

In recent years, benefitted from the improvements of fabrication techniques and experimental approaches, more researches focus on SEIRA technology as a complement to SERS. The plasmonic enchantment of the SEIRA signals can directly benefit from very small metallic features because of the tight confinement of electromagnetic field in it. The recent advancement to nanometer scale in the top-down CMOS fabrication enables fast and reliable production of extremely features on a planar substrate. As an example, patterning methods including focused ion beam (FIB) and electron-beam lithography (E-beam) can fabricate nanosize gaps as small as 5 nm reliably. Novel fabrication method using atomic layer deposition (ALD) can create large number of nanogap of width as small as 9.9 Å simultaneously and pack up to 150,000 such devices on a single 4-inch wafer. [52] In the meantime, the application of new experimental techniques also helps improve the SEIRA technology, especially the use of new types of light sources. For example, in 2008, by using high-quality mid-infrared synchrotron light source and ultra-smooth gold nanowires in the experiment, the detection of the self-assembled monolayer (SAM), Octadecanthiol, is demonstrated by measuring the extinction spectrum of a single nanorod

antenna (Figure 1. 1-1(a)). [49] However, synchrotron source has very high cost and is not widely accessible to researchers. Instead, based on the difference frequency generation (DFG) in optical parametric oscillator (OPO), tabletop high-brilliance light source can replace the thermal globar source in a conventional FTIR setup as in Figure 1. 1-2(b). [50] The coherent source has four orders of magnitude higher brilliance than thermal source and very low noise. The result shown by Giessen's group offers ten times faster acquisition speed in a single antenna SEIRA measurement and an effective sample area size down to 5 μm (in diameter) limited by optical diffraction constraint of conventional IR objective lens.

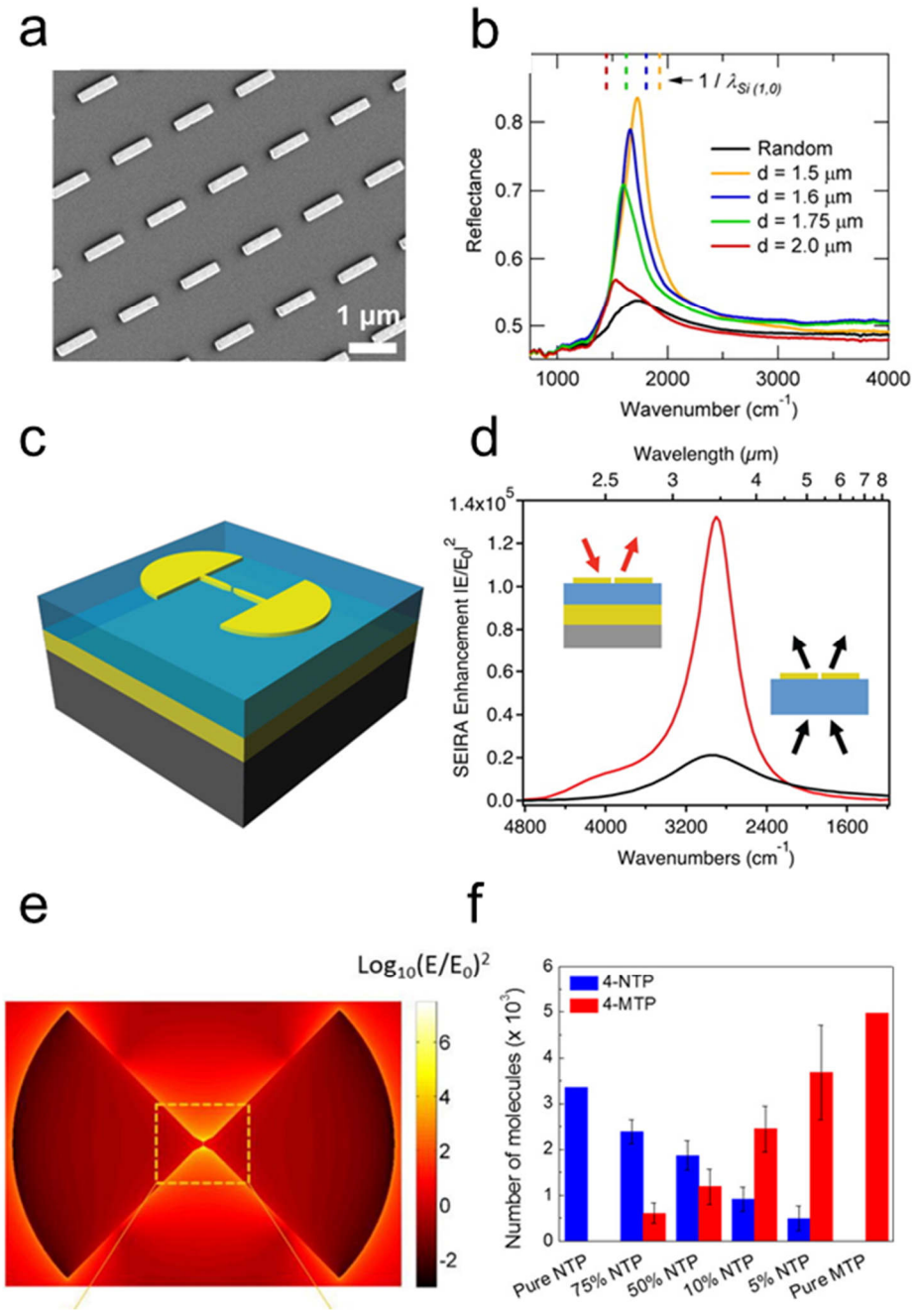

Figure 1.3. Different plasmonic device designs for SEIRA application. (a)(b) Rectangular array of nanorod antennas and its IR reflection spectrum for different periods. (c) Fan-shaped plasmonic antennas with bottom reflectors.[53] (d) Simulated SEIRA enhancement for a fan antenna on a reflective substrate (red) and a fan antenna on a normal transparent substrate (black) [54] (e)

Electrical field intensity distribution for bowtie antenna with sub-3 nm gap width in log scale. (f) Numbers of 4-NTP and 4-MTP molecules on Au surface in the nanosize gap for different chemical mixtures. [55]

Besides the improvements in nanofabrication techniques and experiment approaches, more advanced and sophisticated device designs also expand the capability of SEIRA technology. At first, optical antennas only have relatively simple geometries and arrangements due to the lack of well-developed theoretical knowledge. One of the very first demonstration of SEIRA is based on the nanorods arrays arranged in a square lattice, as in Figure1.3. (a)(b). [53] Comparing to the single nanorod antenna, the near-field interaction between neighboring nanorods increase the electromagnetic field intensity at nanorod tips and enable the identification of two Amide bonds with a 4-nm thick silk protein film. In another attempt, Brown *et al.* proposed and fabricated a fan-shaped antenna design and added another reflective layer underneath the substrate in reflection spectrum measurement. (Figure1.3 (c)) The fan-shaped antenna design can funnel more optical power into the plasmonic hotspot. The metallic reflective layer can form a constructive optical interference on the plasmonic devices, and thus recycle the optical energy transmitted through the device. This significantly increases the intensity enhancement factor up to seven times (Figure1.3 (d)) and the detection of monolayer ODT in 3.5 μm wavelength range with only nine antennas is demonstrated. In 2017, the same research group reported that by applying a more complicated lift-off technique, sub-3 nm gap can be created with high repeatability. This extremely small gap yields a theoretical SEIRA enhancement factor over 10^7. Benefitted from this enhancement, the detection and quantitative analysis of different SAM molecules (NTP and MTP) in a mixture are

demonstrated, as in Figure 1.3. (e)(f). [55] All these improvements in device design, combined with the progress of fabrication techniques and measurement approaches, greatly expands the applications of SEIRA sensing, making it a competitive candidate in spectroscopic biosensing. More importantly, the few antennas required in the experiment, the high coherence of laser source and the reliability of nanofabrication, enable the SEIRA application to be achieved in a more compact form on silicon chip.

1.2.2. Direct Integration of Plasmonic Antennas and Silicon Waveguide

The combination of plasmonic antennas and silicon waveguide can be implemented in a rather straightforward way: simply fabricate the antennas on top of the waveguide and measure through waveguide transmission. This idea becomes possible with accurate estimation from 3D numerical simulation (e.g. FDTD and FEM) and precise lithography alignment down to nanometers. By fabricating plasmonic antennas of different geometries and designs on the waveguide, different functionalities can be achieved. These pioneering attempts, although not all focusing on the sensing application, yield important results that eventually could lead to the on-chip plasmonic-waveguide sensing platform.

One straightforward application can be achieved is to couple free-space optical signals to waveguide through the nanoantennas. The nanoantennas serve as a metallic grating coupler; however, the area of the antenna array can be extremely small and the function can be more complicated. For example, a very compact plasmonic nanoantenna array integrated on silicon waveguides can allow polarization-dependent, mode-selective, and directional waveguide coupling at 1550-nm wavelength (Figure 1.4(a)). In this report, [56] by properly designing and constructing several metallic nanorods closely on waveguide, the coupling of free-space optical signals to propagating waveguide mode is demonstrated. Also, taking advantage of the phase delay of each individual nanorod for constructive/destructive interference, free-space light of orthogonal polarizations can be coupled to either TE or TM waveguide modes with high unidirectionality (Figure 1.4 (b)(c)). Moreover, this free-space/waveguide plasmonic interface can transmit optical signals with modulation frequency up to 10 GHz, which paves the path for a functional compact mode demultiplexer.

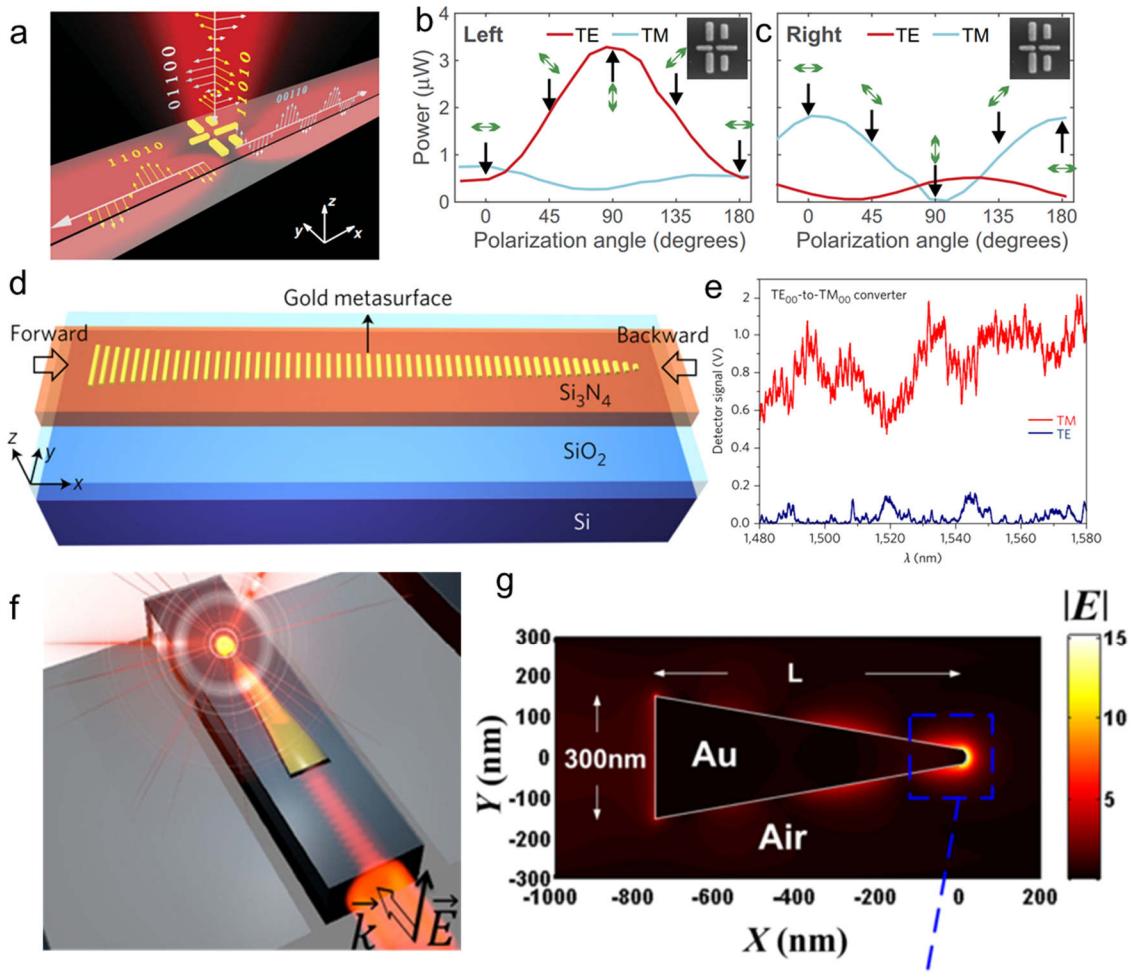

Figure 1.4. Direct integration of plasmonic nanoantennas with photonic waveguides. (a) High–bit rate ultra-compact light routing with mode-selective on-chip nanoantennas. (b)(c) Transmission spectra at both the left and the right waveguide end for the antenna, confirming the coupling of y-polarized (x-polarized) light to the TE mode (TM mode) to the left (right). [56] (d) Schematic of a device with integrated metasurface. (e) TE and TM components at the output port of a mode converter, showing that the device operates over a broad wavelength range. [57] (f) Schematic illustration of the plasmonic concentrator integrated on silicon ridge waveguide. (g) Simulation result of the device showing a high electric field at the tip of the metallic concentrator. [58]

Besides the free-space/waveguide coupling function that plasmonic antennas can offer, the conversion between different silicon waveguide modes can also be achieved by waveguide integrated plasmonics. [57] *Nanfang*'s group integrated a metallic metasurface consisting of multiple nanorods with gradually changing geometries on top of a silicon waveguide (Figure 1.4(d)). By optimizing the geometries and optical phase delays of the nanorods, the phase of the waveguide mode is distorted by nanoantenna array. They demonstrated the symmetric transmission of TE mode: the mode is converted to TM mode when propagating in one direction and gets completely absorbed when propagating in the other direction. This device can be used as a mode converter with broad operating bandwidth, as shown in Figure 1.4(e). In another example, a simple triangular plasmonic light concentrator is integrated on top of the waveguide (Figure 1.4(f)). By converting the waveguide mode to plasmonic mode through mode hybridization, the nanotaper can concentrate the light from the waveguide into a very small spot on the taper tip. Thus, a high electric field is created. Though the enhancement is only 15, which may be limited by the fabrication process and less optimized device design, it is an important step towards creating a plasmonic hotspot based on the light delivery of silicon photonics.

1.2.3. Spectroscopic Sensing Based on Silicon Waveguide

Currently, most surface enhanced spectroscopy sensing applications are implemented using free-space FTIR microscope measurement setup. These table-top systems are good choices for a research lab environment; yet, they are still complicated systems that take large spaces and require dedicated maintenance. Also, except for a handful of reports attempting to use few or single plasmonic devices, [49], [54], [59] most of the spectroscopic sensing experiments involve hundreds to thousands of nanoantennas in a aqueous solution or on a planar substrate in order to have a good signal-to-noise ratio. This further limits the size scaling of the sensing chip. To produce a sensing system with a very small form factor and a reasonable detectivity, one plausible approach is taking advantage of silicon photonic waveguide as an efficient light delivery tool and high-brilliance laser as light source. So far, there are several reports utilizing the waveguide integrated spectroscopic sensing approach. Though some of them are not based on plasmonic enhancement, a brief review of these experiments is presented below for understanding the technical details associated with this idea.

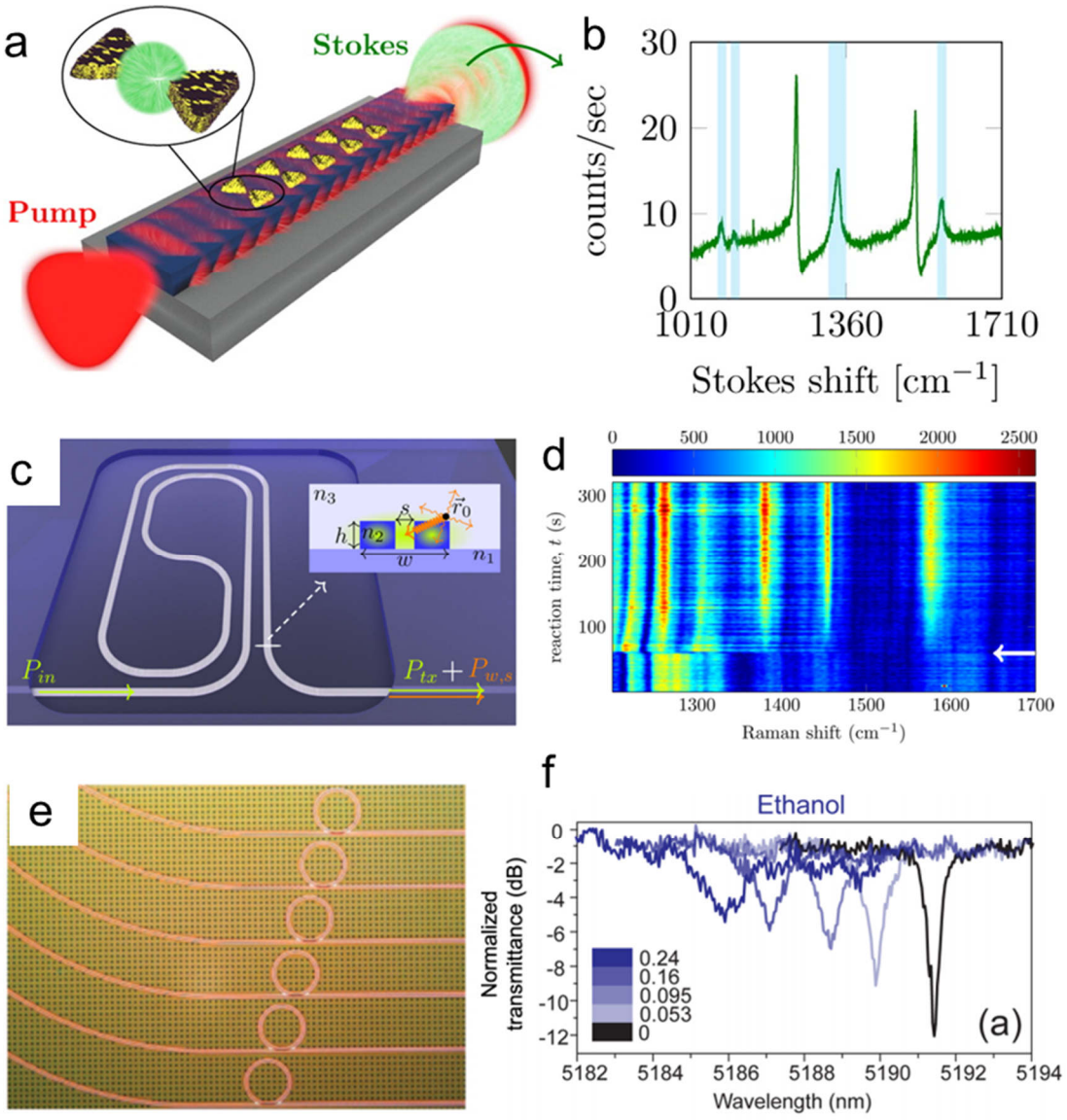

Figure 1.5. Silicon waveguide integrated sensing applications. (a) Single mode silicon nitride waveguides with an array of gold bowtie antennas. (b) Raman spectra of NTP peaks collected from waveguide.[60] (c) NWERS system based on a generic slot waveguide design. (d) DNA hybridization process using NWERS. Raman spectrums as a function of reaction time. [61] (e) Optical microscope images of the silicon ring heterogeneously integrated on CaF_2 substrate. (f) Mid-IR optical transmission spectrum of a ring resonator in ethanol/cyclohexane solutions of different nominal concentrations. [62]

One of the most recent waveguide sensing results is the on-chip SERS sensing application. [60] Due the high absorption of silicon waveguide, silicon nitride waveguide is used instead to support propagating mode in visible wavelength. A dozen of metallic bowtie structures are integrated on top of the waveguide. The waveguide is used as both a light input and a signal collection ports in the experiment as shown in Figure 1.5 (a). This attempt successfully demonstrates the detection of 4-nitrothiophenol (NTP) monolayer coated on the surface of gold antennas by identifying Stokes peaks in the waveguide transmission spectrum (Figure 1.5 (b)). Later, the same group reported result using on-chip nanophotonic waveguide enhanced Raman spectroscopy (NWERS). [61] Instead of adding plasmonic antennas atop the waveguide, the waveguide is redesigned as a slot waveguide instead of a rectangular waveguide. The center of the waveguide is hollow so that the unknown analytes can fill the waveguide and directly interact with the propagation mode of the waveguide. Due to the extremely long interaction length of the waveguide, Raman signal can gradually accumulate and be enhanced even without plasmonic antennas. Using this technique, the observation of real-time immobilized DNA hybridization process (Figure 1.5 (d)) and an accurate and direct measurement of the density of biotin-streptavidin complex submonolayers are presented.

The abovementioned two experiments are all carried out in visible wavelength range using Raman scattering spectroscopy. In order to create similar application in mid-IR range, several changes need to be made. First, new light sources like quantum cascade lasers (QCL) and OPO sources need to be used, which are quite expensive. Also, although silicon maintains a high transparency in mid-IR range, the high absorption in silicon oxide becomes detrimental and hinder the use of cheap SOI wafer in this band. To overcome this

issue, Chen *et al.* managed to transfer the prefabricated silicon waveguide from the opaque SOI substrate to the transparent CaF_2 substrate for mid-IR band chemical sensing. [62] Using this method, high Q-factor ring resonators in mid-IR wavelength are heterogeneously integrated on the CaF_2 substrate. After the device is exposed to a chemical solution, by measuring the ring resonance dip wavelength shift and extinction ratio change in transmission spectrum, the information regarding the concentration and species of the solution can be well extracted (Figure 1.5 (e)(f)).

These examples mentioned demonstrate different on-chip sensing mechanisms. Though still far from a completed on-chip integrated SIERA sensing platform, they provide important building blocks for such a device.

1.3. Dissertation Outline

The outline of the dissertation is presented below.

In Chapter 1, the background knowledge of my research is presented. The first section includes a brief introduction of silicon photonics (focus on silicon waveguide), two-dimensional materials and their combinations. This serves as an introduction to the integration of 2D materials and silicon waveguide. Next, the surface plasmonics are introduced with focus on the spectroscopic sensing including the SERS and SEIRA techniques. Experiments of directly fabricating plasmonic nanoantennas on top of waveguide are briefly discussed. Also, a very short review on the chip-scale sensing applications is presented.

In Chapter 2, a three-dimensional integration approach of silicon waveguides, plasmonics and 2D material is demonstrated. This vertical device architecture takes advantage of the low propagation loss of silicon waveguide and the high field enhancement in the plasmonic nanogap. Combined with the very thin 2D material flake, black phosphorus, a photodetector in telecom band is demonstrated with high on-off ratio, good intrinsic responsivity and reasonable high-speed responsivity.

In Chapter 3, the research focus is shifted from telecom band to the mid-IR range and the on-chip SEIRA sensing application is explored. An array of metallic nanorods, as a plasmonic resonator, is directly fabricated on top of a mid-IR silicon waveguide. The strong coupling between the waveguide and resonator is verified by the transmission spectrum measurement and the plasmonic-enhanced optic hotspot is confirmed through

FDTD simulation. Utilizing the hotspot, the absorption peaks of CH-bond in PMMA and monolayer ODT are successfully measured.

In Chapter 4, we summarize the contents presented in the dissertation and provide an outlook of the future perspective in this integration approach.

Chapter 2. Integration of Black Phosphorus Photodetector with Silicon Photonics and Plasmonics

2.1. Black Phosphorus

As mentioned in Chapter 1, for a rather long time, 2D material research focuses on graphene and transition-metal dichalcogenides (TMDCs). They have shown many unique properties that provide important insight for condensed matter physics research. However, in practical optoelectronic applications, the limitations of these two popular materials are apparent. For example, the semimetal graphene has zero bandgap causing low on-off ratio for FET and high dark current for photodetecting applications. On the other hand, monolayer TMDCs materials has large bandgap and carrier can be excited by photons in visible wavelength, which hinders its optoelectronic application in telecom band.

In the search for new van der Waals semiconductors, one of the nearest neighbors of silicon, phosphorus, has been used as an n-type dopant in silicon for very long time. However, due to the unstable nature of white and red phosphorus in room environment, the application of phosphorus as a stand-alone semiconductor has long been ignored. In 2014, Li *et al.* first isolated few-layer black phosphorus (BP) from its bulk crystals and explored the application of BP as a 2D semiconductor material. [24]

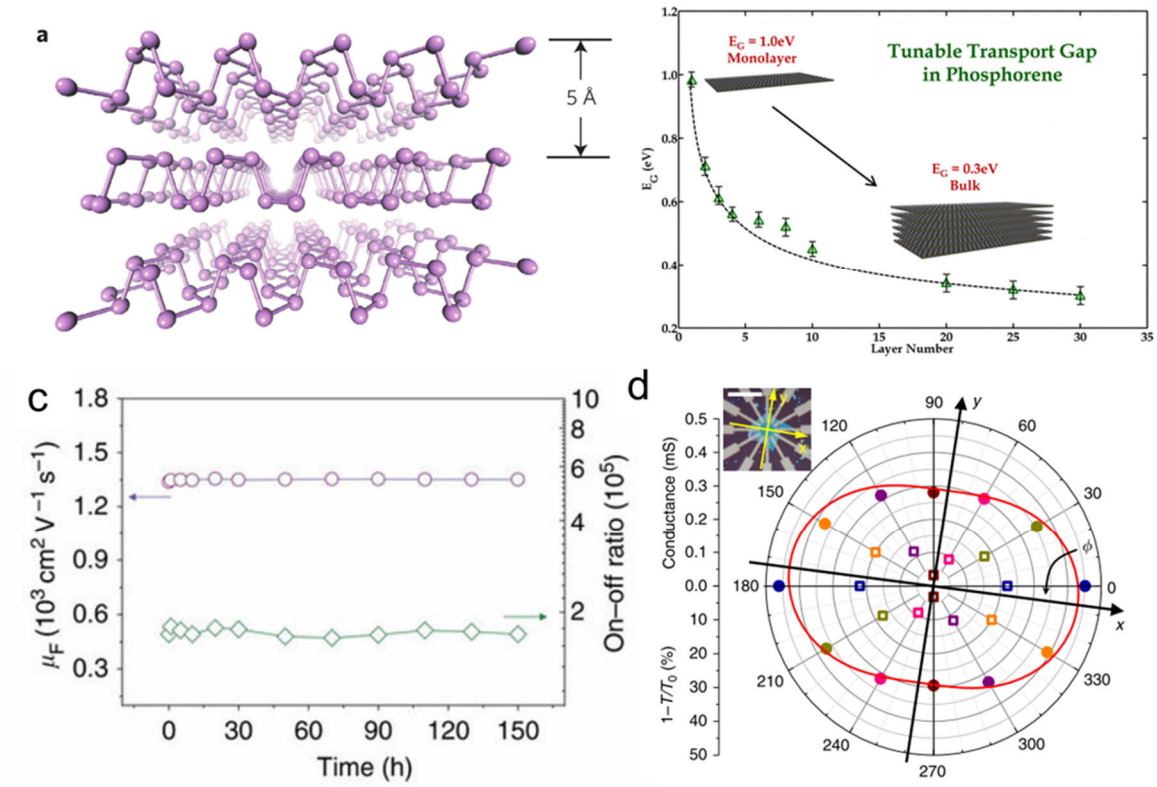

Figure 2.1. BP material and optoelectronic properties. (a) Black phosphorus crystal structure showing puckered layers. [24] (b) Layer dependent tunable band gaps of black phosphorus. [63] (c) Room-temperature hole mobility up to 1350 cm^2 V^{-1} s^{-1} and on-off ratio over 10^5 of BN sandwiched BP FET. [64] (d) Angle-resolved anisotropic electrical conductance and infrared (2700 cm^{-1}) optical absorption of BP. [65]

Black phosphorus is a stable isotope of phosphorus in the ambient environment and can be easily synthesized by heating red phosphorus at high pressure and temperature. [24] It shares similar crystalline structure as other 2D material with interlayer van der Waals force and in-plane covalent bonding between atoms. However, each atom layer has a puckered surface due to sp^3 hybridization (Figure 2.1 (a)). Black phosphorus has a direct bandgap even for few-layer form and it is dependent on the number of atom layers (Figure 2.1 (b)). The band gap of BP is estimated to be about 1-2 eV in monolayer. When the

number of layers increase, due to the reduced confinement of electrons, BP direct bandgap reduces to ~0.3 eV. [24], [63] This property is highly desired for infrared optoelectronic devices as it also provides very low dark current. Beside the tunable direct bandgap, BP also has other superior properties. For example, when BP layer is sandwiched between high-quality insulating boron nitride (BN) layers, the interface can be atomically smooth compared to dielectric capsulation (i.e. ALD capsulation [66]). Its hole mobility can reach up to ~1,350 $cm^2 V^{-1} s^{-1}$ at room temperature and on-off ratios exceeding 10^5 (Figure 2.1 (c)). At low temperatures, the mobility even reaches ~2,700 $cm^2 V^{-1} s^{-1}$ [64]. In addition, comparing to other 2D material, BP has strong in-plane anisotropy in both electronic conductance and optical absorption. This adds another tuning knob in engineering BP device (Figure 2 .1 (d)). In a word, black phosphorus, as a newly discovered 2D material, has many unique properties that were not available in other 2D materials and is an ideal candidate for infrared optoelectronic applications.

2.2. Project Motivation

As discussed in previous sections, 2D materials including graphene, TMDCs, BP, and many others, offer novel optoelectronic properties that are very promising for a wide variety of photonic applications. [67] Optoelectronic devices based on these materials (e.g. photodetectors, optical modulators, light emitting diodes, and lasers) have been demonstrated with performances approaching, and sometimes rivaling, their commercial counterparts. [68]–[70] For instance, graphene photodetectors with over 30 GHz RF frequency response has been demonstrated in telecom band. [68], [69] Black phosphorus photodetector in mid-IR band is presented with unprecedented high gain factor. [71]

However, we should note that for these materials, most of the extraordinary electrical and optical properties are the direct results of their low dimensionality, which provides out-of-plane quantum confinement and altered properties from their bulk counterparts. Also, the extreme thinness of monolayer or few layers greatly restrains the light-matter interaction process, and consequently limits the optical absorption, electro-optic effects, and nonlinearity. For instance, while graphene has a remarkable universal absorption of 2.3% per layer over a broad range of spectrum, this small percentage is far from almost any practical application (e.g. optical communication). To address this issue, several methods have been implemented to enhance light-matter interaction in 2D materials. Integrating 2D materials directly with planar photonic waveguides can extend the interaction length along the longitudinal direction of the 2D material, but at the expense of a very large footprint. [36]–[38], [72], [73] The increased footprint often causes issues including high energy consumption, high insertion loss and more importantly, the scaling

potential of the fabricated device. Alternatively, embedding 2D materials in high-Q optical cavities (e.g. ring resonators and photonic crystals) can resonantly boost the light-matter interaction, but only within the narrow band of the cavity resonance.[32], [74] In addition, nanoplasmonic structures can focus impinging optical field to hotspots under conventional diffraction limit and thus dramatically enhance light-matter interaction over a wavelength range much broader than dielectric optical resonators.[45], [75]–[81] However, metallic plasmonic devices suffer from intrinsic Ohmic loss due to use of noble metal and thus are not suitable for long-distance propagation of optical signals when compared to dielectric waveguide.

Based on the above considerations, it becomes obvious that the optimal approach would be designing a hybridization platform combining dielectric and plasmonic structures. Thus, it is possible to take the advantages and avoid the drawbacks of both platforms. There have been previous efforts to achieve such dielectric-plasmonic hybrid systems, such as hybrid waveguides to alleviate metal loss[82]–[86], integrating plasmonic nanoantennas directly on silicon photonic waveguides [58], [60], and low-loss couplers between silicon and plasmonic waveguides[87], [88]. Yet, a silicon/plasmonic device integrated with 2D materials has not been demonstrated to date.

In this project, a new hybrid architecture is presented by integrating silicon photonics, plasmonic nanostructures, and a 2D material to construct a monolithically integrated photodetecting device. On this hybrid platform, infrared (IR) light is delivered *via* the silicon waveguide over a long distance, converted to surface plasmon polariton (SPP) waves, and concentrated within a plasmonic nanogap, on which the 2D material is integrated. For the 2D material, we use black phosphorus (BP), which is very attractive in

optoelectronics for its direct and tunable bandgap ranging from ~2 to 0.33 eV as the thickness increases from a monolayer to tens of nanometers. [24], [63] BP is known to have good sensitivity in the near- and mid-IR regimes and various optoelectronic devices have been demonstrated such as a multispectral imager, [89] polarization sensitive, [90] waveguide integrated near-IR, [38] and mid-IR photodetectors. [71] As we have discussed above, these devices suffer from either low responsivity when excited with normal incident light or a large device footprint when using a waveguide-integrated configuration.

2.3. Device Design and Fabrication

2.3.1. Structure Overview

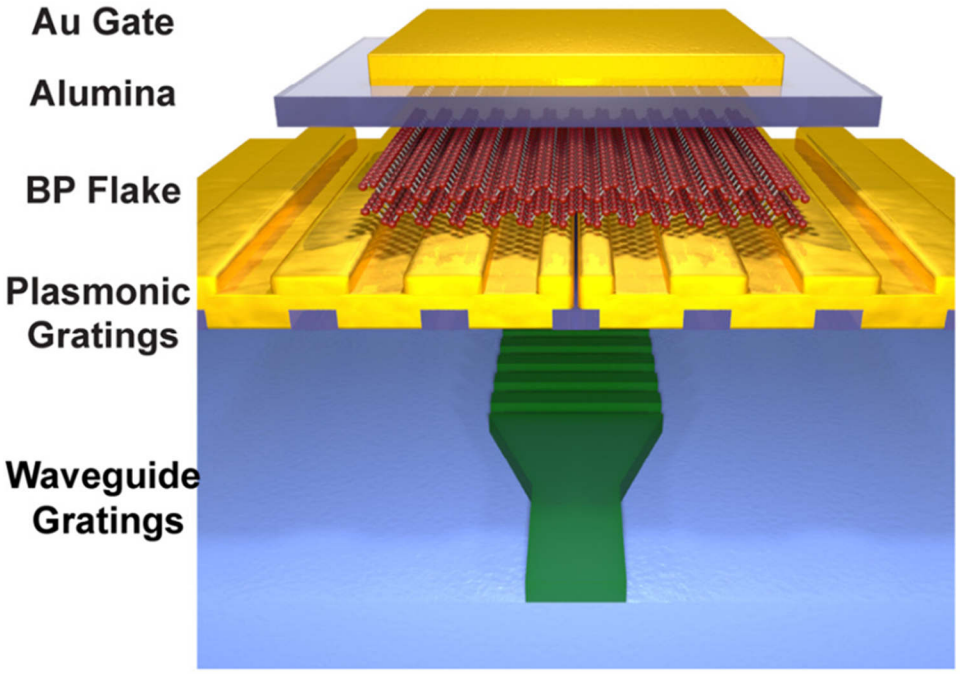

Figure 2.2. The artistic illustration of 3D hybrid structure consisting silicon photonics, nanoplasmonics, and black phosphorus.

The overall structure of the demonstrated hybrid system with a 3D architecture is illustrated conceptually in Figure 2.2. It consists of three layers built on a standard silicon-on-insulator (SOI) substrate: the bottom layer includes a silicon photonic waveguide with low propagation loss; the middle is the plasmonic layer comprising a metal grating and a nanogap; the top layer consists of an exfoliated BP flake that is in direct contact with the metallic nanogap. A grating is patterned on the waveguide underneath the plasmonic structure to launch light out-of-plane through a spacing layer, thus coupling light from the

waveguide to the nanogap. The output light from the waveguide grating (fundamental TE waveguide mode) is polarized in the x-direction which is perpendicular to the nanogap direction. The metallic grating in the plasmonic structure converts the emission from the waveguide grating to an SPP wave and focus it into the nanogap, where significantly enhanced optical intensity is achieved. It's notable that the metallic grating is fabricated by direct deposition of gold on pre-patterned hydrogen silsesquioxane (HSQ) resist, which provides a very smooth metal-dielectric interface with reduced scattering loss. In addition, another layer Al_2O_3 is deposited on top of BP flake as a capping layer and gate dielectric layer. A top metal layer is fabricated as electrical modulating gate and optical reflecting layer.

2.3.2. Silicon Photonic Layer Design

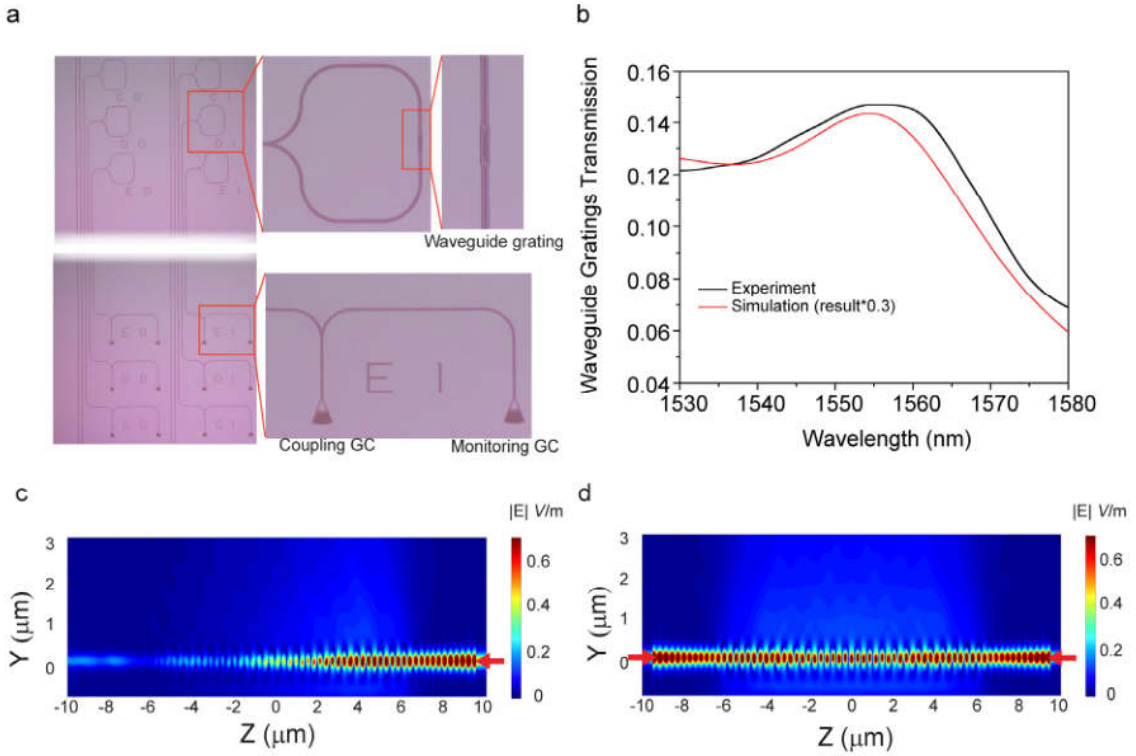

Figure 2.3. Photonic layer design and measurement. (a) Microscopic images of photonic layers. Two grating couplers (GC) are shown in right lower panel. Racetrack waveguide and waveguide grating are shown in the upper panel. (b) Measured waveguide grating transmission and simulated result. The transmission is normalized to the optical power in waveguide. (c) (d) Simulated (FDTD) E-field amplitude |E| for the waveguide grating cross-section (along light propagation direction) for (c) light input from right end only and (d) light input from both ends (indicated by red arrows).

Here, we delineate the design of bottom silicon photonic layer. As shown in Figure 2.3 (a), the silicon photonic layer has two grating couplers (GC). The left GC is used to couple laser light from fiber arrays into waveguide and the right one is used to monitor coupling efficiency after the first Y-junction waveguide split. The second Y-junction divides light into two waveguides, which then recombine in the waveguide grating. The

measured waveguide gating transmission spectrum (normalized to optical power in waveguide) is shown in Figure 2.3 (b) along with simulated spectrum. The experiment and simulation spectra have similar outlines. However, measured waveguide grating efficiency is only around 30% of the simulation result. We believe that this may be due to variations and imperfections in the fabrication process.

Figure 2.3 (c) (d) shows the simulated (FDTD) electric field amplitude distributions of the waveguide grating cross-section view. In Figure 2.3 (c), only one mode source is added in the simulation and injects light from right side. In Figure 2.3 (d), two mode sources are added on both sides of the waveguide grating and inject light simultaneously with wave vectors of opposite signs. Apparently, from the field distribution, the second design results in a better uniformity of the output wave front, comparing to single light source case. This is more desirable for our application to couple light into plasmonic structure on top of silicon waveguide grating. Therefore, in our silicon photonic layer design, the light is split into two waveguides through the second Y-junction before emitted by waveguide grating.

2.3.3. Plasmonic Layer Design

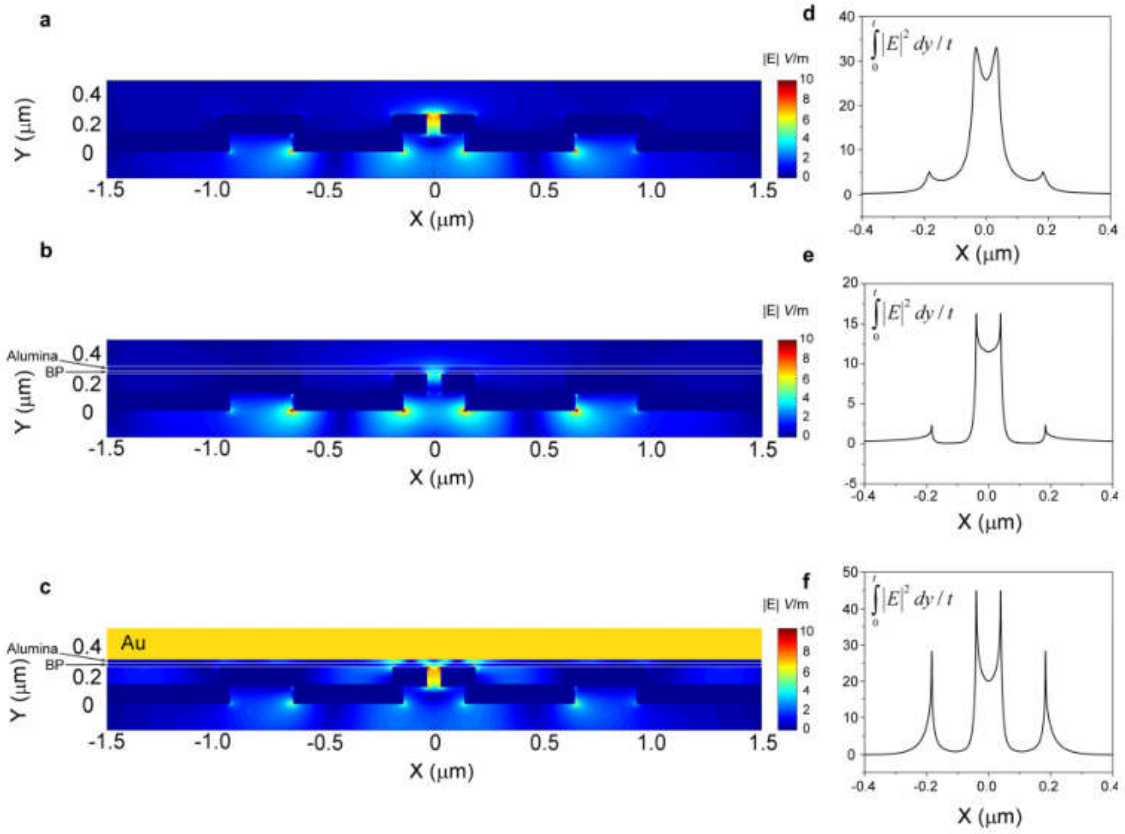

Figure 2.4. Two-dimensional FDTD simulation of plasmonic effect in devices including different layers. Simulated electric field amplitude |E| distribution (left side) and average optical intensities within 20 nm above plasmonic gratings (right side) of devices including different layers: (a) (d) only metallic plasmonic gratings, (b) (e) BP and alumina are on top of metallic gratings, (c) (f) completed device with BP, alumina and top metal gate.

For the design of the middle layer, plasmonic metallic gratings, three individual cases need to be carefully considered: 1) stand-alone metallic gratings, 2) metallic gratings covered with 20 nm BP flake and Al_2O_3 capping layer, 3) completed device with top Au gate. In order to verify plasmonic enhancement and gate metal reflection, 2D FDTD

simulations are performed for the device including different layers. Given the very large aspect ratio of the nanogap, 60 nm width and 25 µm length, simulations in two-dimension provide sufficient precision and the full 3D simulations are rather unnecessary. Figure 2.4 (a) shows the electric field distribution in metallic gratings. Figure 2.4 (d) is the averaged optical intensity 20 nm above the top of plasmonic gratings. Figure 2.4 (b) shows the electric field amplitude when BP and alumina layers are included in the simulation. Figure 2.4 (e) is the average optical intensity inside BP layer (20 nm). This corresponds to an ungated device. In Figure 2.4 (c), the electric field distribution of the completed device (including top metal gate) is shown. The average optical intensity in BP layer (20 nm) is shown in Figure 2.4 (f). Comparing Figure 2.4 (e) and (f), it is obvious that by adding a metal gate, optical intensity inside the BP flake is further enhanced, which should increase total optical absorption subsequently. The detailed design parameters for the plasmonic structure are presented in Figure 2.5 and Table 2.1.

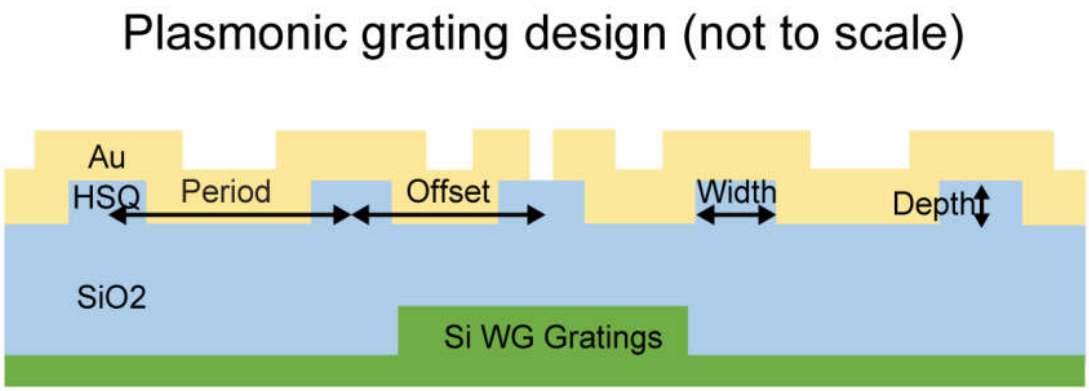

Figure 2.5. Plasmonic grating cross-section structural view and key design parameters.

Parameters	Offset	Period	Width	Depth	Metal layer
Values	0.78 µm	1 µm	0.28 µm	~120 nm	3 nm Ti/120 nm Au

Table 2-1. Design parameters for the plasmonic metallic gratings.

2.3.4. Device Fabrication Processes

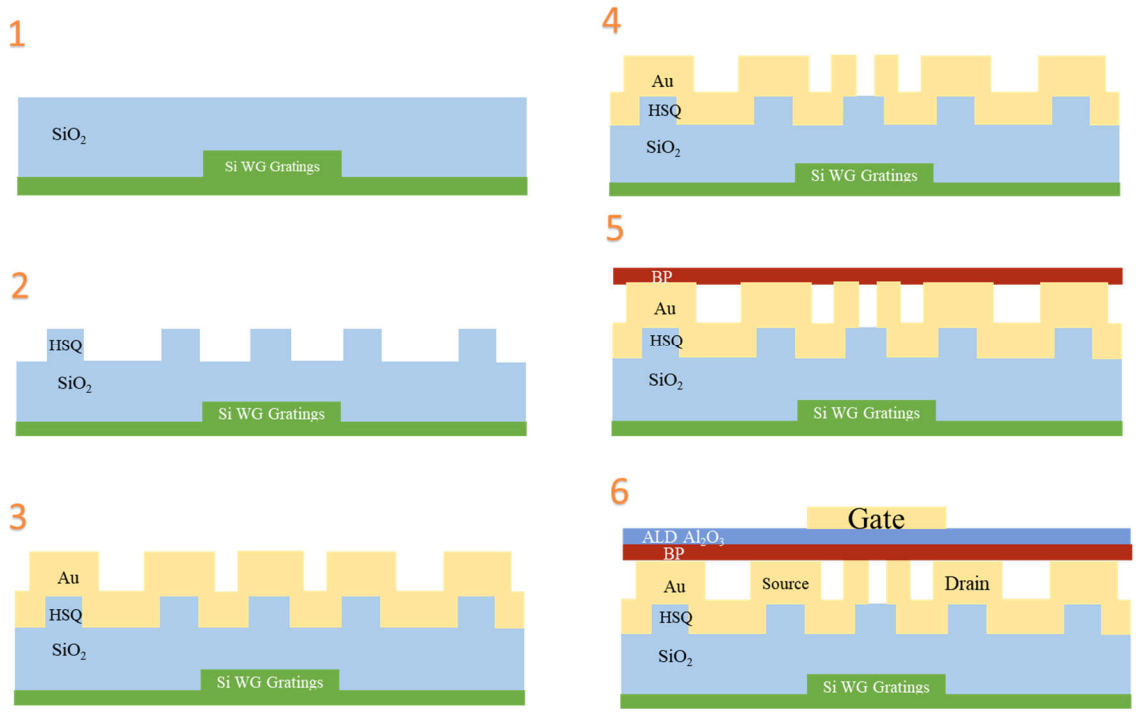

Figure 2.6. Device fabrication processes.

Due to the complexity of the device in this project, here, we present the fabrication process of the device as in Figure 2.6. Photonic structures were fabricated on a standard SOI wafer (SOITEC, 220 nm top silicon layer and 3 μm buried oxide layer). The silicon photonic layer was fabricated using standard e-beam lithography (Vistec EBPG 5000+) with ZEP resist and Bosch dry etching process (Deep Trench Etcher, SLR-770). Then, the substrate is planarized by self-aligned e-beam silicon oxide deposition (Varian 3118) without removing e-beam resist. After lift-off process in N-methylpyrrolidone (NMP) on 80 ℃ hotplate overnight, the device is cladded with a 2 μm silicon dioxide layer deposited by plasma-enhanced chemical vapor deposition (PECVD, Plasmatherm 340). The result is in the step 1 in Figure 2.6.

Next, the device is spun with a layer of hydrogen silsesquioxane (HSQ, 6% concentration) resist and baked on hotplate. The resulting thickness of HSQ is around 120 nm. The plasmonic nanostructure was fabricated with e-beam lithography by patterning the dielectric nanograting in HSQ layer (step 2 in Figure 2.6). Then using planetary fixture in e-beam deposition tool (CHA Evaporator, SEC 600), a conformal metal layer (3 nm Ti/ 120 nm Au) is deposited on top of the chip (step 3). E-beam lithography and ion milling (Intlvac Nanoquest) process is done to pattern the outline of the metallic area. In step 4, using focused ion beam (FIB, FEI Quanta 200 3D), a nanogap was subsequently milled in the noble metal film. A quick electrical characterization is done by measuring the resistance between two sides of the nanogap. Only those devices with very high resistance (i.e. good electrical insulation) were used in the following transferring process.

The BP flakes were exfoliated onto premade polydimethylsiloxane (PDMS)/glass slides stamps from bulk crystals (Smart Elements GmbH) and examined under optical microscope. The flake of appropriate thickness was transferred onto the plasmonic structure using the dry transfer method forming direct contacts with metallic gratings (step 5). To minimize the degradation of BP flake in room environment, immediately after the transfer, 40 nm Al_2O_3 was deposited by atomic layer deposition (ALD, Savannah system, Cambridge Nano Tech) at 180 ºC. This layer encapsulated the BP to prevent degradation and functioned as the gate dielectric and is widely used in 2D material devices. [91] We bake the device under vacuum at 120 C overnight to further remove any trapped water molecules. Finally, the top metal gate (3 nm Ti/100 nm Au) was patterned using standard e-beam lithography and metal deposition/lift-off (step 6).

2.4. Characterization and Measurement Result

2.4.1. Plasmonic Simulations and Device Images

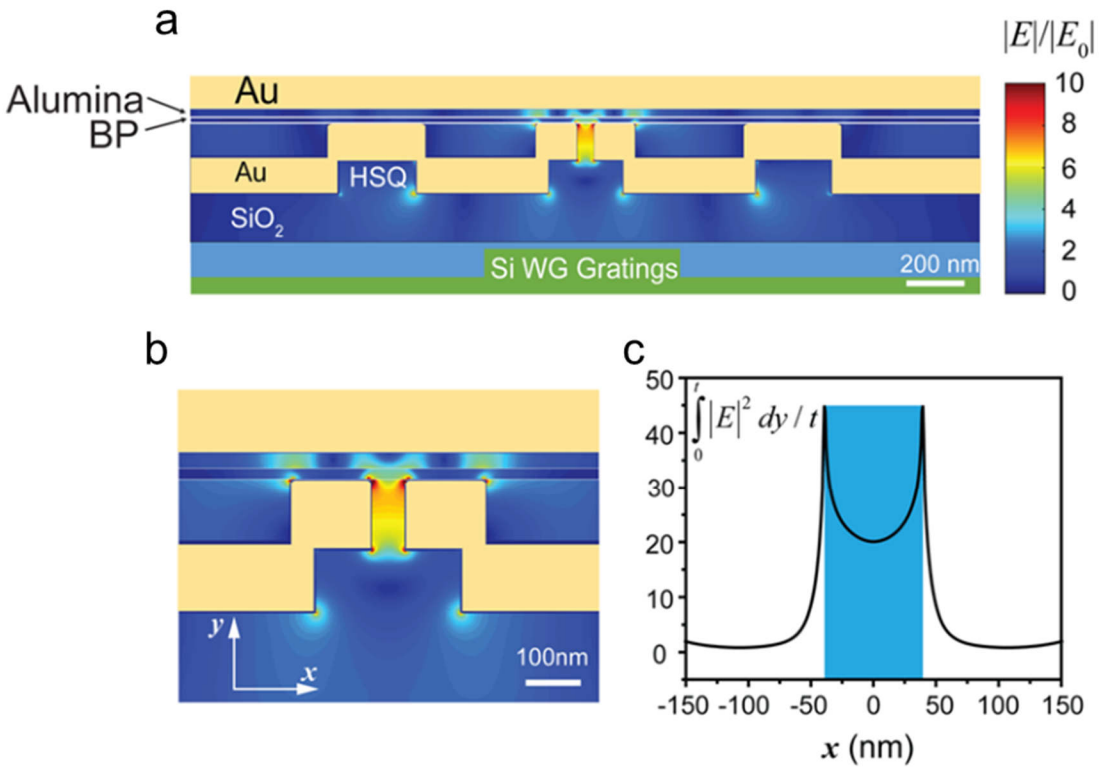

Figure 2.7. 2D FDTD simulation result of the device. (a) FDTD simulation of the optical mode coupling between the waveguide grating, metal grating, and the nanogap. $|E_0|$ refers to the source amplitude in simulation. The BP layer is outlined with the white box. (b)(c) The simulation result highlights the significantly enhanced field amplitude distribution (b) and average optical intensity in the BP layer (c) over the BP-nanogap region of the device.

First, the plasmonic enhancement effect is examined through finite-difference time-domain (FDTD) simulation. Although the direct measurement of electric field near-field intensity distribution can be achieved by near-field scanning optical microscope (NSOM),

[92] this approach is far beyond the capability of current research setup and the scope of this project. Thus, the verification and analysis of plasmonic enhancement is based on numerical simulation. Figure 2.7. (a) shows a schematic cross-sectional view of this structure, overlaid with electric field amplitude distribution (normalized to the source amplitude $|E|/|E_0|$) of the optical mode simulated by the 2D FDTD method (Lumerical FDTD solutions). As visible in the field map, the extraordinary optical transmission (EOT) effect through the nanogap generates a highly concentrated optical field in the BP layer. [93], [94] A detailed simulation highlights the enhanced electric field amplitude inside the nanogap (Figure 2.7(b)) and the profile of the averaged optical intensity in the BP layer (Figure 2.7(c)), which exhibits an enhancement factor in the range of 20-45 relative to output intensity of waveguide grating (light source in simulation).

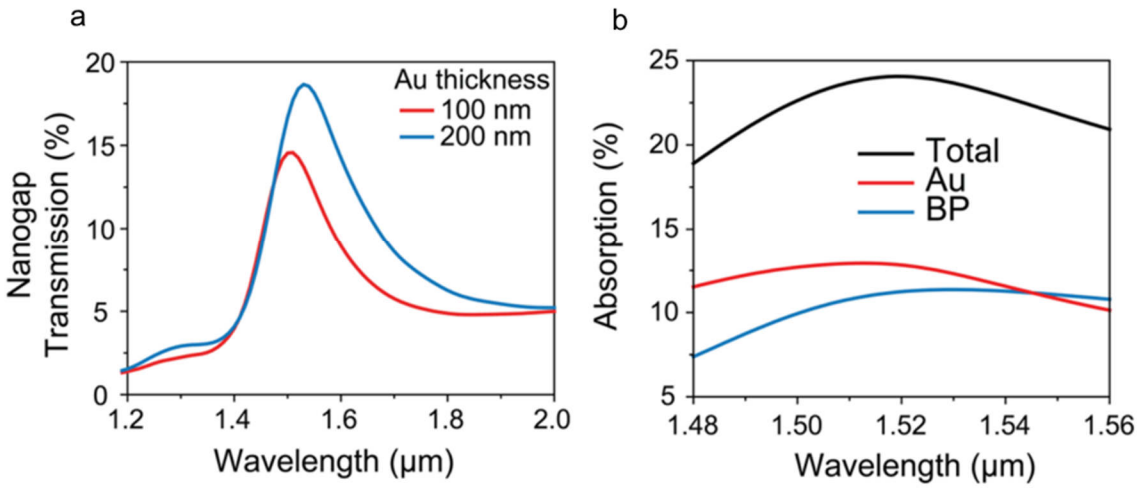

Figure 2.8. Simulated nanogap transmission and material absorption. (a) Simulated transmission spectrum of the nanogap for 100 and 200 nm Au layer thickness, showing a resonance near the designed wavelength of 1.55 μm. (b) The total absorption of the waveguide grating emission by the BP-nanogap structure found in FDTD with contributions from the BP (blue) and the metal (red).

To show the enhancement in optical transmission, Figure 2.8 (a) plots the simulated transmission spectrum of the plasmonics nanostructure with a gap width of 60 nm. The simulation result indicates that when 100 nm (200 nm) thick gold layer is used in plasmonic gratings, 15% (18%) of the waveguide grating emission can be transmitted through the nanogap at the peak, corresponding to an EOT factor of 3.75 (4.50). Figure 2.8 (b) plots the total optical absorption spectrum of the nanogap-BP hybrid and the respective contribution by the gold and the BP found in simulation. Although metal contributes more absorption (13% at peak wavelength) than BP flake, the light absorbed by BP is near 11% at peak (normalized to the power emitted from the waveguide gratings), which is significant given that the width of our aperture (60 nm) is much smaller as compared to other previously reported results. [38], [71]

The most unique part of our device design is that the two sides of the metallic nanogap also serve as the electrical source and drain contacts to the BP flake. Together with a metallic top gate, the nanogap and BP form a field effect transistor (FET) with an ultrashort channel of the width of the nanogap. Additionally, the metallic top gate reflects the transmitted light back to the BP to improve optical absorption further, which is confirmed through simulation (compare to Figure 2.4 (b)). The combined benefits of low loss light delivery using a silicon waveguide, the concentration of light using plasmonics, and the ultrashort BP channel create an integrated BP photodetector with both high detection efficiency and speed.

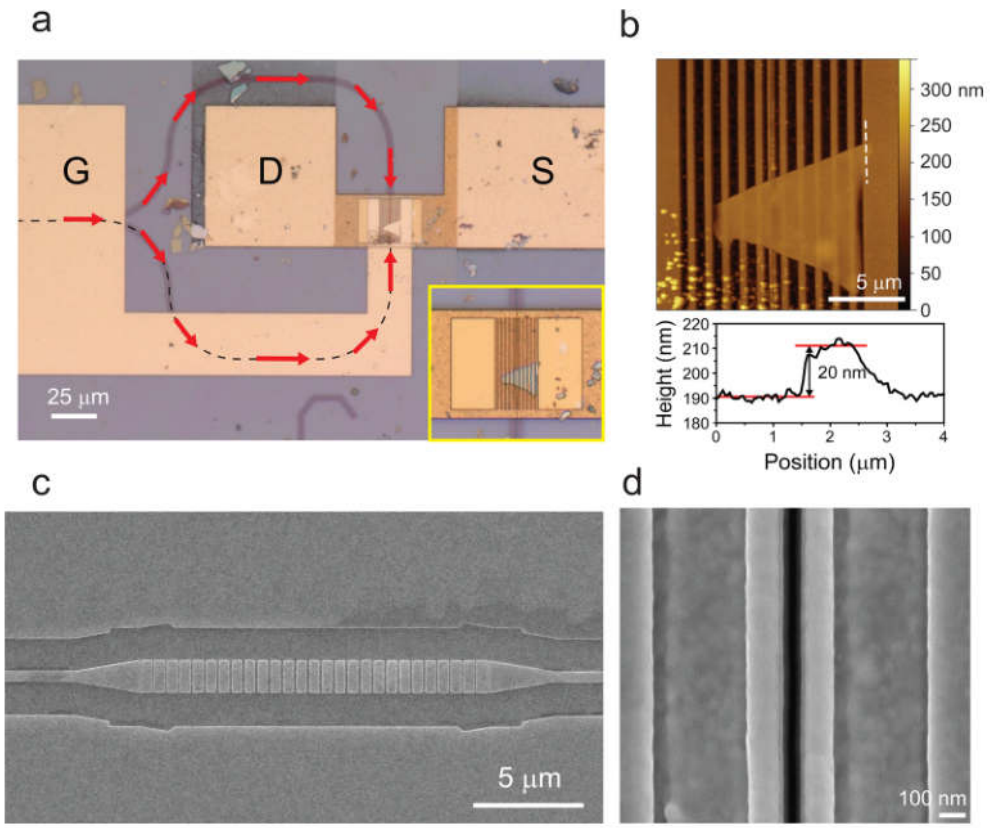

Figure 2.9. Microscope images of the device. (a) Optical microscope image of the completed device. The BP FET, using the metallic nanogap as the source and drain contacts, is integrated on top of the silicon waveguides (marked with black dashed lines). The red arrows indicate the direction of optical propagation. Inset: zoom-in microscope image of the BP–nanogap region (before patterning gate metal). (b) Atomic force microscope (AFM) image of the BP–nanogap region. The topographic profile (lower panel) along the dashed line shows that the BP flake is 20 nm thick. (c,d) Scanning electron microscope (SEM) images of the silicon waveguide grating (c) and the details of the nanogap (d), which shows a smooth and uniform gap with a width of 60 nm.

The device fabrication process is described in detail in the previous section. Device images are taken at different steps of the fabrication process. Figure 2.9 (a) shows an optical microscope image of the fabricated device. Thin BP flakes were exfoliated from

crystals and transferred to the prefabricated substrates using a dry transfer method. [30] Figure 2.9 (b) shows the atomic force microscope (AFM) image of the BP-nanogap region after Al_2O_3 encapsulation and before the integration of the top metal gate. It shows that the BP flake, 20 nm thick and 10 μm wide across the nanogap, has been successfully transferred and integrated with the plasmonic nanostructures. The scanning electron microscope (SEM) image in Figure 2.9 (d) shows that the nanogap has a very smooth profile with a width of 60 nm, which was limited by the resolution of the focused ion beam (FIB) system available in our clean room. The SEM image of the silicon waveguide grating with a period of 590 nm and duty cycle of 78 % is shown in Figure 2.9 (d).

2.4.2. Measurement Setup

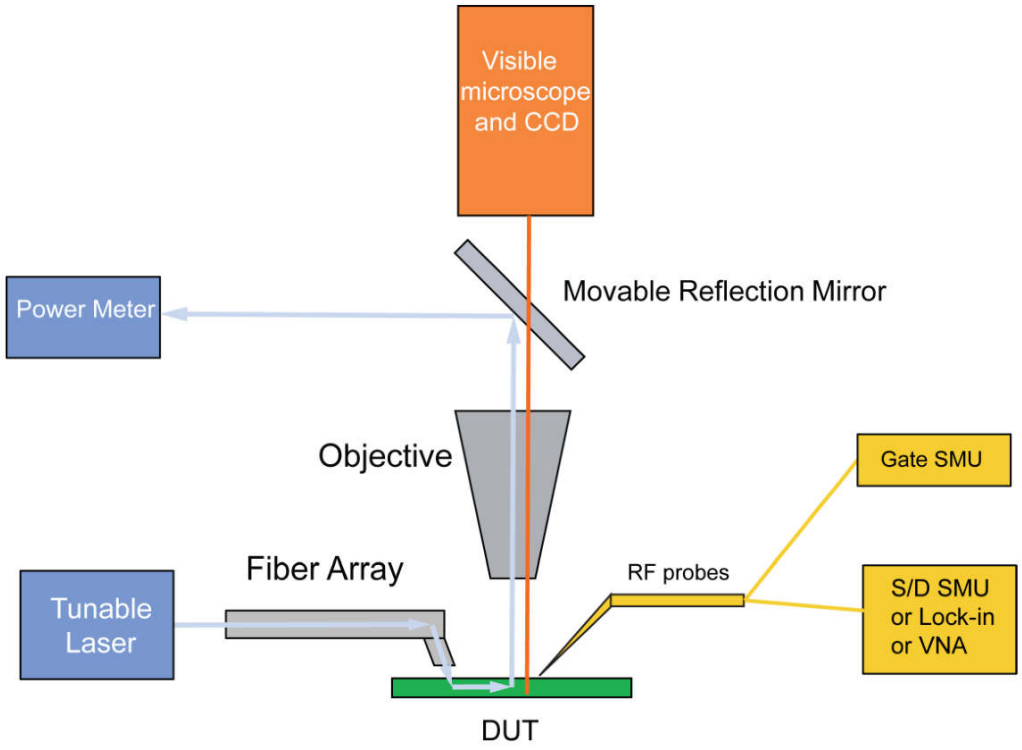

Figure 2.10. Measurement setup. Not all components and connections are shown in the illustration.

In order to measure optical and electrical performance of the device, we use a measurement setup as shown in Figure 2.10. To characterize emission efficiency of the silicon waveguide grating, the output of a tunable telecom-band laser is coupled into the waveguide via a customized fiber array and on-chip grating coupler. The light is guided to the waveguide grating and emitted vertically into free space which is collected by an infrared-transparent objective lens. When the removable reflection mirror (1550 nm band) is in the optical path, the collected light is reflected to an optical power meter. Without the presence of the movable mirror, a visible microscope and CCD camera are used to locate and align the device. In the electrical measurement part, the device has three metal contacts

(source, drain and gate) which are connected to electrical equipment through high-speed RF probes. A gate source meter unit (SMU) is used to apply appropriate gate bias voltage during the entire measurement. For DC measurements, another SMU is connected to S/D contacts to measure current. DC photocurrent measurements were performed by scanning both gate and S/D (source/drain) biases at a fixed laser wavelength, and measuring S/D currents. Two Keithley 2400 series SMUs were used in electrical measurements. Both SMUs were operated in source-voltage/measure-current mode. While one SMU applied the gate bias, the other applied the S/D bias and recorded current readings. By varying the optical power, the S/D current was measured, including the dark current. After extracting the dark current, the photocurrent was acquired for different optical power inputs at various bias conditions.

In low frequency RF measurements, a low-noise amplifier (Stanford Research Systems SR570) applies S/D bias and amplifies the current, and a lock-in amplifier (Stanford Research Systems SR830) is used to measure S/D current. In high RF frequency measurements, a vector network analyzer (VNA, Agilent 4396B) is used to measure the photoresponse for frequencies greater than 100 kHz. During RF frequency measurements, the laser light is modulated by an in-fiber electro-optical modulator (EOM, Lucent 2623NA) which is driven by a RF signal generator or the output of VNA.

2.4.3. Electrical Measurement of the BP FET

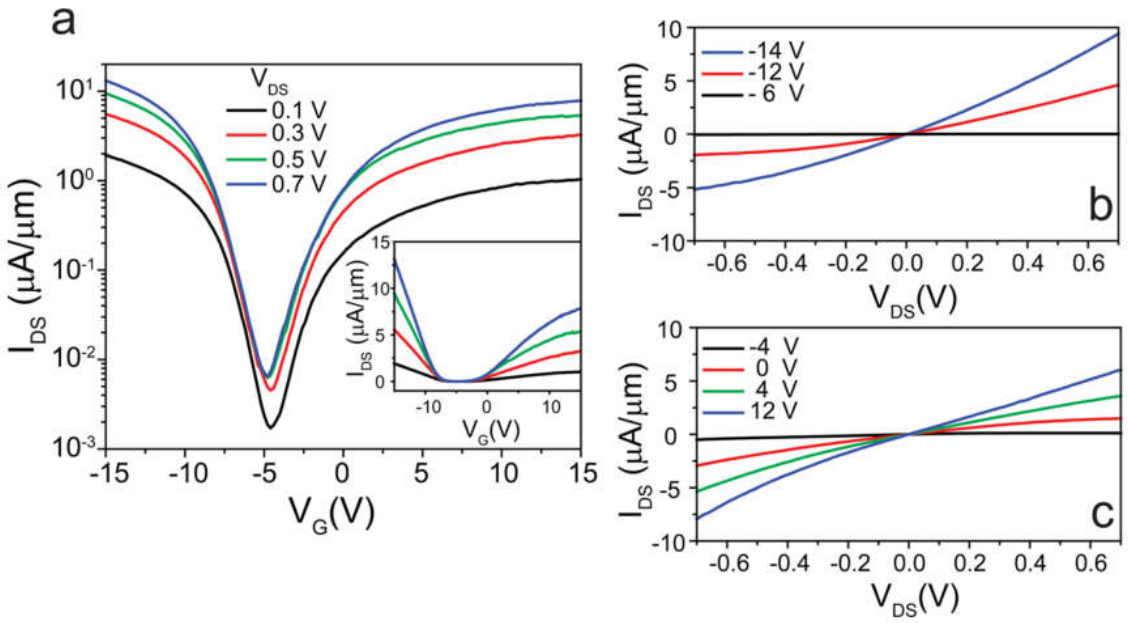

Figure 2.11. DC electrical characterization of the BP FET. (a) Source-drain current, I_{DS}, plotted in log (main panel) and linear scales (inset), as the gate voltage V_G is swept while the bias voltage is fixed at various values. (b,c) *I-V* characteristics of the device when the BP is gated to be p-doped (b) and n-doped (c), respectively.

After the completion of the device, it is important to characterize the electrical performance of the device. The electrical characteristics of the device are shown in Figure 2.11. Figure 2.11 (a) plots the source-drain current I_{DS} versus the gate voltage V_G. The short-channel FET shows outstanding gate modulation of the channel current. Even at a moderately high bias (V_{DS}) of 0.7 V, the on-off ratio is up to 10^3, and the modulation depth is comparable to reported BP FETs with similar channel length. [95] Also, the device shows excellent ambipolar transport with channel conductance in the n-doped region being only a factor of 2 lower than the p-doped region in the measured range of V_G. The BP

channel is tuned to be near intrinsic at a gate voltage of -4 V, indicating the material is n-doped. In Figure 2.11 (b)(c), the *I-V* characteristics in different doping regimes are shown. In both p-type and n-type doping regions, the FET has linear *I-V* characteristics, which implies comparable Schottky barrier heights for both holes and electrons. The slight asymmetry in *I-V* curves at positive and negative bias can be attributed to bias modulating the barrier heights: in p-type doped regime (negative gate bias), positive V_{DS} can further narrow the Schottky barrier width and increase the contact conductance; on the contrary, in the n-type doped regime negative V_{DS} can narrow contact barrier and increase the conductance. [96]

2.4.4. Photodetection Characterization and RF Response Measurement

Before showing the photodetection performance of the device, it is necessary to reiterate how the light is routed to the BP photodetector in the hybrid system. First, laser light is coupled from a fiber array into the waveguide through grating couplers with a typical coupling efficiency of ~20%. The optical signal propagates to the waveguide grating and reemits upward. The waveguide grating (Figure 2.9 (c)) is designed to have an efficiency of 48%, using adiabatically tapered duty cycles to mitigate back reflection. However, the measured efficiency is only 14%, which is attributed to fabrication imprecision and nonideality. This efficiency can be further improved by about a factor of 2 with the use of a back reflector. [97] With the assistance of the metal gratings on both sides of the nanogap, the emitted light excites SPP waves on the metallic nanostructure, which further propagates and funnels through the nanogap, leading to the EOT effect and significantly increased absorption in the BP layer (Figure 2.8 (b)).

The device's photoresponse was measured when it operates in the photoconductive mode with an applied source-drain bias. Figure 2.12 (a) shows the source-drain current I_{DS} at a fixed V_G of -8 V at different optical power levels, marked in the legends as the power emitted by the waveguide grating. It is clearly seen that photocurrent is generated in the BP channel with a magnitude that increases with the optical power. The photocurrent of the device is also highly dependent on the gate voltage, as shown in Figure 2.12 (b). The maximum photocurrent occurs near a gate bias of -8 V, coincident with the peak of the FET transconductance g_m, as shown in the lower panel of Figure 2.12 (b), indicating an internal gain mechanism plays a role. Figure 2.12 (c) shows a 2D contour plot of the photocurrent dependent on the gate and bias voltage. It is clear that the device shows very

low negative photocurrent in the highly doped regions. Unlike the long channel devices, [38], [39] the bolometric effect has a rather negligible contribution to the measured photocurrent. We attribute this to the large metal area in our device, which provides an efficient heat sink for the BP channel to dissipate heat quickly.

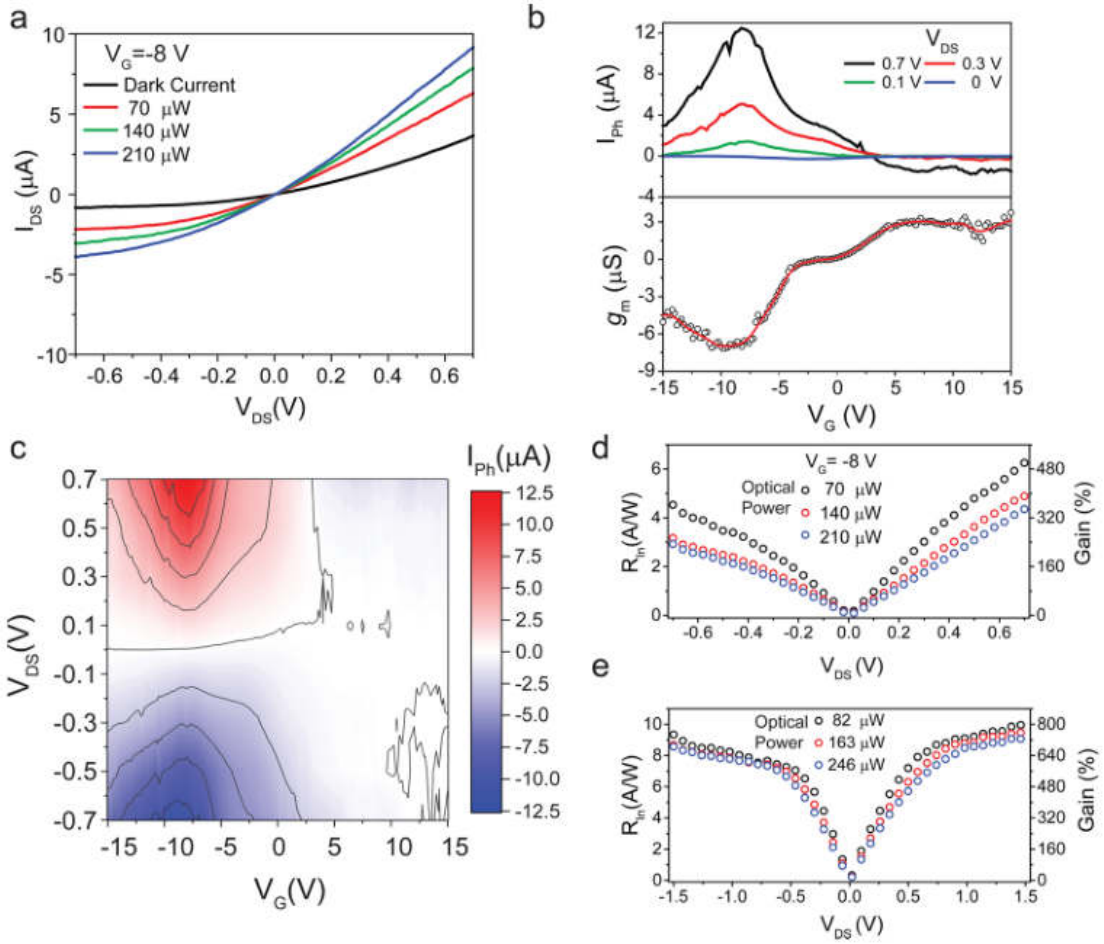

Figure 2.12. Photoresponse of the BP photodetector. (a) Source-drain current I_{DS} of the BP FET at a fixed gate voltage V_G (-8 V) versus source-drain bias V_{DS} under varying optical power levels. The optical power levels refer to the emission at the silicon waveguide grating, determined by the calibration. (b) Photocurrent I_{ph} and transconductance (g_m) at optical power level of 560 μW when the gate voltage is swept. The maximums of I_{ph} and g_m are coincident at the same gate voltage, suggesting the related gain mechanism. (c) Contour plot of photocurrent I_{ph} versus V_G and V_{DS}.

Bolometric effect that generates negative photocurrent is weak in the device. (d) The intrinsic responsivity, referred to the absorbed optical power in BP, is as high as 6.25 A/W, corresponding to a photoconductive gain of 500%. (e) In another device without an integrated top gate, the highest responsivity is 10 A/W at 1.5 V source-drain bias and the corresponding photoconductive gain is 800%.

On the basis of the measurement results of photocurrent I_{ph}, the intrinsic responsivity $R_{In} = I_{ph}/P_{abs}$, where P_{abs} is the absorbed optical power by the BP, and the photoconductive gain factor defined as $G = R_{In}/(\eta e/h\nu)$, where $h\nu$ is photon energy, e is electron charge, and η is intrinsic quantum efficiency, are calculated and plotted in Figure 2.12(d) for different optical powers. P_{abs} is calculated based on the waveguide grating calibration and the simulation results in Fig. 2.8. For example, when the estimated optical emission power from the BP covered gratings (BP covers 18% of the total grating area) is at 12.6 μW, the external responsivity of the photodetector is 214 mA/W. Simulation (Figure 2.8 (b)) suggests that the 20 nm BP layer absorbs 11% of the optical power emitted from the waveguide grating, and among this 31% is absorbed in the active BP area within the 60-nm wide channel, which generates the collected photocurrent. Therefore, the device achieves a remarkable intrinsic responsivity R_{In} of 6.25 A/W and a gain G of 500% at V_{DS} = 0.7 V. Figure 2.12 (e) shows the results of another device fabricated without the top gate, allowing application of higher bias without the concern of the large drain-gate field that may breakdown the BP. Its R_{In} is as high as 10 A/W at a bias voltage of 1.5 V. These values of responsivity are considerably higher than many previously reported results.[38], [89] Also noticeable is that the responsivity reduces slightly with increasing optical power, which was previously observed in MoS_2 photodetection measurements. [98] This slight

decrease may be attributed to increased photocarrier recombination with increasing incident photons that generate high concentration of excess carriers in the material, especially when considering the very high optical intensity in the nanogap. We note that this saturation effect occurs at μW level of optical power, significantly higher than that used in the devices reported previously. [71], [99], [100]

The larger than unity gain factor G indicates there are internal photocurrent gain mechanisms at play. Given the symmetric design of the device, the contribution of the photothermoelectric effect can be excluded. The field effect mobility μ_{FE} can be extracted from the transport results by using $\mu_{FE} = g_m L/(WC_{ox}V_{DS})$, [66] where g_m is the trans-conductance, L = 60 nm is the gate length, W = 4.5 μm (see Figure 2.9 (b)) is the channel width, and C ox is the gate oxide capacitance per unit area. The hole mobility is estimated to be 0.96 $cm^2 V^{-1} s^{-1}$ in the linear regime (Figure 2 .11(a) inset). The extracted mobility is likely to be much underestimated due to the high contact resistance in our device, and consequently much lower than previously reported results. [24], [101] We attribute the high contact resistance to directly transferring the BP flake onto the metal contacts. This process likely causes trapping of a high level of contaminates at the interface, as compared to forming the contacts by directly depositing metal onto the BP. Using the extracted field mobility value, the carrier transit time in the BP channel can be calculated with $\tau_{tr} = L^2/(\mu_h V_{DS})$ to be 53.6 ps, whereas the carriers in bulk and at the surface of BP can be trapped with a longer lifetime. The coincidence of the maximum of the photocurrent and the maximum of g_m at the same gate voltage (Figure 2.12. (b)) indicates that photogating effect related to charge trapping and the short transit time lead to a high

photoconductive gain (*G*) in our device. [102] In the photogating effect, one type of carrier is effectively trapped (by trap states or band bending) while the other type travels multiple time before they recombine. Moreover, the much higher hole mobility than the electron mobility in BP also facilitates the photoconductive gain. [103] The photoconductive gain (Figure 2.12. (d)) of our device originates from the short BP channel length of only 60 nm enabled by the integration with the nanogap, and can be significantly increased if the carrier mobility can be improved and the contact resistance lowered.

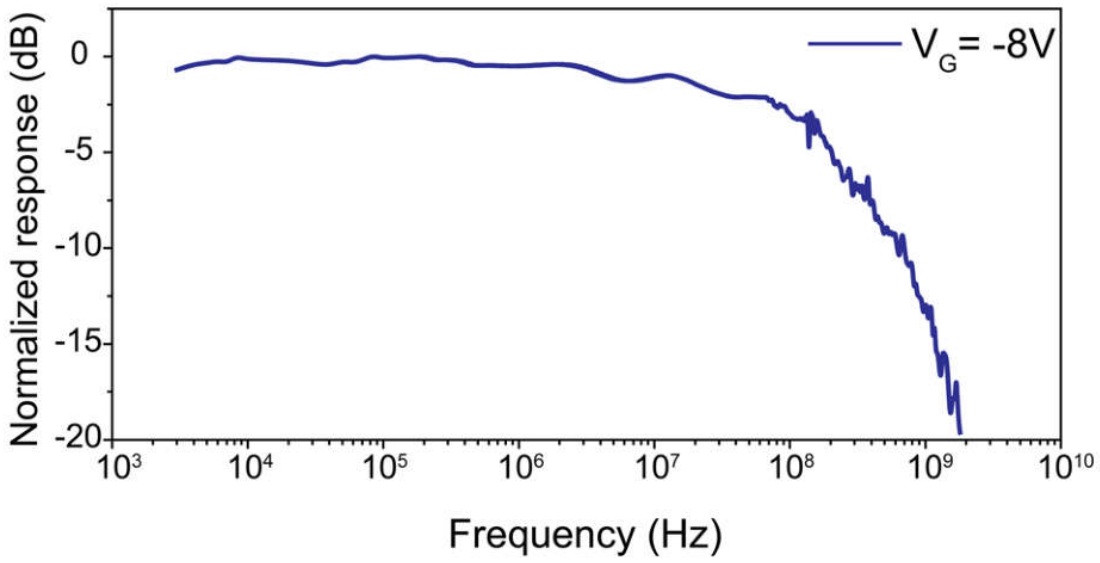

Figure 2.13. Frequency response of the BP photodetector to amplitude-modulated optical signal. The 3-dB cutoff frequency is at 150 MHz, limited by the RC bandwidth of the device. The contact resistance of the device is the main factor that limits the high-speed performance of the device.

It has been reported that the photogating effect in 2D materials due to photocarriers in mid-band traps states can dramatically enhance the optical responsivity, however, only at low frequency due to the very long trapping time. [71], [99], [100] We assessed the frequency response of the photodetector to an amplitude-modulated optical signal in the

frequency range from 2 kHz to 1.8 GHz, as shown in Figure 2.13. A lock-in amplifier was used from 2 to 100 kHz range and an RF network analyzer was used from 100 kHz to 1.8 GHz in the measurement. The photoresponse of the device shows a 3-dB roll-off frequency of 150 MHz. Although this cutoff frequency response is lower than that of previously demonstrated BP photodetectors, [38] it is considerably higher than that of devices dominated by the photogating effect and other reported results.[71], [89], [104], [105] The current device's frequency response is limited by the RC time constant, because although the parasitic capacitance of the device is measured to be ~260 fF at 1 GHz, the contact and channel resistance is very high. [68] Compared to our previous result, [38] although the current device achieves very high responsivity due to a very short channel, the frequency response is compromised by the high resistance. In the future, improving the contact to BP could be achieved by transferring BP flake in an ultraclean and inert environment to avoid contaminations and using different adhesion metal layer between BP and Au to lower Schottky barrier. [106] Additionally, sandwiching BP between two layers of hexagonal boron nitride (h-BN) can not only improve the carrier mobility in BP [107] but also allows fabrication of 1D edge contacts to BP to further reduce contact resistance.[108]

2.4.5. Additional Measurement of the Device without Top Gate

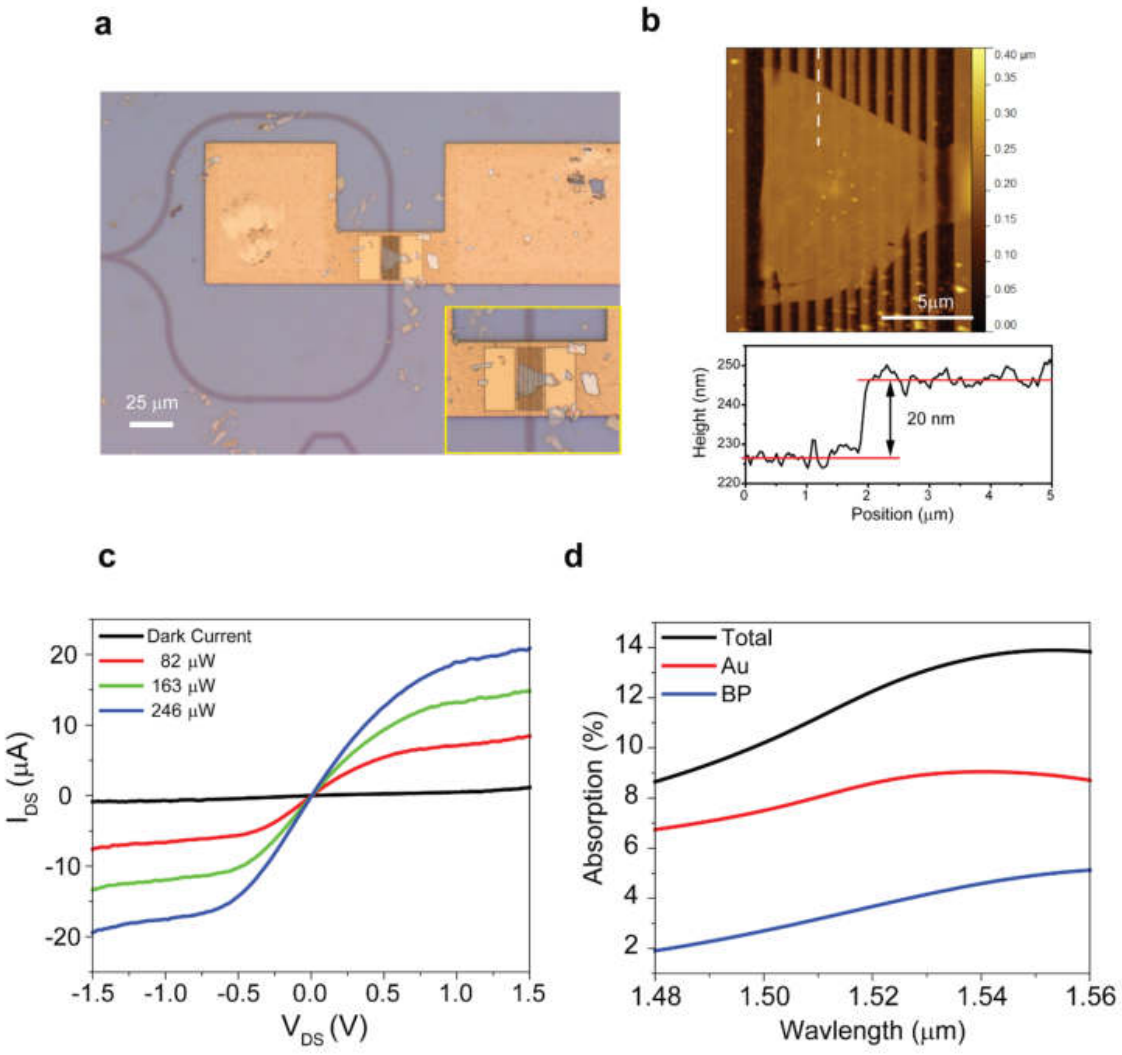

Figure 2.14. Similar BP photodetector without top gate. (a) Microscope image of the fabricated device. Inset: zoom-in image of BP on nanogap. (b) AFM image of the BP flake on metallic grating. Lower panel: height profile of the flake along white dashed line indicating 20 nm thickness of BP. (c) I_{DS}-V_{DS} curves under different input optical powers. The marked optical power levels refer to the emission power at the waveguide grating, determined by our transmission measurement. (d) Simulated absorption of Au and BP in the device without top metal gate. The absorption is normalized to optical emission of waveguide grating.

Here we show another fabricated device without a top metal gate to provide supplementary information. The intrinsic responsivity of this ungated device is shown in Figure 2.12 (e). As shown in Figure 2.14 (a), the overall structure is the same as the gated device discussed in previous section. The AFM image (Figure 2.14 (b)) indicates the BP flake has a length of 10 μm and thickness of 20 nm. I_{DS}-V_{DS} measurement results are shown in Figure 2.14 (c) with various optical powers. Without optical illumination, the device has very small dark current. When input optical power increases, S/D current increases indicating the presence of photocurrent. I_{DS} is symmetric for positive and negative V_{DS}, which is different from the device with top metal gate (Figure 2.12 (a)). Figure 2.14 (d) is the simulated absorption in different materials for this device (normalized to waveguide grating emission). Comparing to the 11% absorption in BP (Figure 2.8 (b)) for a device with gate reflection, the absorption here is only 5% due to the absence of reflection from metal gate.

2.5. Conclusion

In conclusion, we have shown an integrated BP infrared photodetector based on a 3D integration platform of silicon photonics and plasmonics. The photodetector's performance significantly benefits from silicon photonics' ability to deliver light over a long distance with very low propagation loss and plasmonics' ability to concentrate light to the sub-diffraction limit. Direct integration of BP on the plasmonic nanogap also naturally makes a short channel photodetector, enabling built-in photoconductive gain with a high detection bandwidth. Much higher photoconductive gain can be obtained when the nanogap width is further reduced to below 10 nm as has been achieved recently,[109] and the BP quality is improved to increase carrier mobility such that the carrier transport in the device may approach the ballistic regime. The optical loss at the waveguide grating and the plasmonic grating can be reduced by improving the waveguide grating design, adding a dielectric reflector under the waveguide grating, and more systematic optimization between the photonics and plasmonics layers. The results from the current device successfully demonstrate the feasibility and promise of such a hybrid approach of integrating 2D materials, plasmonics, and silicon photonics. Overall, this integration approach combines the best attributes of each technology while mitigates their respective disadvantages. Our demonstration of a photodetector with high responsivity and fast frequency response is only the first step. The integration approach can be adopted to make efficient optical modulators, [110] nonlinear optical devices, [111] and co-integration of 2D electronics with optoelectronics [112] with a broad range of potential applications including optical signal processing. [113]

Chapter 3. Plasmonic Antenna Integrated on Waveguide for SEIRA application

3.1. Project Motivation

With the advancement of nanotechnology, electromagnetic waves can be confined below the diffraction limit in nanoscale metallic structures and thus light-matter interactions is dramatically enhanced by harnessing surface plasmons. Optical sensing technologies advance rapidly, facilitated by the sub-wavelength field localization and resonant field enhancement rendered by nanoplasmonic devices. [76], [114] These include surface-enhanced Raman scattering (SERS),[115]–[117] and surface-enhanced infrared absorption (SEIRA).[49], [53], [54], [118]–[124] Among these methods, SEIRA directly measures absorption peaks related to molecular bond vibrations in the infrared band and is capable of detecting and identifying a minute amount of analyte. It is highly desirable to implement SEIRA as a portable, fully-integrated system in a miniaturized form-factor for applications including industrial chemical sensing and biomedical diagnosis,. Nowadays, SEIRA sensing is typically performed with a bulky table-top setup consisting of a Fourier Transform Infra-Red (FTIR) spectrometer coupled with a microscope. Such systems are not amenable to chip-scale miniaturization. Another limitation of performing SEIRA with a conventional FTIR system is its use of a low-brilliance thermal IR source (i.e. a Globar source), which also has low power efficiency. The low intensity of the source requires a large number of plasmonic sensing elements (e.g. nanorods, bowtie antennas) and a long

integration time to overcome background noise for sensing application, thus limiting both the chip size and the signal acquisition speed.

Comparing to the thermal sources, coherent IR sources such as quantum cascade lasers (QCL) and optical parametric oscillators (OPO) can generate output beams with much higher brilliance over a widely tunable spectral range.[50], [125] Since chip-scale QCL,[126] OPO,[127] and mid-IR frequency combs[128] have become available in recent years, these coherent sources show great promise for SEIRA applications. Aside from the IR source, another major challenge in SEIRA is the low coupling efficiency from the light source to nanoplasmonic resonators because of the mismatch between the diffraction-limited optical spot size and the deep-subwavelength plasmonic mode size in the nanostructures. For instance, most SEIRA measurement setups use a reflective (i.e. Schwarzschild) objective lens to focus IR light to a typical spot size of tens of micrometers,[50] which is much larger than the dimension of typical plasmonic sensors.

Fully integrated on-chip SEIRA systems can leverage the tremendous development of integrated photonics, which can be manufactured using CMOS fabrication technology. Silicon waveguides can deliver light on-chip with very low propagation loss over a broad IR spectral range.[129]–[133] Placing photonic devices of different materials in the vicinity of a silicon waveguide enables efficient coupling with the evanescent field of the waveguide mode and thus heterogeneous integration to achieve new functionalities with impressive performances.[36], [38], [40] Integration of nanoplasmonics and silicon photonics has been conceived by many to combine plasmonics' strong field enhancement with silicon waveguide's optical mode confinement and low propagation loss. So far, there

have been many successes in attempting such a hybrid approach in optical modulation,[134], [135] photodetection,[80], [136] mode conversion,[57], [88] sensing,[60], [137] and heat-assisted magnetic recording (HAMR).[138] In addition, the efficient coupling between plasmonic structures and silicon waveguides has been achieved for individual nanotapers[58] and long nanoparticle chains.[139] Specifically, for sensing applications, bowtie nanoantennas have been integrated on silicon nitride waveguides to realize on-chip SERS.[60] However, few hybrid waveguide-plasmonic devices have been demonstrated in the mid-IR range, though a hybrid waveguide mode converter has been reported recently by Nanfang's group.[57]

3.2. Fiber End-Coupling Measurement Setup

Although planar grating coupler can couple light efficiently with optimized design and requires fewer fabrication steps, its bandwidth is still too narrow for broadband spectroscopy research. [97] Moreover, the most commonly used fibers in mid-IR range are hollow fibers [140] and chalcogenide glass fibers, [141] which are extremely brittle and requires large bending radius. Manufacturing a compact fiber array assembly becomes difficult and unpractical, comparing to telecom fibers. In order to efficiently couple light into silicon waveguide over a broadband IR wavelength (2.5- 3.7 μm), the end-coupling scheme is applied.

We design a very straightforward measurement setup for mid-IR waveguide experiment, as shown in Fig. 3.1. A commercial tunable OPO laser (M Squared, Firefly IR SW) covering the wavelength range from 2.5 to 3.7 μm is used as the coherent IR light source. Because the OPO laser output is polarized in the vertical direction (manufacturer setup), a pair of reflection mirrors in vertical periscope setup are used to rotate the polarization to horizontal direction (for waveguide TE mode coupling). A rotational neutral density filter is used to control the optical power continuously. The laser beam is modulated at 1 kHz by the mechanical optical chopper (Stanford Research System, SR540). A reflective fiber collimator focuses light into the single-mode optical fiber which then couples light into the silicon waveguide. A multi-mode fiber with a large core diameter is used to collect waveguide end output and transmit the light into a photodetector. The signal from photodetector is sent to a lock-in amplifier (SR 830) with reference frequency signal from chopper controller. This lock-in measurement setup helps reduce noise from the

environment and laser output fluctuation. Finally, the transmission spectrum of the waveguide is obtained by scanning the laser output wavelength while acquiring the output signal of the photodetector at the same time.

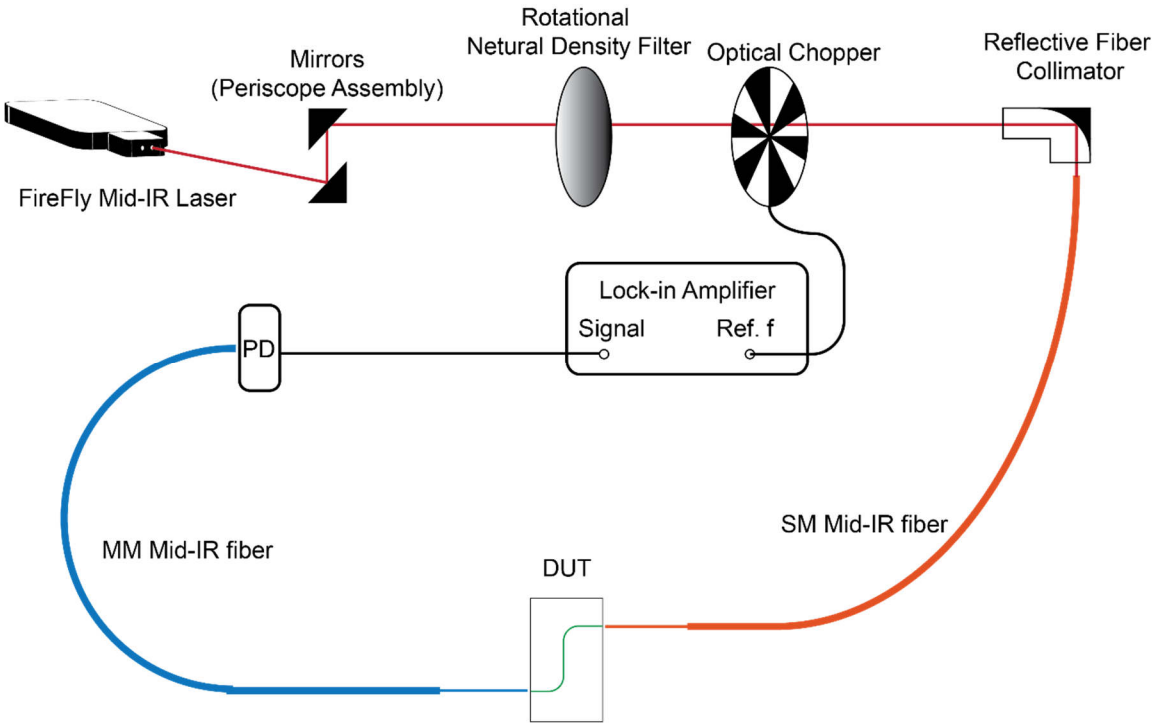

Figure 3.1. Detailed measurement setup for fiber end-coupling approach.

3.3. Narrow-Gap Devices and SEIRA Sensing

3.3.1. Device Design and Simulation

The plasmonic-waveguide hybrid device is fabricated on a silicon-on-insulator (SOI) substrate with a 600 nm thick silicon device layer and a 3 μm thick buried oxide layer. The silicon rib waveguide is patterned with electron beam lithography (EBL) (Vistec EBPG 5000+) and etched with a reactive ion etching (RIE) process. The rib waveguide is 1600 nm in width (*W*), 400 nm in depth (*D*) and 200 nm in the thickness of the slab layer. The waveguide supports a fundamental TE mode in the measured wavelength range (Fig. 3.3(a)) and is designed to reduce mode leakage into the SiO_2 layer underneath, which has a noticeable amount of absorption in the mid-IR band. As shown in Fig. 3.3(a), the two ends of the waveguides are inversely tapered to a narrow width of 120 nm to significantly improve fiber-waveguide coupling efficiency and suppress detrimental Fabry–Pérot noise due to waveguide facet reflections. At the middle section and directly atop the waveguide (Fig. 3.2(a) inset), five pairs of nanorods (3 nm Ti/35 nm Au) with a narrow gap of ~30 nm are patterned with standard EBL, metal deposition, and lift-off processes. Precise alignment between the silicon waveguide and the nanorods is clearly shown in the SEM image of the device (Fig. 3.2 (b) (c)).

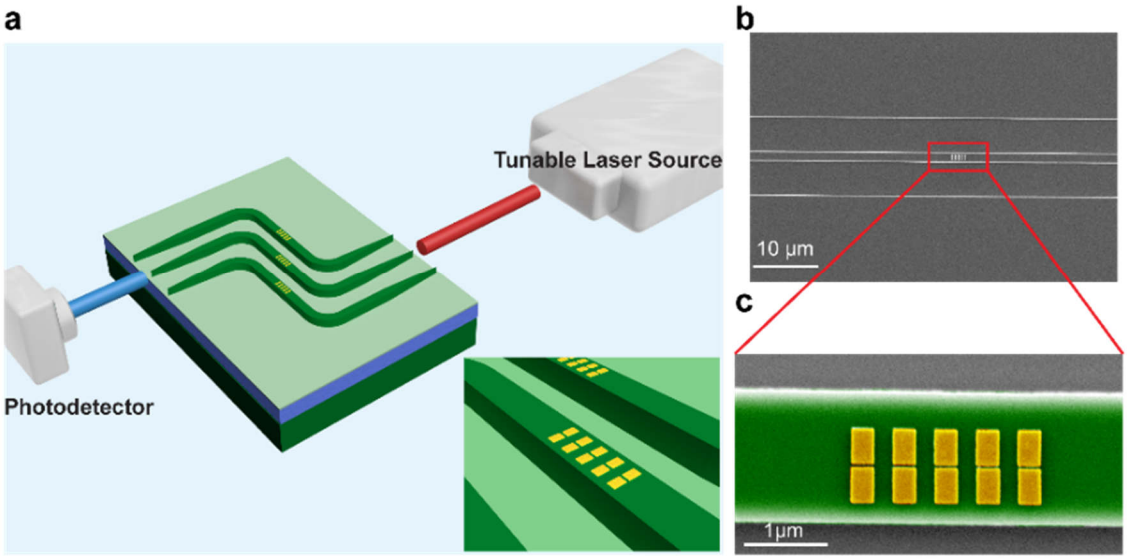

Figure 3.2. Device schematics and SEM images. (a) 3D artistic illustration of the chip and the simplified measurement setup. Chopper and lock-in amplifier used in the experiment are not shown. Inset: zoom-in view of the nanorod array integrated on the waveguide. (b) (c) Scanning electron microscope (SEM) image of the fabricated device.

Light is efficiently coupled from waveguide to the nanorod array when the laser wavelength is tuned to the nanorods resonance wavelength.[142] As a result of the plasmonic enhancement, oprical hotspot appears in the nanogaps as shown in Fig. 3.3 (b) and (c). This resonant coupling results in strong dissipation of the guided mode due to metallic absorption and radiation from the nanorods and thus a reduced waveguide transmission within the plasmonic resonance. When the wavelength is off-resonance, the propagating waveguide mode interacts with the nanorods weakly and only suffers from relatively weak broadband absorption and scattering. Because of the very small footprint of the nanorod array, the off-resonance loss is much lower than other similar devices with longer metallic structures.[57], [139] Therefore, such an integrated configuration allows

measuring the nanorods' resonance conveniently through the transmission spectrum of the waveguide, in much the same way as waveguide side-coupled dielectric resonators such as photonic crystal cavities. Compared to dielectric resonators, metallic plasmonic resonators have a much smaller footprint and mode volume, but also low Q factors (typically <10 in the mid-IR). Both types of cavities/resonators have their advantages and shortcomings and should be evaluated depending on specific application requirements.

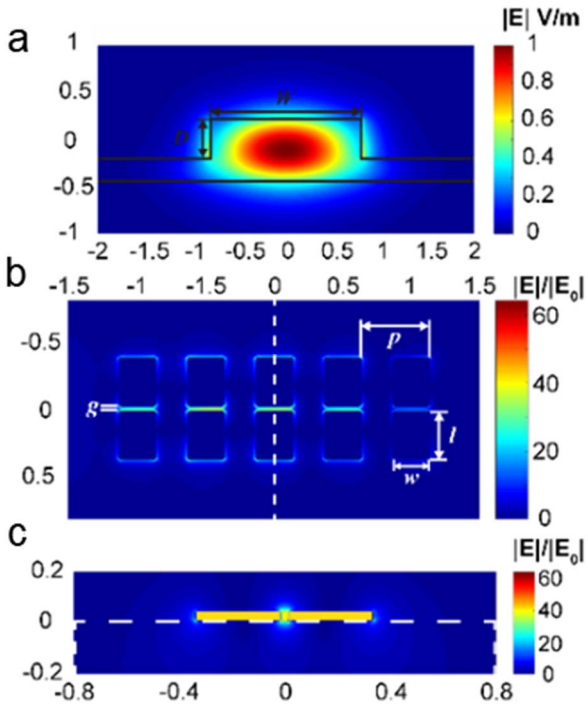

Figure 3.3. Electric field intensity distribution acquired from 3D FDTD simulation. (a) Cross-sectional view of the simulated electric field distribution of the waveguide fundamental TE mode at 3.5 μm wavelength. *D* and *W* are the rib waveguide depth and width, respectively. (b) Top-view of the normalized electric field distribution (of the plane 1 nm above waveguide top surface) at the plasmonic resonant wavelength. The parameters of the nanorods are labeled as *p*, *l*, *w* and *g*, representing the nanorods' period, length, width and gap, respectively. (c) Cross-sectional view of the device sliced at the dashed line in (b) with the normalized electric field distribution at the

resonance wavelength. The silicon waveguide is outlined with dashed line box. Note: the unit of coordinates in (a) (b) (c) is micrometer.

The nanorod array has multiple design parameters including length (l), period (p), width (w) and gap (g) as denoted in Fig. 3.3(b). These parameters collectively determine the resonant wavelength, the field enhancement factor, and the coupling strength with the silicon waveguide.[142], [143] Specifically, since SEIRA signal increases with the square of the electric field amplitude, the most critical parameter among them is the nanogap width, which determines the field enhancement factor. Considering the fabrication precision and yield, we choose a gap size of 30 nm. To maximize the field enhancement factor, more advanced fabrication processes can be applied[55], [124] to reduce the gap size to as small as 2-3 nm. The 3D finite-difference time-domain (FDTD) simulation in Fig. 3.3 (b) and (c) shows that, on resonance, the highest electric field intensity is in the nanogap between the center pair of nanorods, where the field amplitude enhancement factor is over 60 with respect to the evanescent field of the waveguide mode (1 nm above the waveguide top surface).

3.3.2. Waveguide Transmission Measurement Results

We design the resonance of the nanorod array to be within the spectral range of our laser source. Fig. 3.4(a) shows the measured transmission spectra of the devices with changing nanorod length (l). To acquire the spectrum, the laser wavelength is scanned in steps of 10 nm. A strong resonance peak can be observed in the spectrum. As the length of the nanorods increases and other parameters remain fixed, it is observed that the resonance wavelength consistently red-shifts and the extinction ratio changes non-monotonically. When l = 420 nm, the extinction ratio reaches the highest value of over 20 dB. We note that the situation is quite different from that of a plasmonic perfect absorber[144], [145] because in our devices reflection and scattering cannot be neglected. Our simulation in Fig. 3.7 (a) shows that when the resonance of the nanorod array is excited, of the total incident power in the waveguide, the nanorod arrays resonantly reflect 30% into the backward propagating waveguide mode, absorb 20 %, and scatter the rest downward into the oxide layer and upward into free-space. It is worth noting that, due to metallic damping, the wavelength at which the near-field intensity maximum is slightly red-shifted relative to the wavelength when far-field intensity is maximal[146], [147]. Thus, the maximum electric field intensity (Fig. 3.3 (b) and (c)) indeed occurs at the wavelength near 3.5 μm, red-shifted from the wavelength position of maximum extinction near 3.3 μm as measured.

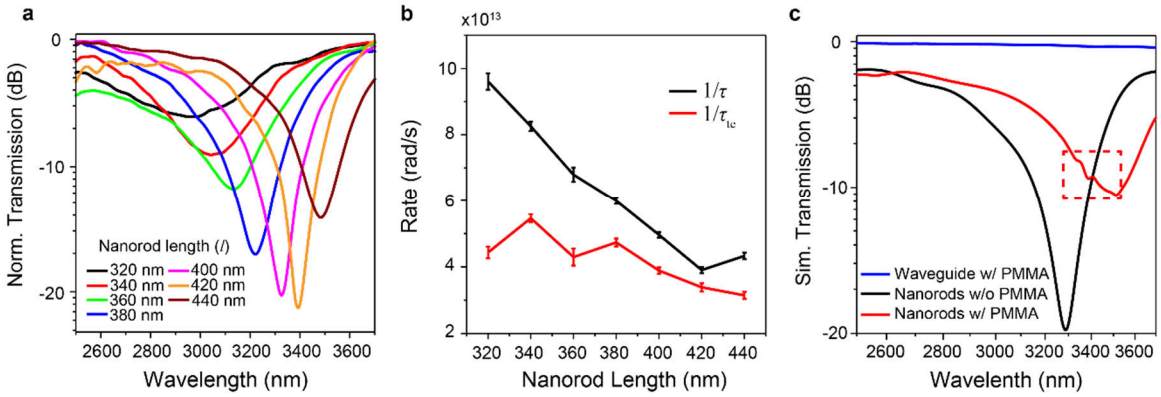

Figure 3.4. Waveguide transmission spectra, fitting parameters and simulated SEIRA sensing results. (a) Waveguide transmission spectra of devices with varying nanorod lengths. The wavelength is scanned in steps of 10 nm. (b) Coupling parameters extracted by fitting the transmission spectrum of each nanorod length. $1/\tau$ and $1/\tau_{te}$ represent total loss and total external loss of the waveguide-resonator coupled system, respectively. (c) FDTD-simulated transmission spectra of a reference waveguide-nanorod array device, the same device covered with 200 nm PMMA, and a simple bare waveguide with a rectangular PMMA patch. The absorption peaks of PMMA are clearly visible (in the dashed line box) in the hybrid waveguide-resonator device.

To fit the measured transmission spectra and understand the underlying mechanism of the change in extinction ratio, a theoretical model is derived. In devices with a long chain of metallic gold nanoparticles on top of a silicon waveguide, the chain is treated as a plasmonic waveguide to allow the use of coupled mode theory.[57], [139], [148] Our device, however, has a very short plasmonic device length and very high field enhancement, such that coupled mode theory is not appropriate. Instead, we treat our plasmonic array as a resonator[149], [150] and use temporal coupled-mode theory to model the system.[151], [152] With this approach, the transmission spectrum can be written as the following (the derivation can be found in supplementary information):

$$T = \frac{|s_{2-}|^2}{|s_{1+}|^2} = |t_0|^2 + \frac{-\frac{2\beta}{\tau_{te}}(w - w_0) + \left(\frac{1}{\tau_{te}}\right)^2 + \frac{2\alpha}{\tau\tau_{te}}}{(w - w_0)^2 + \left(\frac{1}{\tau}\right)^2} \qquad ((3\text{-}1)$$

Here s_{2-} and s_{1+} represent the outgoing amplitude from the output waveguide and incoming amplitude from the input waveguide, respectively. ω_0 is the resonance frequency of the resonator, $1/\tau_{te}$ represents the resonator's total external coupling rate to the waveguide mode, and $1/\tau$ is the total loss of the resonator and corresponds to the linewidth of the resonance. In addition, we introduce a complex, frequency-independent off-resonance transmission coefficient $t_0=\alpha + j\beta$ to account for the broadband damping (α) and the phase shift (β) caused by non-resonant interaction with the nanorods. We can extract the parameters: ω_0, τ_{te}, τ, α, β by fitting the measured transmission curves in Fig. 3.4 (a). The extracted values of $1/\tau$ and $1/\tau_{te}$ are plotted in Fig. 3.4(b) with respect to different nanorod lengths. As expected from Eq. (3-1), when the $1/\tau_{te}$ approaches $1/\tau$ for the device with l = 420 nm, the measured spectrum shows the highest extinction ratio (Fig. 3.4 (a)). Because of the complex t_0, the resonance is slightly distorted from an ideal Lorentz resonance lineshape.[153] The very high extinction ratio of greater than 20 dB achieved when l = 420 nm indicates that, other than a non-resonance loss of $1-|t_0|^2$, more than 99% of the power in the waveguide mode is coupled to the resonance mode of the nanorods. Our measurement results, as well as the simulation results in Figure 2c, show that the non-resonance loss $1-|t_0|^2$ is typically 30% so that an on-resonance, waveguide-plasmonic coupling efficiency of 70% is achieved in our device.

3.3.3. SEIRA Sensing for PMMA and Monolayer ODT

To demonstrate on-chip SEIRA sensing using our waveguide-integrated hybrid device, poly(methyl methacrylate) (PMMA) was used as a model analyte because it is a widely used electron beam resist which can be patterned with nanometer accuracy and has a thoroughly characterized absorption spectrum in the mid-IR range. We first performed simulations to examine the feasibility. In the simulation, the PMMA was included as a 200-nm thick layer conformally covering only the nanorods (3 μm ×1.6 μm in the area) and its complex refractive index was used. The result in Fig. 3.4(c) apparently shows multiple absorption peaks due to PMMA analyte. As a comparison, for a waveguide covered with the same area of PMMA, but without the nanorods, its transmission spectrum shows no discernable spectroscopic features from PMMA absorption. These results verify that a bare waveguide does not provide enough field enhancement to sense a small amount of analyte patterned on it, while waveguide-integrated plasmonic resonators can detect them via SEIRA measurement.

In our experiments, the PMMA was patterned on the nanorods as shown in the optical microscope image in Figure 3a and illustrated in Fig. 3.5(b). First, the entire chip was spin-coated with PMMA (4% in chlorobenzene solvent) and then baked on a hotplate at 120 ℃ for 16 min, with the precaution to prevent heat-induced deformation of the gold nanorods. We then used EBL to pattern the PMMA layer into a patch only covering the nanorods. However, this process usually left a very thin layer of organic residue on the surface of the entire chip. Thus, an additional O_2 plasma cleaning process was necessary to remove the residues. The O_2 cleaning step also thins down the PMMA on the nanorods,

so it can be used to control the PMMA thickness. The final thickness of PMMA was determined with atomic force microscopy (AFM). The optical micrograph in Fig. 3.5(a) shows that only the nanorod array area is covered with a PMMA layer.

Table 3-1. Absorption peak positions, strengths and assignments of PMMA in the infrared range (~ 3.5 μm). ν_s and ν_a represent symmetric and antisymmetric stretching vibration, respectively.

Peak position	**Stength**	**Assignment**
2850 cm^{-1} (3508 nm)	very weak	combined band involving the O-CH_3
2915 cm^{-1} (3430 nm)	weak shoulder	combined band involving the O-CH_3 and $\nu_s(CH_2)$
2948 cm^{-1} (3392 nm)	strong	ν_s(C-H) of O-CH_3 with ν_s(C-H) of α-CH_3 and $\nu_a(CH_2)$
2995 cm^{-1} (3339 nm)	medium	ν_a(C-H) of O-CH_3 and ν_a(C-H) of α-CH_3

SEIRA measurement results are presented in Fig. 3.5(c). The top and middle panels show the transmission spectra of the device with PMMA film thickness of 230 nm and 160 nm, respectively. The asymmetric least square smoothing (AsLSS) method [154] is used to create the baselines for the measured curves. Compared to the transmission spectrum of the same device with no PMMA analyte (in the bottom panel), three spectroscopic changes can be observed due to PMMA: the redshift of the resonance peak, the reduction of the extinction ratio, and the appearance of multiple absorption peaks within the plasmonic resonance. The former two changes are simply due to the refractive index of PMMA, which results in shifting the resonance to longer wavelengths and modifying the waveguide-nanorod array coupling strength. The third change is the hallmark of SEIRA sensing. The infrared absorption peaks are from the vibrational modes of the C-H bonds in PMMA

molecules and they interfere with the broader plasmonic resonance of the nanorods to form the multiple resonance peaks in the transmission spectra.

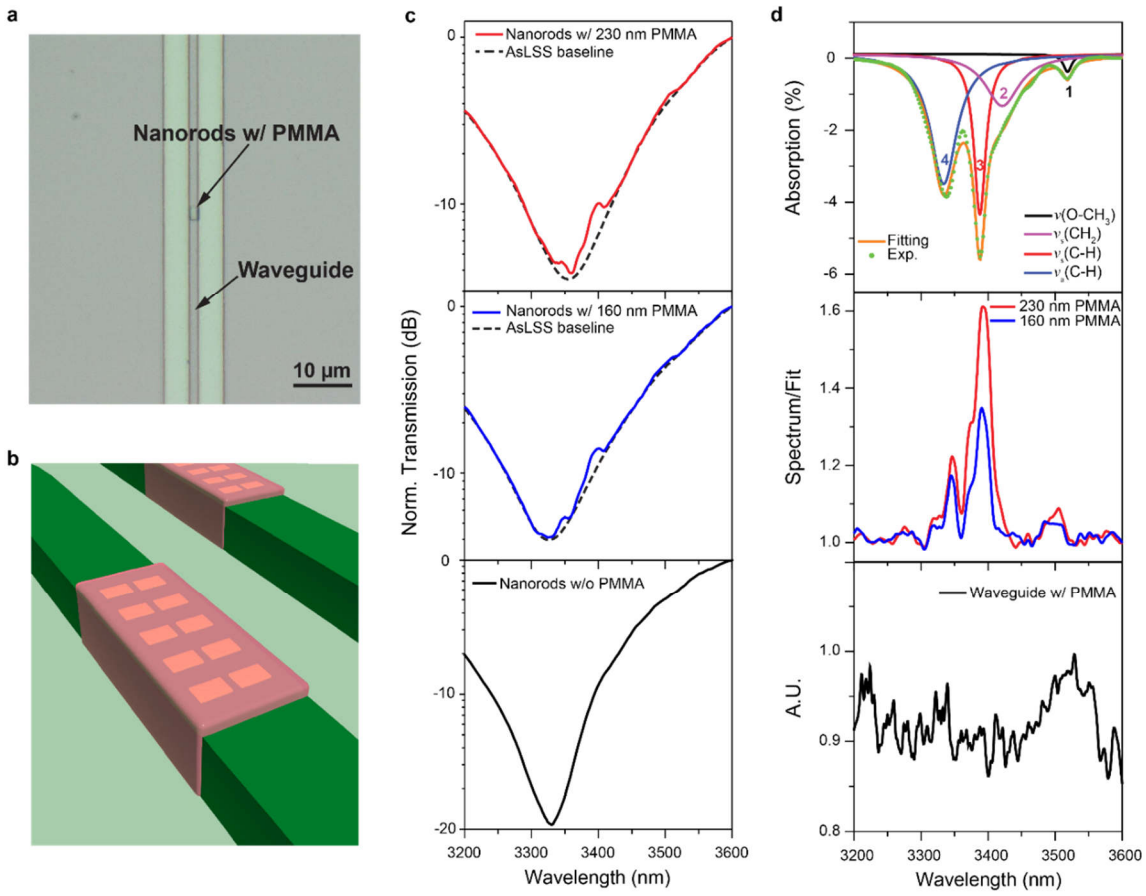

Figure 3.5. On-chip SEIRA sensing result for minute volume of PMMA analyte. (a) Optical microscope image of the waveguide-nanorod array device after PMMA patterning. (b) The 3D illustration of PMMA analyte on top of metallic nanorods. (c) Top and middle panel: transmission spectrum of nanorods covered with PMMA of ~230/160 nm thicknesses and the baselines extracted with the ASLSS method. Bottom panel: the spectrum of the same device without PMMA. The wavelength scan step is 2 nm. (d) Top panel: the FT-IR absorption spectrum of 400 nm thick PMMA film on a double-polished silicon wafer. Middle panel: absorption spectra for different thicknesses of PMMA in (c) after normalization to the baselines. Bottom panel: transmission

spectrum of a bare waveguide without nanorods and after adding a rectangular patch of 200 nm-thick PMMA.

To verify that the absorption peaks are indeed from the PMMA molecule's absorption, we used FI-IR to measure the absorption spectrum of a 400 nm PMMA film coated on a silicon wafer. The FTIR transmission spectrum can be precisely fitted with four individual Lorentz peaks, which are known to be induced by different vibrational modes of the chemical bonds in the PMMA molecules.[155] The detailed assignments of the absorption peaks are listed in Table 1. In Figure 3d, we compare the FIIR results with the SEIRA results, which is normalized by the AsLSS fitted baseline. The SEIRA absorption spectrum (middle panel, Fig. 3.5(d)) clearly shows three peaks, corresponding to peak 1), 3) and 4) in the FIIR spectrum. Their wavelength positions agree reasonably well with the FTIR spectrum despite small deviations likely due to the inaccuracy of the OPO laser output wavelength. The relative strengths between the peaks also agree with the FTIR result. The shoulder peak (peak 2), however, is hardly resolvable because of its close proximity to the nearby strong absorption peak (peak 3). The observation of the three distinct peaks in our SEIRA measurement is made possible by the resonant field enhancement afforded by the gold nanorod array. It is clear that thicker PMMA layer (230 nm) induces a larger red-shift of the plasmonic resonance and generate stronger SEIRA absorption peaks than the thinner PMMA layer (160 nm). It indicates that the probing range extends more than 160 nm from the nanorods' surface with the evanescent field of the surface plasmon.[156], [157] In a control experiment to verify the necessity of field enhancement by the nanorods, we patterned the same area of 200 nm thick PMMA on a bare silicon waveguide and performed the same measurement. The measured spectrum,

shown in the bottom panel of Fig. 3.5(d), presents no discernable absorption peaks, in agreement with the simulation result in Fig. 3.4(c). Apparently, the direct interaction between the evanescent field of the waveguide mode and such a small volume of PMMA is insufficient to generate absorption peaks above the noise background. It is thus confirmed that the observed absorption peaks are enabled by the surface enhancement of the plasmonic resonators.

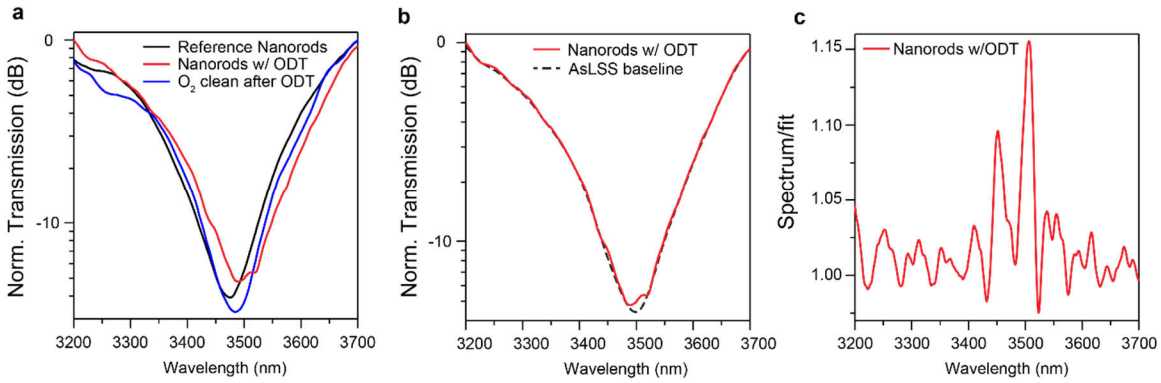

Figure 3.6. On-chip SEIRA sensing result of ODT monolayer. (a) The transmission spectra of the device at three different stages of the ODT experiment: clean device before ODT coating, device with ODT monolayer, and device cleaned by O_2 plasma after ODT coating and measurement. (b) The transmission spectrum of the same device after coating of an ODT monolayer. (c) The SEIRA spectrum of ODT monolayer in (b) after normalization by baseline, showing two prominent absorption peaks.

Next, we demonstrate SEIRA measurement of a self-assembled monolayer of ODT molecules on the surface of the gold nanorods. To do so, the device was incubated in ODT solution (1 μM in ethanol solution) overnight before performing SEIRA measurement. Comparing the transmission spectra measured before and after ODT coating in Fig. 3.6 (a), a small redshift of the resonance peak is observed. After normalization to the fitted baseline

of the plasmonic resonance, two absorption peaks become clearly visible in Fig. 3.6 (b) (c). Compared with the reported ODT absorption spectrum, the stronger peak at 3508 nm can be attributed to the symmetric stretching mode of the CH_2 bond (2850 cm^{-1}) and the weaker peak near 3460 nm to the Fermi-resonant symmetric stretching mode (2878 cm^{-1}) of the CH_3 bond.[54] The thickness (2.4 nm) of the ODT monolayer is ~1400 times smaller than the free-space wavelength and the number of ODT molecules in the gap region (hotspot) is only 2.4×10^5. Nevertheless, our device still generates absorption peaks with a signal-to-noise ratio better than 3. The intrinsically weak absorption of the C-H bond in the measured short-wavelength mid-IR band (2.5-3.7 μm), limited by the range of our OPO laser, is in part responsible for the weakness of the acquired signal. Therefore, our results demonstrate the potential of SEIRA sensing to be realized with a waveguide-integrated architecture.

To further improve the sensitivity of SEIRA sensing, two possible approaches can be taken. First, the field enhancement factor of the plasmonic resonator can be further improved by reducing the center gap width to only a few nm with more advanced fabrication methods[55], [122], [158] or using a coaxial aperture structure with higher field confinement.[121], [142] Second, SEIRA sensing can be performed in the long-wavelength mid-IR band around 5 μm range, which is the "fingerprint" range of organic molecules. In this spectral range, the C=O bond has ~ 5 times stronger absorption than that of the C-H bond in 3.5 μm band. However, to operate in the long-wavelength mid-IR range, the current silicon waveguide on an SOI substrate will suffer a high propagation loss due to the stronger absorption of the SiO_2 cladding layer. Low-loss waveguides can be fabricated with different material platforms, such as chalcogenide glasses or silicon on calcium fluoride substrate.[62], [159]

3.3.4. Additional Simulation Information

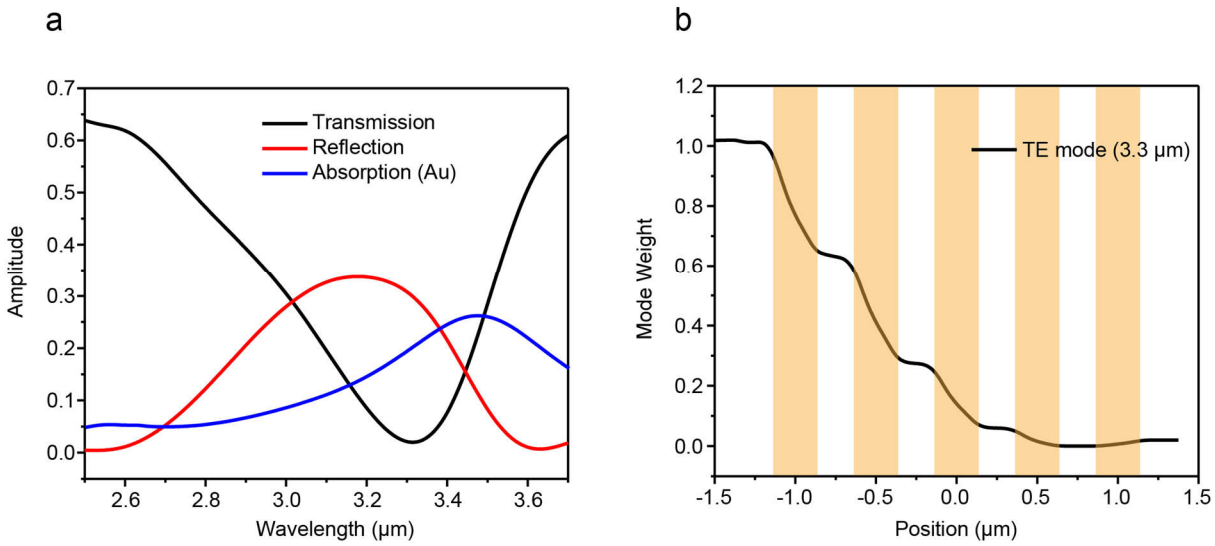

Figure 3.7. Additional simulation result for the narrow-gap devices. (a) Simulated spectrums of device transmission, reflection and Au absorption. (b) Simulated waveguide quasi-TE mode weight at different positions along the mode propagation direction. The yellow shadow areas indicate the metallic nanorods and the zero position is the center of the resonator.

Based on the 3D FDTD simulation, the transmission spectrum, the reflection spectrum and Au absorption spectrum of the device are shown in Fig. 3.7 (a). The device is the same as the device in Fig. 3.4 (c). In Fig. 3.7 (b), the evolution of TE mode weight along the mode propagation direction is shown. At the wavelength of 3.3 μm (maximum extinction ratio), the mode weight decreases quickly over a short distance.

3.4. Wide-Gap Nanorods Devices

Guided by the design proposed by Sang-Hyun Oh's group, we also fabricated devices consisting of wide-gap nanorods pairs on top of silicon waveguide, as shown in Fig. 3.8. In this design, comparing to narrow-gap device of a fixed gap width shown in the previous section, an additional tuning parameter is included as gap width (*d*). This parameter has a noticeable influence on the linewidth (Q factor) of this plasmonic resonance. In this round of investigation, we also fabricated devices include only three pairs of nanorods.

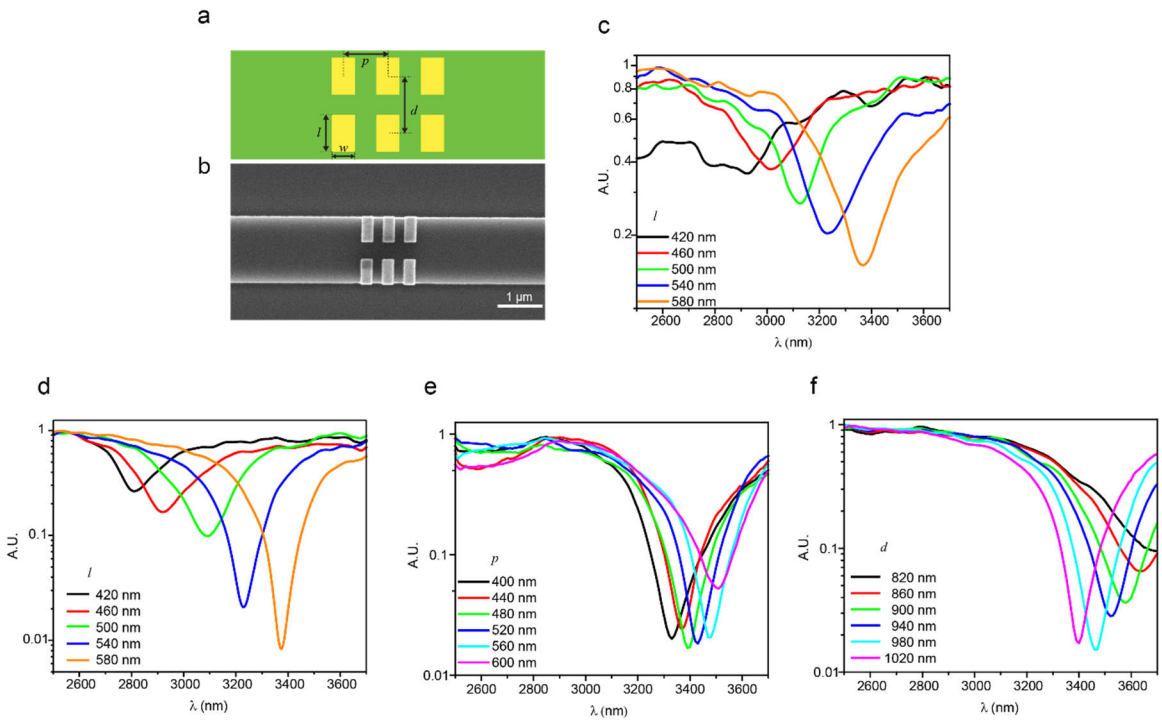

Figure 3.8. Results for wide-gap nanorods devices. (a) Schematic drawing of the wide-gap device with 3 pairs of nanorods. The parameters are labeled as width (*w*), period (*p*), distance (*d*) and length (*l*). (b) SEM image of the fabricated device. (c) Transmission spectrum measurement of the device (3 pairs of nanorods) (d) (e) (f) Transmission spectrum measurement of devices with 5 pairs

of nanorods with different tuning parameters. If not stated, the default parameters are: w = 0.275 µm, p = 0.5 µm, d = 1 µm and l = 0.58 µm.

We perform the same transmission measurement on the wide-gap plasmonic resonator. First, the plasmonic resonator consisting of only three pairs of nanorods is integrated on top of the waveguide (Fig. 3.8 (a) and (b)). Instead of a fixed nanogap as the device shown in the previous section, the lateral distance between nanorods is an additional tuning parameter (d). From our measurement results, even with only 3 pairs of nanorods atop the waveguide (Fig. 3.8(c)), a decent interaction between the resonator and waveguide can be observed in the transmission spectra. Adding another two pairs of nanorods (5 pairs in total), the extinction ratio increases dramatically as in Fig. 3.8 (d). Noticing here that the Q factor is slightly higher than the device in the main text because the tunable distance (d) helps optimize electromagnetic field coupling in the lateral direction. [143] Also, tuning other parameters also modifies the collectively exited plasmonic resonance and the coupling strength between resonator and waveguide as in Fig. 3.8 (e) (f). These parameters systematically optimize the device and provide an easy way to improve the performance.

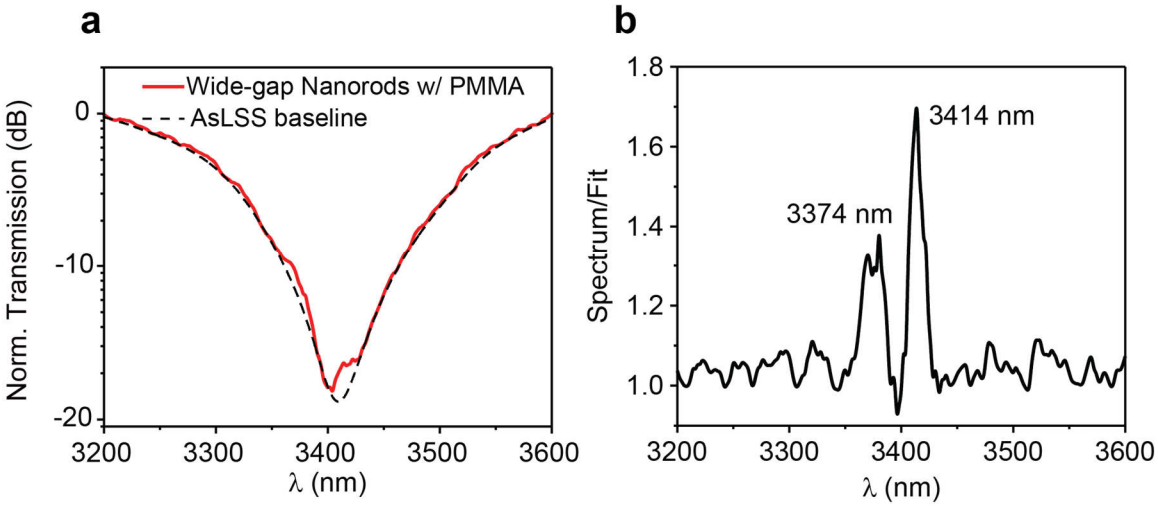

Figure 3.9. On-chip SEIRA sensing for small volume of PMMA using wide-gap devices. (a) Transmission spectrum of wide-gap device with PMMA analyte (~200 nm thickness) and the AsLSS baseline. (b) Extracted result of data divided by baseline from (a).

In Fig. 3.9, we show the SEIRA sensing result of PMMA using the wide-gap device (5 pairs of nanorods) shown In Fig. 3.8. In Fig. 3.9(a), the transmission spectrum of the device with PMMA and its AsLSS baseline are shown. In Fig. 3.9 (b), the result of data divided by baseline is plotted. Only two peaks can be resolved in the spectrum, comparing to the FT-IR measurement result in the previous section (Fig. 3.5 (d)). We believe this result is due to the limited electrical field enhancement in this wide-gap device comparing to nanogap device.

3.5. Modified Coupled Mode Theory

Figure 3.10. Schematic of the waveguide-resonator system with incoming and reflecting amplitude from two ports.

In the system presented in this chapter, one plasmonic resonator is coupled with one waveguide. From the perspective of the coupled mode theory, this single mode waveguide provides two ports coupling to one resonator (Fig. 3.10). This is similar to a waveguide side coupled photonic crystal cavity. [14] The following equations can be used to describe this system.

$$\frac{da}{dt} = \left(j\omega_0 - \frac{1}{\tau}\right)a + \kappa_1 s_{1+} + \kappa_2 s_{2+} \tag{3-2}$$

$$s_{1-} = C_{11}s_{1+} + C_{12}s_{2+} + ad_1 \tag{3-3}$$

$$s_{2-} = C_{21}s_{1+} + C_{22}s_{2+} + ad_2 \tag{3-4}$$

Here, s_{1+} and s_{1-} represents the incoming mode amplitude and reflecting mode amplitude for the input waveguide port. s_{2+} and s_{2-} are the counterparts for the output waveguide port. The amplitude a is normalized such that $|a|^2$ corresponds to the energy inside the resonator. ω_0 and τ are the resonant frequency and the total lifetime of the resonator respectively. κ_i is the coupling constant between the excitation of resonant field a and input amplitude s_{i+}. C_{ij} represents the scattering constant between s_{i-} and s_{j+}. d_i is the coupling constants between resonantor field a and reflecting amplitude s_{i-}.

By considering energy conservation and time-reversal symmetry of the system, the following conclusion can be acquired.[151], [152]

$$d_i = \kappa_i, \text{ where } i = 1, 2. \tag{3-5}$$

Also, the amplitude a can be written as $Ae^{j\omega t}$, where A is a constant, and ω is the input frequency. In the real measurement, only one port has input power, so $s_{2+} = 0$. The equations (3-2), (3-3) and (3-4) can be simplified as the following.

$$a = \frac{d_1 s_{1+}}{j(\omega - \omega_0) + 1/\tau} \tag{3-6}$$

$$s_{1-} = \left[C_{11} + \frac{{d_1}^2}{j(\omega - \omega_0) + 1/\tau} \right] s_{1+} \tag{3-7}$$

$$s_{2-} = \left[C_{21} + \frac{d_1 d_2}{j(\omega - \omega_0) + 1/\tau} \right] s_{1+} \tag{3-8}$$

In the real-world measurement, we only can measure the transmission T of the system through the waveguide, which is $|s_{2-}/s_{1+}|^2$. In addition, we propose the following assumptions.

$$C_{21} = t_0 = \alpha + j\beta \tag{3-9}$$

$${d_1}^2 = {d_2}^2 = \frac{1}{\tau_{te}} \tag{3-10}$$

$$\frac{1}{\tau_{te}} + \frac{1}{\tau_0} = \frac{1}{\tau} \tag{3-11}$$

In most waveguide-coupled dielectric cavity, because of the negligible off-resonance perturbation from the cavity, C_{21} simply equals -1.[152] For the waveguide-coupled plasmonic cavity, the metal induces a significant absorption even at off-resonance frequencies because its direct contact with waveguide. Thus, C_{21} becomes a complex number as in eq. (3-9). In eq. (3-10), we define $1/\tau_{te}$ as the total decay rate due to the coupling to both the input and output waveguides, where the subscript “te” stands for “total

external". Here, $1/\tau_0$ can still be defined as the intrinsic loss of the plasmonic resonator. However, in this model, C_{21} already incorporates the metallic loss experienced by waveguide; unlike in the case of waveguide-coupled dielectric cavity, the physical meaning of $1/\tau_0$ cannot be simply interpreted as the absorption and radiation loss of the plasmonic cavity.

$$s_{2-} = \left[(\alpha + j\beta) + \frac{1/\tau_{te}}{j(\omega - \omega_0) + 1/\tau} \right] s_{1+} \tag{3-12}$$

$$T = \frac{|s_{2-}|^2}{|s_{1+}|^2} = (\alpha^2 + \beta^2) + \frac{-\frac{2\beta}{\tau_{te}}(\omega - \omega_0) + \left(\frac{1}{\tau_{te}}\right)^2 + \frac{2\alpha}{\tau\tau_{te}}}{(\omega - \omega_0)^2 + \left(\frac{1}{\tau}\right)^2} \tag{3-13}$$

To provide a simplified equation for the actual curve fitting application, we have the following notation: $A = \alpha^2 + \beta^2, B = -\frac{2\beta}{\tau_{te}}$, $C = \left(\frac{1}{\tau_{te}}\right)^2 + \frac{2\alpha}{\tau\tau_{te}}$, $D = \left(\frac{1}{\tau}\right)^2$, so

$$T = \frac{|s_{2-}|^2}{|s_{1+}|^2} = A + \frac{B(w - w_0) + C}{(w - w_0)^2 + D} \tag{3-14}$$

After we have acquired all the parameters in the situation, we need to solve for α, β, $1/\tau$ and $1/\tau_{te}$.

$$\frac{1}{\tau} = +\sqrt{D} \tag{3-15}$$

$$\left(\frac{1}{\tau_{te}}\right)^2 = (C + 2AD) \pm \sqrt{(C + 2AD)^2 - (C^2 + B^2 D)} \tag{3-16}$$

$$\beta = -\frac{B\tau_{te}}{2} \tag{3-17}$$

$$\alpha = \frac{\tau\tau_{te}}{2}\left[C - \left(\frac{1}{\tau_{te}}\right)^2 \right] \tag{3-18}$$

To choose the correct solution for $1/\tau_{te}$, its value should be close to and smaller than the value of $1/\tau$, because the coupling between waveguide and metallic cavity should be much larger than cavity intrinsic loss.

To determine the minimum value of the transmission, we perform the first derivative on $T(\omega)$,

$$\frac{dT}{d\omega} = \left[A + \frac{B(\omega-\omega_0)+C}{(\omega-\omega_0)^2+D} \right]'_w = \frac{-B(\omega-\omega_0)^2 - 2C(\omega-\omega_0) + BD}{[(\omega-\omega_0)^2+D]^2} \tag{3-19}$$

Let $\frac{dT}{d\omega} = 0$ and two solutions will be acquired. In the acquired fitting results, ω_0 is lower than the frequency position of the transmission minima, so $\omega - \omega_0 > 0$. Also considering that $B<0, C<0$, we will get the following solution.

$$\omega - \omega_0 = -\frac{C + \sqrt{C^2 + B^2 D}}{B} \tag{3-20}$$

Insert this solution into the transmission equation $T(\omega)$, and recall the notations for A, B, C and D, we have

$$T_{\min} = (\alpha^2+\beta^2) - \frac{2\beta^2}{\left[\left[1+\frac{2\alpha\tau_{te}}{\tau}\right]^2 + \frac{4\beta^2{\tau_{te}}^2}{\tau^2}\right]^{1/2} + \left[1+\frac{2\alpha\tau_{te}}{\tau}\right]} \tag{3-21}$$

For simplicity, introduce a parameter $\eta = \frac{\tau_{te}}{\tau} = \frac{1/\tau}{1/\tau_{te}}$, noticing $\eta > 1$,

$$T_{\min}(\eta) = (\alpha^2+\beta^2) - \frac{2\beta^2}{[1+4\alpha\eta+4(\alpha^2+\beta^2)\eta^2]^{1/2} + (1+2\alpha\eta)} \tag{3-22}$$

We now explore the relation of η and $T_{\min}$. In order to find the extreme point of $T_{\min}$ for a fixed α and β, we calculate the 1st order derivative of the denominator of the second term in eq. (3-21),

$$T_{\min\_\text{core}}(\eta) = [1+4\alpha\eta+4(\alpha^2+\beta^2)\eta^2]^{1/2} + (1+2\alpha\eta) \tag{3-23}$$

$$\frac{dT_{\min\_\text{core}}}{d\eta} = \frac{1}{2}[1+4\alpha\eta+4(\alpha^2+\beta^2)\eta^2]^{-1/2} \cdot (4\alpha + 8(\alpha^2+\beta^2)\eta) + 2\alpha \tag{3-24}$$

Let $\frac{dT_{\min\_\text{core}}}{d\eta} = 0 \Rightarrow \beta^2\eta[(\alpha^2+\beta^2)\eta+\alpha] = 0$, we can get

$$\eta = -\frac{\alpha}{\alpha^2+\beta^2} \quad or \ 0 \ (\text{trivial}) \tag{3-25}$$

To ensure that this is a minimum point for $T_{\min\_\text{core}}$, we examine the 2nd order derivative,

$$\frac{d^2T_{\min\_\text{core}}}{d\eta^2} = \left\{\frac{1}{2}\left[1+4\alpha\eta+4(\alpha^2+\beta^2)\eta^2\right]^{-1/2}\cdot\left(4\alpha+8(\alpha^2+\beta^2)\eta\right)+2\alpha\right\}'_{\eta} \tag{3-26}$$
$$= -\frac{1}{4}\left[1+4\alpha\eta+4(\alpha^2+\beta^2)\eta^2\right]^{-3/2}\cdot\left[4\alpha+8(\alpha^2+\beta^2)\eta\right]^2+4\left[1+4\alpha\eta+4(\alpha^2+\beta^2)\eta^2\right]^{-1/2}\cdot(\alpha^2+\beta^2)$$

This 2nd order derivative is positive for the extracted parameters from different devices (Table 3-2), meaning $\eta = -\frac{\alpha}{\alpha^2+\beta^2}$ is indeed a local minimum for $T_{\min}(\eta)$.

Finally, we consider a special case when $\alpha = -1,\ \beta = 0$ (C_{21} = -1),

$$T = \frac{|s_{2-}|^2}{|s_{1+}|^2} = 1 - \frac{\frac{1}{\tau_{te}}\left(-\frac{1}{\tau_{te}}+\frac{2}{\tau}\right)}{(\omega-\omega_0)^2+\left(\frac{1}{\tau}\right)^2} \tag{3-27}$$

This is a typical symmetric Lorentz shape curve. The transmission minimum occurs when $\omega = \omega_0$.

$$T_{\min}(\eta) = 1 - \frac{\left(-1+\frac{2\tau_{te}}{\tau}\right)}{\left(\frac{\tau_{te}}{\tau}\right)^2} = \frac{1}{\eta^2} - \frac{2}{\eta} + 1 \tag{3-28}$$

When $\eta = 1$, $T_{\min}$ reaches 0. This result also can be predicted from the modified coupled mode (in eq.(3-25)) that $\eta = -\frac{\alpha}{\alpha^2+\beta^2} = 1$ for the condition $\alpha = -1,\ \beta = 0$.

Table 3-2. Extracted parameters from fitting measured transmission spectra (for 5 pair, narrow-gap device).

Rod length (nm)	α	β	$t_0^2 = \alpha^2+\beta^2$	$-\frac{\alpha}{\alpha^2+\beta^2}$	$\left.\frac{d^2T\_\text{core}}{d\eta^2}\right\|_{\eta=-\frac{\alpha}{\alpha^2+\beta^2}}$
320	-0.722	0.412	0.690	1.045	0.678
340	-0.882	0.246	0.838	1.052	0.242
360	-0.610	0.450	0.574	1.063	0.808
380	-0.738	0.379	0.688	1.073	0.573
400	-0.711	0.358	0.634	1.122	0.512
420	-0.709	0.433	0.690	1.027	0.751
440	-0.804	0.287	0.729	1.103	0.329

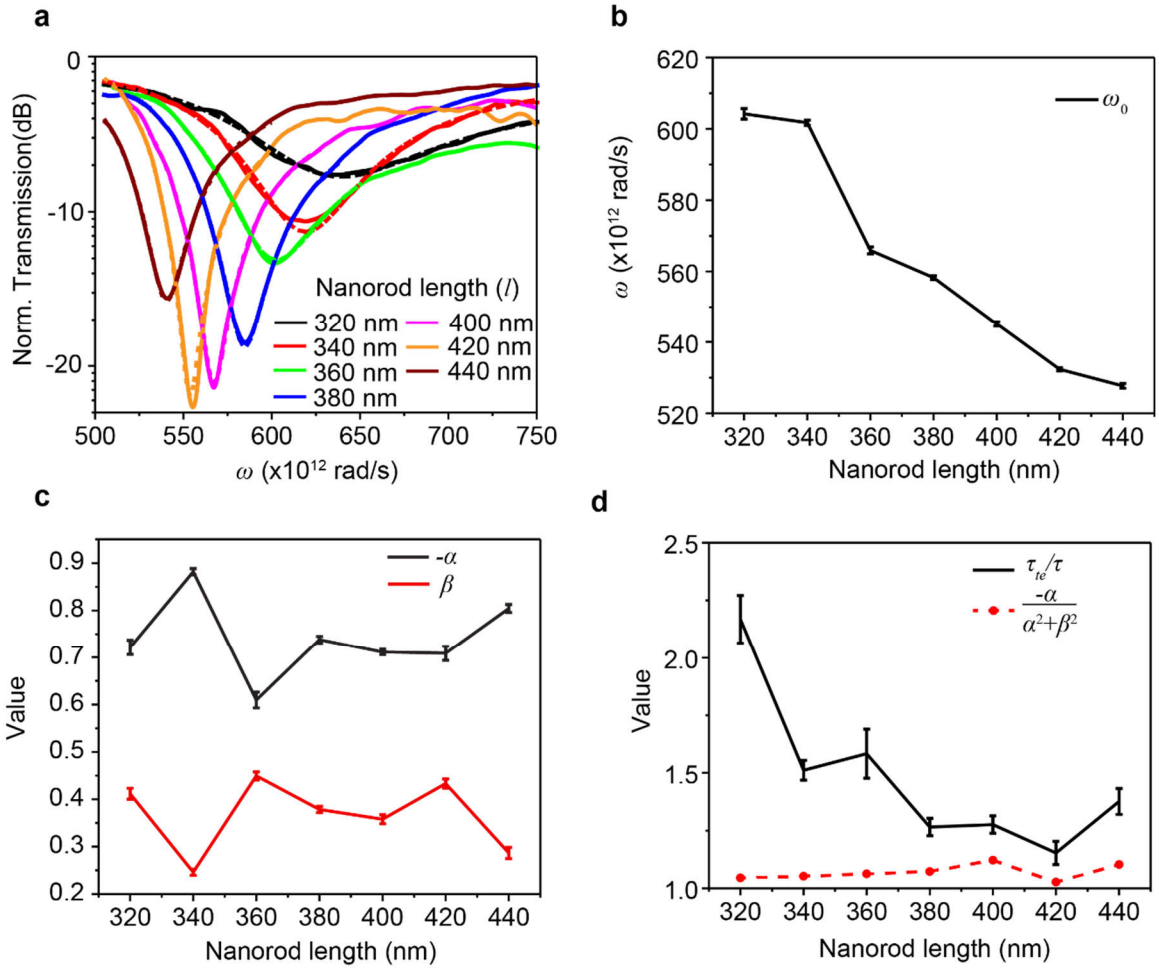

Figure 3.11. Plots of the fitted results and corresponding parameters. (a) Measurement result (solid lines) and fitting curves (dashed lines) in frequency domains. Note that the measured curves are multiplied with a constant of 0.7 (estimated broadband metallic transmission, acquired from comparing absolute transmission value between nanorods device and straight waveguide at wavelength away from resonance). (b) Extracted resonance frequency ω_0 for different devices. (c) Extracted values of $-\alpha$ and β for different devices. (d) Extracted values of t and $-\frac{\alpha}{\alpha^2+\beta^2}$ for different devices.

3.6. Conclusion

In conclusion, we have achieved highly efficient coupling to plasmonic resonators by directly integrating them on top of a mid-IR silicon waveguide. In our hybrid approach, the plasmonic resonance can be conveniently measured through the waveguide transmission and exhibit an extinction ratio of more than 20 dB. With this waveguide-plasmonic hybrid device, we demonstrate SEIRA sensing of both PMMA material and an ODT monolayer by measuring their C-H bond absorption peaks in the mid-IR band. This prototype waveguide-integrated SEIRA platform is an important step forward towards building a fully integrated and miniaturized SEIRA system. With the advancement of on-chip QCL and photodetectors for light generation and detection, along with microfluidic packaging for site-specific analyte delivery, it will be possible to achieve an integrated and multiplexed sensing system in a single package that is greatly smaller than conventional FTIR/microscope systems. Benefiting from the efficient coupling with the waveguide mode, this compact plasmonic device can also be used as an optical resonator as an alternative to dielectric cavities for on-chip nonlinear optics[160] and optical communications.[134] The strong interaction between a plasmonic resonator and a waveguide in the mid-IR range could potentially reveal fundamental physics including plasmon hybridization,[161] strong coupling of plasmon-phonon,[162]and waveguide integrated parity-time metamaterial.[163] Moreover, in addition to simple plasmonic resonators, more complicated and versatile metasurfaces[164], [165] may enable novel functionalities (e.g. multi-resonant and low-loss sensors) on such a hybrid platform.

Chapter 4. Conclusion Remarks

4.1. Summary

In this dissertation, we have discussed two research projects of the same central topic: the integration of silicon photonics and plasmonics. In Chapter 1, a brief overview of current research status of 2D material photonics and plasmonic sensing is presented as an introduction.

In Chapter 2, the three-dimensional on-chip integration of silicon waveguide, plasmonic gratings and black phosphorus is demonstrated. Based on this hybrid integration approach, a telecom-band photodetector is fabricated and characterized. The device has very short channel length (~ 60 nm) and compact footprint. The BP FET has a decent on-off ratio over 1000 with low dark current. Benefitted from internal gain mechanism, the device shows a high intrinsic responsivity of 10 A/W and a reasonable frequency response of 150 MHz at 3-dB roll-off point.

In Chapter 3, to further shrink the footprint of the plasmonic-photonic device, the metallic nanorod pairs are fabricated directly on top of a mid-IR silicon waveguide. Verified by 3D numerical simulation, an optical hotpot is created in the nanogap of 30 nm wide and the estimated field enhancement factor is ~ 60 in the wavelength near 3.5 μm. The plasmonic resonances are measured through waveguide transmission spectra with highest extinction ratio over 20 dB. Utilizing the hotspot and a high-brilliance OPO laser source, the absorption peaks of CH-bond in thin PMMA film and monolayer ODT are observed in the waveguide transmission spectra via SEIRA approach.

4.2. Future Perspective

In this section, we will briefly discuss potential research projects that can be pursued in the topic of the integration of plasmonics and photonics. In developing new optoelectronic applications, more compact devices can be developed with direct integration approach. For example, embedding 2D material inside plasmonic resonator can provide a method to tune the resonator property electrically via gate voltage. Combing with silicon waveguide, optoelectronic modulation and photodetection can be achieved.

For the on-chip SEIRA sensing application, there are also interesting experiments that can be exploited. For instance, the underlying coupling mechanism between plasmonic cavity and photonic waveguide needs a thorough theoretical investigation. Moreover, different types of plasmonic cavities can be integrated atop the waveguide for improved efficiency and field confinement. In addition, the new developments of OPO laser sources enable the sensing application in 6-8 μm wavelength range. Combining this with chalcogenide glass which supports broadband mid-IR waveguide, new sensing devices that can directly measure molecular absorption peaks in the “fingerprint” region become plausible. Further, integrating this photonic/plasmonic platform with the mature microfluidics analyte delivery technology may provide a complete package for portable sensing system.

References

[1] M. N. Zervas and C. A. Codemard, "High Power Fiber Lasers: A Review," *IEEE J. Sel. Top. Quantum Electron.*, vol. 20, no. 5, pp. 219–241, Sep. 2014.

[2] J. Heo, "Rare-earth doped chalcogenide glasses for fiber-optic amplifiers," *J. Non. Cryst. Solids*, vol. 326–327, pp. 410–415, Oct. 2003.

[3] O. S. Wolfbeis, "Fiber-optic chemical sensors and biosensors," *Analytical Chemistry*, vol. 76, no. 12. American Chemical Society, pp. 3269–3284, 2004.

[4] R. A. Soref and J. P. Lorenzo, "Single-crystal silicon: a new material for 1.3 and 1.6 μm integrated-optical components," *Electron. Lett.*, vol. 21, no. 21, p. 953, 1985.

[5] I. Staude and J. Schilling, "Metamaterial-inspired silicon nanophotonics," *Nat. Photonics*, vol. 11, no. 5, pp. 274–284, 2017.

[6] J. E. Bowers, "Roadmap on silicon photonics," *J. Opt.*, vol. 18, no. July, p. 073003, 2016.

[7] Z. Wang *et al.*, "Novel Light Source Integration Approaches for Silicon Photonics," *Laser Photonics Rev.*, vol. 11, no. 4, p. 1700063, Jul. 2017.

[8] J.-M. Brosi, C. Koos, L. C. Andreani, M. Waldow, J. Leuthold, and W. Freude, "High-speed low-voltage electro-optic modulator with a polymer-infiltrated silicon photonic crystal waveguide," *Opt. Express*, vol. 16, no. 6, pp. 4177–4191, Mar. 2008.

[9] M. A. Foster, A. C. Turner, J. E. Sharping, B. S. Schmidt, M. Lipson, and A. L. Gaeta, "Broad-band optical parametric gain on a silicon photonic chip," *Nature*, vol. 441, no. 7096, pp. 960–963, Jun. 2006.

[10] M. Li, W. H. P. Pernice, C. Xiong, T. Baehr-Jones, M. Hochberg, and H. X. Tang, "Harnessing optical forces in integrated photonic circuits," *Nature*, vol. 456, no. 7221, pp. 480–484, Nov. 2008.

[11] C. Rios *et al.*, "Integrated all-photonic non-volatile multi-level memory," *Nat. Photonics*, vol. 9, no. 11, pp. 725–732, 2015.

[12] K. Saha *et al.*, "Modelocking and Femtosecond Pulse Generation in Chip-Based Frequency Combs," *Opt. Express*, vol. 21, no. 1, p. 1335, Jan. 2012.

[13] H. Li, Y. Chen, J. Noh, S. Tadesse, and M. Li, "Multichannel cavity optomechanics for all-optical amplification of radio frequency signals.," *Nat. Commun.*, vol. 3, p. 1091, Jan. 2012.

[14] H. Li and M. Li, "Optomechanical photon shuttling between photonic cavities," *Nat. Nanotechnol.*, vol. 9, no. 11, pp. 913–919, Nov. 2014.

[15] Y. Shen *et al.*, "Deep learning with coherent nanophotonic circuits," *Nat. Photonics*, vol. 11, no. 7, pp. 441–446, Jun. 2017.

[16] H. W. Kroto, J. R. Heath, S. C. O'Brien, R. F. Curl, and R. E. Smalley, "C60: Buckminsterfullerene," *Nature*, vol. 318, no. 6042, pp. 162–163, Nov. 1985.

[17] S. Iijima, "Helical microtubules of graphitic carbon," *Nature*, vol. 354, no. 6348, pp. 56–58, Nov. 1991.

[18] T. Dürkop, S. A. Getty, E. Cobas, and M. S. Fuhrer, "Extraordinary Mobility in Semiconducting Carbon Nanotubes," *Nano Lett.*, vol. 4, no. 1, pp. 35–39, 2004.

[19] M. F. Yu, O. Lourie, M. J. Dyer, K. Moloni, T. F. Kelly, and R. S. Ruoff, "Strength and breaking mechanism of multiwalled carbon nanotubes under tensile load," *Science*, vol. 287, no. 5453, pp. 637–640, Sep. 2000.

[20] K. S. Novoselov *et al.*, “Electric field effect in atomically thin carbon films.,” *Science*, vol. 306, no. 5696, pp. 666–9, Oct. 2004.

[21] K. F. Mak, C. Lee, J. Hone, J. Shan, and T. F. Heinz, “Atomically Thin MoS_2: A New Direct-Gap Semiconductor,” *Phys. Rev. Lett.*, vol. 105, no. 13, p. 136805, Sep. 2010.

[22] K. K. Kim *et al.*, “Synthesis of Monolayer Hexagonal Boron Nitride on Cu Foil Using Chemical Vapor Deposition,” *Nano Lett.*, vol. 12, no. 1, pp. 161–166, Jan. 2012.

[23] B. Huang *et al.*, “Layer-dependent ferromagnetism in a van der Waals crystal down to the monolayer limit,” *Nature*, vol. 546, no. 7657, pp. 270–273, Jun. 2017.

[24] L. Li *et al.*, “Black phosphorus field-effect transistors,” *Nat. Nanotechnol.*, vol. 9, no. 5, pp. 372–377, Mar. 2014.

[25] L. M. Malard, T. V. Alencar, A. P. M. Barboza, K. F. Mak, and A. M. de Paula, “Observation of intense second harmonic generation from MoS_{2} atomic crystals,” *Phys. Rev. B*, vol. 87, no. 20, p. 201401, May 2013.

[26] B. Huang *et al.*, “Layer-dependent ferromagnetism in a van der Waals crystal down to the monolayer limit,” *Nature*, vol. 546, no. 7657, pp. 270–273, Jun. 2017.

[27] L. M. Malard, M. A. Pimenta, G. Dresselhaus, and M. S. Dresselhaus, “Raman spectroscopy in graphene,” *Physics Reports*, vol. 473, no. 5–6. North-Holland, pp. 51–87, 01-Apr-2009.

[28] X. Xu, W. Yao, D. Xiao, and T. F. Heinz, “Spin and pseudospins in layered transition metal dichalcogenides,” *Nature Physics*, vol. 10, no. 5. Nature Publishing Group, pp. 343–350, 01-May-2014.

[29] D. N. Basov, M. M. Fogler, and F. J. Garcia de Abajo, “Polaritons in van der Waals materials,” *Science*, vol. 354, no. 6309, pp. aag1992-aag1992, Oct. 2016.

[30] A. Castellanos-Gomez *et al.*, “Deterministic transfer of two-dimensional materials by all-dry viscoelastic stamping,” *2D Mater.*, vol. 1, no. 1, p. 011002, Apr. 2014.

[31] S. Wu *et al.*, “Monolayer semiconductor nanocavity lasers with ultralow thresholds,” *Nature*, vol. 520, no. 7545, pp. 69–72, 2015.

[32] M. Furchi *et al.*, “Microcavity-integrated graphene photodetector,” *Nano Lett.*, vol. 12, no. 6, pp. 2773–2777, Jun. 2012.

[33] M. Holland *et al.*, “Atomically flat and uniform relaxed III–V epitaxial films on silicon substrate for heterogeneous and hybrid integration,” *Sci. Rep.*, vol. 7, no. 1, p. 14632, Dec. 2017.

[34] G.-H. Duan *et al.*, “Hybrid III-V on silicon lasers for photonic integrated circuits on silicon,” in *IEEE Journal of Selected Topics in Quantum Electronics*, 2014, vol. 7, no. 1, p. 90020X.

[35] L. Wang *et al.*, “One-dimensional electrical contact to a two-dimensional material,” *Science*, vol. 342, no. 6158, pp. 614–617, Nov. 2013.

[36] M. Liu *et al.*, “A graphene-based broadband optical modulator,” *Nature*, vol. 474, no. 7349, pp. 64–67, Jun. 2011.

[37] X. Gan *et al.*, “Chip-integrated ultrafast graphene photodetector with high responsivity,” *Nat. Photonics*, vol. 7, no. 11, pp. 883–887, Sep. 2013.

[38] N. Youngblood, C. Chen, S. J. Koester, and M. Li, “Waveguide-integrated black phosphorus photodetector with high responsivity and low dark current,” *Nat. Photonics*, vol. 9, no. April, pp. 249–252, Mar. 2015.

[39] M. Freitag, T. Low, F. N. Xia, and P. Avouris, “Photoconductivity of biased graphene,” *Nat. Photonics*, vol. 7, no. 1, pp. 53–59, Dec. 2013.

[40] Y.-Q. Bie *et al.*, “A MoTe2-based light-emitting diode and photodetector for silicon photonic integrated circuits,” *Nat. Nanotechnol.*, vol. 12, no. 12, pp. 1124–1129, Oct. 2017.

[41] O. Lazcka, F. J. Del Campo, and F. X. Muñoz, “Pathogen detection: A perspective of traditional methods and biosensors,” *Biosensors and Bioelectronics*, vol. 22, no. 7. Elsevier, pp. 1205–1217, 15-Feb-2007.

[42] F. G. Bănică, *Chemical Sensors and Biosensors: Fundamentals and Applications*. John Wiley & Sons Inc, 2012.

[43] N. Bhalla, P. Jolly, N. Formisano, and P. Estrela, “Introduction to biosensors,” *Essays Biochem.*, vol. 60, no. June, pp. 1–8, 2016.

[44] J. Pendry, “Praying tricks with light,” *Science*, vol. 285, no. 5434. American Association for the Advancement of Science, pp. 1687–1688, 03-Sep-1999.

[45] J. A. Schuller, E. S. Barnard, W. Cai, Y. C. Jun, J. S. White, and M. L. Brongersma, “Plasmonics for extreme light concentration and manipulation.,” *Nat. Mater.*, vol. 9, no. 3, pp. 193–204, Mar. 2010.

[46] J. N. Anker, W. P. Hall, O. Lyandres, N. C. Shah, J. Zhao, and R. P. Van Duyne, “Biosensing with plasmonic nanosensors,” *Nat. Mater.*, vol. 7, no. 6, pp. 442–453, Jun. 2008.

[47] T. Althaus, W. Eisfeld, R. Lohrmann, and M. Stockburger, “Application of Raman Spectroscopy to Retinal Proteins,” *Isr. J. Chem.*, vol. 35, no. 3–4, pp. 227–251, 1995.

[48] K. Kneipp *et al.*, "Single Molecule Detection Using Surface-Enhanced Raman Scattering (SERS)," *Phys. Rev. Lett.*, vol. 78, no. 9, pp. 1667–1670, Mar. 1997.

[49] F. Neubrech, A. Pucci, T. W. Cornelius, S. Karim, A. García-Etxarri, and J. Aizpurua, "Resonant plasmonic and vibrational coupling in a tailored nanoantenna for infrared detection," *Phys. Rev. Lett.*, vol. 101, no. 15, p. 157403, Oct. 2008.

[50] T. Steinle, F. Neubrech, A. Steinmann, X. Yin, and H. Giessen, "Mid-infrared Fourier-transform spectroscopy with a high-brilliance tunable laser source: investigating sample areas down to 5 μm diameter," *Opt. Express*, vol. 23, no. 9, p. 11105, 2015.

[51] A. Hartstein, J. R. Kirtley, and J. C. Tsang, "Enhancement of the infrared absorption from molecular monolayers with thin metal overlayers," *Phys. Rev. Lett.*, vol. 45, no. 3, pp. 201–204, Jul. 1980.

[52] X. Chen *et al.*, "Atomic layer lithography of wafer-scale nanogap arrays for extreme confinement of electromagnetic waves," *Nat. Commun.*, vol. 4, p. 2361, Sep. 2013.

[53] R. Adato *et al.*, "Ultra-sensitive vibrational spectroscopy of protein monolayers with plasmonic nanoantenna arrays," *Proc. Natl. Acad. Sci.*, vol. 106, no. 46, pp. 19227–19232, Nov. 2009.

[54] L. V Brown, X. Yang, K. Zhao, B. Y. Zheng, P. Nordlander, and N. J. Halas, "Fan-shaped gold nanoantennas above reflective substrates for surface-enhanced infrared absorption (SEIRA)," *Nano Lett.*, vol. 15, no. 2, pp. 1272–1280, Feb. 2015.

[55] L. Dong *et al.*, "Nanogapped Au Antennas for Ultrasensitive Surface-Enhanced Infrared Absorption Spectroscopy," *Nano Lett.*, vol. 17, no. 9, pp. 5768–5774, Sep. 2017.

[56] R. Guo *et al.*, "High-bit rate ultra-compact light routing with mode-selective on-chip nanoantennas," *Sci. Adv.*, vol. 3, no. 7, p. e1700007, Jul. 2017.

[57] Z. Li *et al.*, "Controlling propagation and coupling of waveguide modes using phase-gradient metasurfaces," *Nat. Nanotechnol.*, vol. 12, no. 7, pp. 675–683, 2017.

[58] Y. Luo *et al.*, "On-Chip Hybrid Photonic–Plasmonic Light Concentrator for Nanofocusing in an Integrated Silicon Photonics Platform," *Nano Lett.*, vol. 15, no. 2, pp. 849–856, Feb. 2015.

[59] L. V. Brown, K. Zhao, N. King, H. Sobhani, P. Nordlander, and N. J. Halas, "Surface-Enhanced Infrared Absorption Using Individual Cross Antennas Tailored to Chemical Moieties," *J. Am. Chem. Soc.*, vol. 135, no. 9, pp. 3688–3695, Mar. 2013.

[60] F. Peyskens, A. Dhakal, P. Van Dorpe, N. Le Thomas, and R. Baets, "Surface Enhanced Raman Spectroscopy Using a Single Mode Nanophotonic-Plasmonic Platform," *ACS Photonics*, vol. 3, no. 1, pp. 102–108, Jan. 2016.

[61] A. Dhakal, P. C. Wuytens, F. Peyskens, K. Jans, N. Le Thomas, and R. Baets, "Nanophotonic Waveguide Enhanced Raman Spectroscopy of Biological Submonolayers," *ACS Photonics*, vol. 3, no. 11, pp. 2141–2149, Nov. 2016.

[62] Y. Chen, H. Lin, J. Hu, and M. Li, "Heterogeneously integrated silicon photonics for the mid-infrared and spectroscopic sensing.," *ACS Nano*, vol. 8, no. 7, pp. 6955–61, Jul. 2014.

[63] S. Das, W. Zhang, M. Demarteau, A. Hoffmann, M. Dubey, and A. Roelofs, "Tunable transport gap in phosphorene," *Nano Lett.*, vol. 14, no. 10, pp. 5733–5739, Oct. 2014.

[64] X. Chen *et al.*, "High-quality sandwiched black phosphorus heterostructure and its quantum oscillations," *Nat. Commun.*, vol. 6, no. 1, p. 7315, Dec. 2015.

[65] F. Xia, H. Wang, and Y. Jia, "Rediscovering black phosphorus as an anisotropic layered material for optoelectronics and electronics," *Nat. Commun.*, vol. 5, no. 1, p. 4458, Dec. 2014.

[66] N. Haratipour and S. J. Koester, "Ambipolar Black Phosphorus MOSFETs with Record n-Channel Transconductance," *IEEE Electron Device Lett.*, vol. 37, no. 1, pp. 103–106, Jan. 2016.

[67] F. Xia, H. Wang, D. Xiao, M. Dubey, and A. Ramasubramaniam, "Two-dimensional material nanophotonics," *Nat. Photonics*, vol. 8, no. 12, pp. 899–907, Nov. 2014.

[68] F. Xia, T. Mueller, Y.-M. Lin, A. Valdes-Garcia, and P. Avouris, "Ultrafast graphene photodetector," *Nat. Nanotechnol.*, vol. 4, no. 12, pp. 839–843, 2009.

[69] C. T. Phare, Y.-H. Daniel Lee, J. Cardenas, and M. Lipson, "Graphene electro-optic modulator with 30 GHz bandwidth," *Nat. Photonics*, vol. 9, no. 8, pp. 511–514, Jul. 2015.

[70] M. Huang *et al.*, "Broadband Black-Phosphorus Photodetectors with High Responsivity," *Adv. Mater.*, vol. 28, no. 18, pp. 3481–3485, May 2016.

[71] Q. Guo *et al.*, "Black Phosphorus Mid-Infrared Photodetectors with High Gain," *Nano Lett.*, vol. 16, no. 7, pp. 4648–4655, Jul. 2016.

[72] X. Wang, Z. Cheng, K. Xu, H. K. Tsang, and J.-B. Xu, "High-responsivity graphene/silicon-heterostructure waveguide photodetectors," *Nat. Photonics*, vol. 7, no. 11, pp. 888–891, Sep. 2013.

[73] N. Youngblood, Y. Anugrah, R. Ma, S. J. Koester, and M. Li, "Multifunctional

graphene optical modulator and photodetector integrated on silicon waveguides.," *Nano Lett.*, vol. 14, no. 5, pp. 2741–6, May 2014.

[74] M. Engel *et al.*, "Light–matter interaction in a microcavity-controlled graphene transistor," *Nat. Commun.*, vol. 3, no. May, p. 906, Jun. 2012.

[75] S. I. Bozhevolnyi, V. S. Volkov, E. Devaux, J.-Y. Laluet, and T. W. Ebbesen, "Channel plasmon subwavelength waveguide components including interferometers and ring resonators.," *Nature*, vol. 440, no. 7083, pp. 508–11, Mar. 2006.

[76] S. Lal, S. Link, and N. J. Halas, "Nano-optics from sensing to waveguiding," *Nat. Photonics*, vol. 1, no. 11, pp. 641–648, Nov. 2007.

[77] T. Ishi, J. Fujikata, K. Marita, T. Baba, and K. Ohashi, "Si nano-photodiode with a surface plasmon antenna," *Japanese J. Appl. Physics, Part 2 Lett.*, vol. 44, no. 12–15, pp. L364–L366, Mar. 2005.

[78] A. Akbari, R. N. Tait, and P. Berini, "Surface plasmon waveguide Schottky detector," *Opt. Express*, vol. 18, no. 8, p. 8505, Apr. 2010.

[79] I. Goykhman, B. Desiatov, J. Khurgin, J. Shappir, and U. Levy, "Locally Oxidized Silicon Surface-Plasmon Schottky Detector for Telecom Regime," *Nano Lett.*, vol. 11, no. 6, pp. 2219–2224, Jun. 2011.

[80] I. Goykhman *et al.*, "On-Chip Integrated, Silicon-Graphene Plasmonic Schottky Photodetector with High Responsivity and Avalanche Photogain," *Nano Lett.*, vol. 16, no. 5, pp. 3005–3013, May 2016.

[81] K. C. Y. Huang, M.-K. Seo, Y. Huo, T. Sarmiento, J. S. Harris, and M. L. Brongersma, "Antenna electrodes for controlling electroluminescence," *Nat.*

Commun., vol. 3, p. 1005, Aug. 2012.

[82] M. Wu, Z. Han, and V. Van, "Efficient coupler between silicon photonic and metal-insulator-silicon-metal plasmonic waveguides," *Opt. Express*, vol. 18, no. 11, pp. 11728–36, 2010.

[83] C. Delacour *et al.*, "Efficient Directional Coupling between Silicon and Copper Plasmonic Nanoslot Waveguides: toward Metal−Oxide−Silicon Nanophotonics," *Nano Lett.*, vol. 10, no. 8, pp. 2922–2926, Aug. 2010.

[84] R. M. Briggs, J. Grandidier, S. P. Burgos, E. Feigenbaum, and H. A. Atwater, "Efficient Coupling between Dielectric-Loaded Plasmonic and Silicon Photonic Waveguides," *Nano Lett.*, vol. 10, no. 12, pp. 4851–4857, Dec. 2010.

[85] D. Y. Fedyanin, D. I. Yakubovsky, R. V. Kirtaev, and V. S. Volkov, "Ultralow-Loss CMOS Copper Plasmonic Waveguides," *Nano Lett.*, vol. 16, no. 1, pp. 362–366, Jan. 2016.

[86] M. P. Nielsen *et al.*, "Adiabatic Nanofocusing in Hybrid Gap Plasmon Waveguides on the Silicon-on-Insulator Platform," *Nano Lett.*, vol. 16, no. 2, pp. 1410–1414, Feb. 2016.

[87] H. Choo *et al.*, "Nanofocusing in a metal–insulator–metal gap plasmon waveguide with a three-dimensional linear taper," *Nat. Photonics*, vol. 6, no. 12, pp. 838–844, Nov. 2012.

[88] M. Ono *et al.*, "Deep-subwavelength plasmonic mode converter with large size reduction for Si-wire waveguide," *Optica*, vol. 3, no. 9, p. 999, Sep. 2016.

[89] M. Engel, M. Steiner, and P. Avouris, "Black Phosphorus Photodetector for Multispectral, High-Resolution Imaging," *Nano Lett.*, vol. 14, no. 11, pp. 6414–

6417, Nov. 2014.

[90] H. Yuan *et al.*, "Polarization-sensitive broadband photodetector using a black phosphorus vertical p–n junction," *Nat. Nanotechnol.*, vol. 10, no. 8, pp. 707–713, Jun. 2015.

[91] H. Liu, A. T. Neal, M. Si, Y. Du, and P. D. Ye, "The Effect of Dielectric Capping on Few-Layer Phosphorene Transistors: Tuning the Schottky Barrier Heights," *IEEE Electron Device Lett.*, vol. 35, no. 7, pp. 795–797, Jul. 2014.

[92] S. A. Maier *et al.*, "Local detection of electromagnetic energy transport below the diffraction limit in metal nanoparticle plasmon waveguides," *Nat. Mater.*, vol. 2, no. 4, pp. 229–232, Apr. 2003.

[93] F. J. García-Vidal, H. J. Lezec, T. W. Ebbesen, and L. Martín-Moreno, "Multiple Paths to Enhance Optical Transmission through a Single Subwavelength Slit," *Phys. Rev. Lett.*, vol. 90, no. 21, p. 213901, May 2003.

[94] F. J. Garcia-Vidal, L. Martin-Moreno, T. W. Ebbesen, and L. Kuipers, "Light passing through subwavelength apertures," *Rev. Mod. Phys.*, vol. 82, no. 1, pp. 729–787, Mar. 2010.

[95] J. Miao, S. Zhang, L. Cai, M. Scherr, and C. Wang, "Ultrashort Channel Length Black Phosphorus Field-Effect Transistors," *ACS Nano*, vol. 9, no. 9, pp. 9236–9243, Sep. 2015.

[96] A. V. Penumatcha, R. B. Salazar, and J. Appenzeller, "Analysing black phosphorus transistors using an analytic Schottky barrier MOSFET model," *Nat. Commun.*, vol. 6, no. 1, p. 8948, Dec. 2015.

[97] D. Taillaert, P. Bienstman, and R. Baets, "Compact efficient broadband grating

coupler for silicon-on-insulator waveguides.," *Opt. Lett.*, vol. 29, no. 23, pp. 2749–2751, 2004.

[98] M. Massicotte *et al.*, "Picosecond photoresponse in van der Waals heterostructures," *Nat. Nanotechnol.*, vol. 11, no. 1, pp. 42–46, Oct. 2015.

[99] O. Lopez-Sanchez, D. Lembke, M. Kayci, A. Radenovic, and A. Kis, "Ultrasensitive photodetectors based on monolayer MoS2," *Nat. Nanotechnol.*, vol. 8, no. 7, pp. 497–501, 2013.

[100] M. M. Furchi, D. K. Polyushkin, A. Pospischil, and T. Mueller, "Mechanisms of photoconductivity in atomically thin MoS_2," *Nano Lett.*, vol. 14, no. 11, pp. 6165–6170, Nov. 2014.

[101] H. Liu *et al.*, "Phosphorene: An Unexplored 2D Semiconductor with a High Hole Mobility," *ACS Nano*, vol. 8, no. 4, pp. 4033–4041, Apr. 2014.

[102] B. E. A. Saleh and M. C. Teich, *Fundamentals of Photonics*. New York, USA: John Wiley & Sons, Inc., 1991.

[103] J. Qiao, X. Kong, Z.-X. Hu, F. Yang, and W. Ji, "High-mobility transport anisotropy and linear dichroism in few-layer black phosphorus," *Nat. Commun.*, vol. 5, no. 1, p. 4475, Dec. 2014.

[104] M. Buscema, D. J. Groenendijk, S. I. Blanter, G. A. Steele, H. S. J. Van Der Zant, and A. Castellanos-Gomez, "Fast and broadband photoresponse of few-layer black phosphorus field-effect transistors.," *Nano Lett.*, vol. 14, no. 6, pp. 3347–3352, May 2014.

[105] L. Ye, H. Li, Z. Chen, and J. Xu, "Near-Infrared Photodetector Based on MoS2/Black Phosphorus Heterojunction," *ACS Photonics*, vol. 3, no. 4, pp. 692–

699, 2016.

[106] L. Li, M. Engel, D. B. Farmer, S. J. Han, and H. S. P. Wong, "High-Performance p-Type Black Phosphorus Transistor with Scandium Contact," *ACS Nano*, vol. 10, no. 4, pp. 4672–4677, Apr. 2016.

[107] G. Long *et al.*, "Achieving Ultrahigh Carrier Mobility in Two-Dimensional Hole Gas of Black Phosphorus," *Nano Lett.*, vol. 16, no. 12, pp. 7768–7773, Dec. 2016.

[108] J. Aizpurua, G. W. Bryant, L. J. Richter, F. J. García de Abajo, B. K. Kelley, and T. Mallouk, "Optical properties of coupled metallic nanorods for field-enhanced spectroscopy," *Phys. Rev. B*, vol. 71, no. 23, p. 235420, Jun. 2005.

[109] A. Barik, X. Chen, and S.-H. Oh, "Ultralow-Power Electronic Trapping of Nanoparticles with Sub-10 nm Gold Nanogap Electrodes," *Nano Lett.*, vol. 16, no. 10, pp. 6317–6324, Oct. 2016.

[110] A. Melikyan *et al.*, "High-speed plasmonic phase modulators," *Nat. Photon.*, vol. 8, no. 3, pp. 229–233, Feb. 2014.

[111] N. Youngblood, R. Peng, A. Nemilentsau, T. Low, and M. Li, "Layer-Tunable Third-Harmonic Generation in Multilayer Black Phosphorus," *ACS Photonics*, vol. 4, no. 1, pp. 8–14, Jan. 2017.

[112] G. Fiori *et al.*, "Electronics based on two-dimensional materials," *Nat. Nanotechnol.*, vol. 9, no. 10, pp. 768–779, Oct. 2014.

[113] A. E. Willner, S. Khaleghi, M. R. Chitgarha, and O. F. Yilmaz, "All-optical signal processing," *J. Light. Technol.*, vol. 32, no. 4, pp. 660–680, Feb. 2014.

[114] A. G. Brolo, "Plasmonics for future biosensors," *Nature Photonics*, vol. 6, no. 11. pp. 709–713, 2012.

[115] C. L. Haynes, A. D. McFarland, and R. P. Van Duyne, "Surface-Enhanced Raman Spectroscopy," *Anal. Chem.*, vol. 77, no. 17, p. 338 A-346 A, Sep. 2005.

[116] C. E. Talley *et al.*, "Surface-enhanced Raman scattering from individual Au nanoparticles and nanoparticle dimer substrates," *Nano Lett.*, vol. 5, no. 8, pp. 1569–1574, 2005.

[117] N. J. Halas, "Plasmonics: An emerging field fostered by nano letters," *Nano Lett.*, vol. 10, no. 10, pp. 3816–3822, 2010.

[118] S. Lal, N. K. Grady, J. Kundu, C. S. Levin, J. B. Lassiter, and N. J. Halas, "Tailoring plasmonic substrates for surface enhanced spectroscopies," *Chem. Soc. Rev.*, vol. 37, no. 5, p. 898, Apr. 2008.

[119] E. Cubukcu, S. Zhang, Y.-S. Park, G. Bartal, and X. Zhang, "Split ring resonator sensors for infrared detection of single molecular monolayers," *Appl. Phys. Lett.*, vol. 95, no. 4, p. 043113, 2009.

[120] A. Braun and S. A. Maier, "Versatile Direct Laser Writing Lithography Technique for Surface Enhanced Infrared Spectroscopy Sensors," *ACS Sensors*, vol. 1, no. 9, pp. 1155–1162, Sep. 2016.

[121] D. Yoo *et al.*, "High-Throughput Fabrication of Resonant Metamaterials with Ultrasmall Coaxial Apertures via Atomic Layer Lithography," *Nano Lett.*, vol. 16, no. 3, pp. 2040–2046, Mar. 2016.

[122] D. Ji *et al.*, "Efficient Mid-Infrared Light Confinement within Sub-5-nm Gaps for Extreme Field Enhancement," *Adv. Opt. Mater.*, vol. 5, no. 17, p. 1700223, Sep. 2017.

[123] F. Neubrech, C. Huck, K. Weber, A. Pucci, and H. Giessen, "Surface-enhanced

infrared spectroscopy using resonant nanoantennas," *Chem. Rev.*, vol. 117, no. 7, pp. 5110–5145, Mar. 2017.

[124] D. Yoo *et al.*, "High-Contrast Infrared Absorption Spectroscopy via Mass-Produced Coaxial Zero-Mode Resonators with Sub-10 nm Gaps," *Nano Lett.*, vol. 18, no. 3, pp. 1930–1936, Mar. 2018.

[125] D. Heydari, Y. Bai, N. Bandyopadhyay, S. Slivken, and M. Razeghi, "High brightness angled cavity quantum cascade lasers," *Appl. Phys. Lett.*, vol. 106, no. 9, p. 091105, Mar. 2015.

[126] A. Spott *et al.*, "Quantum cascade laser on silicon," *Optica*, vol. 3, no. 5, p. 545, May 2016.

[127] J. S. Levy, A. Gondarenko, M. A. Foster, A. C. Turner-Foster, A. L. Gaeta, and M. Lipson, "CMOS-compatible multiple-wavelength oscillator for on-chip optical interconnects," *Nat. Photonics*, vol. 4, no. 1, pp. 37–40, Jan. 2010.

[128] A. G. Griffith *et al.*, "Silicon-chip mid-infrared frequency comb generation," *Nat. Commun.*, vol. 6, no. 1, p. 6299, Dec. 2015.

[129] C. Reimer *et al.*, "Mid-infrared photonic crystal waveguides in silicon," *Opt. Express*, vol. 20, no. 28, p. 29361, Dec. 2012.

[130] G. Z. Mashanovich *et al.*, "Low loss silicon waveguides for the mid-infrared.," *Opt. Express*, vol. 19, no. 8, pp. 7112–7119, Apr. 2011.

[131] Y. Zou, S. Chakravarty, and R. T. Chen, "Mid-infrared silicon-on-sapphire waveguide coupled photonic crystal microcavities," *Appl. Phys. Lett.*, vol. 107, no. 8, p. 081109, Aug. 2015.

[132] B. Dong *et al.*, "Silicon-on-Insulator Waveguide Devices for Broadband Mid-

Infrared Photonics Silicon-on-Insulator Waveguide Devices," *IEEE Photonics J.*, vol. 9, no. 3, pp. 4501410–4501410, Jun. 2017.

[133] S. A. Miller *et al.*, "Low-Loss Silicon Platform for Broadband Mid-Infrared Photonics," *Optica*, vol. 4, no. 7, p. 707, Jul. 2017.

[134] C. Haffner *et al.*, "Low-loss plasmon-assisted electro-optic modulator," *Nature*, vol. 556, no. 7702, pp. 483–486, 2018.

[135] C. Haffner *et al.*, "All-plasmonic Mach–Zehnder modulator enabling optical high-speed communication at the microscale," *Nat. Photonics*, vol. 9, no. 8, pp. 525–528, Aug. 2015.

[136] C. Chen *et al.*, "Three-Dimensional Integration of Black Phosphorus Photodetector with Silicon Photonics and Nanoplasmonics," *Nano Lett.*, vol. 17, no. 2, pp. 985–991, 2017.

[137] M. Chamanzar, Z. Xia, S. Yegnanarayanan, and A. Adibi, "Hybrid integrated plasmonic-photonic waveguides for on-chip localized surface plasmon resonance (LSPR) sensing and spectroscopy," *Opt. Express*, vol. 21, no. 26, p. 32086, Dec. 2013.

[138] W. A. Challener *et al.*, "Heat-assisted magnetic recording by a near-field transducer with efficient optical energy transfer," *Nat. Photonics*, vol. 3, no. 4, pp. 220–224, Apr. 2009.

[139] P. Gogol, A. Aassime, A. Chelnokov, A. Apuzzo, S. Blaize, and J.-M. Lourtioz, "Giant Coupling Effect between Metal Nanoparticle Chain and Optical Waveguide," *Nano Lett.*, vol. 12, no. 2, pp. 1032–1037, Feb. 2012.

[140] A. Sampaolo, P. Patimisco, J. M. Kriesel, F. K. Tittel, G. Scamarcio, and V.

Spagnolo, “Single mode operation with mid-IR hollow fibers in the range 51-105 μm,” *Opt. Express*, vol. 23, no. 1, p. 195, Jan. 2015.

[141] Z. Tang *et al.*, “Low loss Ge-As-Se chalcogenide glass fiber, fabricated using extruded preform, for mid-infrared photonics,” *Opt. Mater. Express*, vol. 5, no. 8, p. 1722, 2015.

[142] D. A. Mohr, D. Yoo, C. Chen, M. Li, and S.-H. Oh, “Waveguide-Integrated Mid-Infrared Plasmonics with High-Efficiency Coupling for Ultracompact Surface-Enhanced Infrared Absorption Spectroscopy,” May 2018. http://arxiv.org/abs/1805.01391

[143] D. Weber *et al.*, “Longitudinal and transverse coupling in infrared gold nanoantenna arrays: long range versus short range interaction regimes,” *Opt. Express*, vol. 19, no. 16, p. 15047, Aug. 2011.

[144] B. Chen *et al.*, “Hybrid Photon-Plasmon Coupling and Ultrafast Control of Nanoantennas on a Silicon Photonic Chip,” *Nano Lett.*, vol. 18, no. 1, pp. 610–617, 2018.

[145] A. Tittl, P. Mai, R. Taubert, D. Dregely, N. Liu, and H. Giessen, “Palladium-based plasmonic perfect absorber in the visible wavelength range and its application to hydrogen sensing,” *Nano Lett.*, vol. 11, no. 10, pp. 4366–4369, Oct. 2011.

[146] P. Alonso-González *et al.*, “Experimental Verification of the Spectral Shift between Near- and Far-Field Peak Intensities of Plasmonic Infrared Nanoantennas,” *Phys. Rev. Lett.*, vol. 110, no. 20, p. 203902, May 2013.

[147] J. Zuloaga and P. Nordlander, “On the energy shift between near-field and far-field peak intensities in localized plasmon systems,” *Nano Lett.*, vol. 11, no. 3, pp. 1280–

1283, 2011.

[148] A. Apuzzo *et al.*, "Observation of near-field dipolar interactions involved in a metal nanoparticle chain waveguide," *Nano Lett.*, vol. 13, no. 3, pp. 1000–1006, 2013.

[149] V. Giannini, Y. Francescato, H. Amrania, C. C. Phillips, and S. A. Maier, "Fano resonances in nanoscale plasmonic systems: A parameter-free modeling approach," *Nano Lett.*, vol. 11, no. 7, pp. 2835–2840, 2011.

[150] E. Cubukcu and F. Capasso, "Optical nanorod antennas as dispersive one-dimensional Fabry–Pérot resonators for surface plasmons," *Appl. Phys. Lett.*, vol. 95, no. 20, p. 201101, Nov. 2009.

[151] S. Fan, W. Suh, and J. D. Joannopoulos, "Temporal coupled-mode theory for the Fano resonance in optical resonators," *J. Opt. Soc. Am. A*, vol. 20, no. 3, p. 569, 2003.

[152] J. D. Joannopoulos, S. G. Johnson, J. N. Winn, and R. D. Meade, *Photonic Crystals: Molding the Flow of Light*, 2nd ed. Princeton: Princeton University Press, 2008.

[153] W. Suh, Z. Wang, and S. Fan, "Temporal coupled-mode theory and the presence of non-orthogonal modes in lossless multimode cavities," *IEEE J. Quantum Electron.*, vol. 40, no. 10, pp. 1511–1518, Oct. 2004.

[154] P. H. C. Eilers, "A perfect smoother," *Anal. Chem.*, vol. 75, no. 14, pp. 3631–3636, 2003.

[155] H. A. Willis, V. J. I. Zichy, and P. J. Hendra, "The laser-Raman and infra-red spectra of poly(methyl methacrylate)," *Polymer (Guildf).*, vol. 10, pp. 737–746, Jan. 1969.

[156] O. Limaj *et al.*, "Infrared Plasmonic Biosensor for Real-Time and Label-Free Monitoring of Lipid Membranes," *Nano Lett.*, vol. 16, no. 2, pp. 1502–1508, Feb.

2016.

[157] J. Bochterle, F. Neubrech, T. Nagao, and A. Pucci, “Angstrom-Scale Distance Dependence of Antenna-Enhanced Vibrational Signals,” *ACS Nano*, vol. 6, no. 12, pp. 10917–10923, Dec. 2012.

[158] X. Chen, C. Ciracì, D. R. Smith, and S. H. Oh, “Nanogap-enhanced infrared spectroscopy with template-stripped wafer-scale arrays of buried plasmonic cavities,” *Nano Lett.*, vol. 15, no. 1, pp. 107–113, Jan. 2015.

[159] Y. Yu *et al.*, “Experimental demonstration of linearly polarized 2–10 μm supercontinuum generation in a chalcogenide rib waveguide,” *Opt. Lett.*, vol. 41, no. 5, p. 958, Mar. 2016.

[160] M. P. Nielsen, X. Shi, P. Dichtl, S. A. Maier, and R. F. Oulton, “Giant nonlinear response at a plasmonic nanofocus drives efficient four-wave mixing,” *Science*, vol. 358, no. 6367, pp. 1179–1181, Dec. 2017.

[161] E. Prodan, C. Radloff, N. J. Halas, and P. Nordlander, “A Hybridization Model for the Plasmon Response of Complex Nanostructures,” *Science*, vol. 302, no. 5644, pp. 419–422, Oct. 2003.

[162] J. D. Caldwell *et al.*, “Low-loss, infrared and terahertz nanophotonics using surface phonon polaritons,” *Nanophotonics*, vol. 4, no. 1, pp. 44–68, Jan. 2015.

[163] L. Feng *et al.*, “Experimental demonstration of a unidirectional reflectionless parity-time metamaterial at optical frequencies,” *Nat. Mater.*, vol. 12, no. 2, pp. 108–113, 2013.

[164] D. Rodrigo *et al.*, “Resolving molecule-specific information in dynamic lipid membrane processes with multi-resonant infrared metasurfaces,” *Nat. Commun.*,

vol. 9, no. 1, p. 2160, Dec. 2018.

[165] A. Tittl *et al.*, “Imaging-based molecular barcoding with pixelated dielectric metasurfaces,” *Science*, vol. 360, no. 6393, pp. 1105–1109, Jun. 2018.